University of California, Merced

Ph.D. Dissertation

Accounting for Surface Concentrations Using a VOF Front Tracking Method in Multiphase Flow

A dissertation submitted in partial fulfillment of the requirements for the degree

Doctor of Philosophy in Applied Mathematics

by

David W. Martin

September 3, 2015

University of California, Merced

Graduate Division

This is to certify that I have examined a copy of a dissertation by

David W. Martin

and found it satisfactory in all respects, and that any and all revisions required by the examining committee have been made.

Faculty Advisor: _____
François Blanchette

Committee Members: _____
Karin Leiderman

_____
Mayya Tokman

Applied Mathematics Graduate Studies Chair: _____
Boaz Ilan

_____
Date Signed

Abstract

In this dissertation, we present a numerical method for tracking surfactants on an interface in multiphase flow, along with applications of the method to two physical problems. We also present an extension of our method to track charged droplets. Our method combines a traditional volume of fluid (VOF) method with marker tracking. After describing this method in detail, we present a series of tests we used to validate our method. The applications we consider are the coalescence of surfactant-laden drops, and the rising of surfactant-laden drops in stratifications.

In our study of the coalescence of surfactant-laden drops, we describe conditions under which coalescence is partial, rather than total. In particular, we examine the dependence of the critical Ohnesorge number, above which coalescence is total, on surfactant effects. We find that the surfactant potency has a surprising non-monotonic effect on the critical Ohnesorge number. This effect is explained by a balancing interface area loss and tangential stresses, which we describe using a scaling argument. Our argument is confirmed by forming a predicted critical Ohnesorge number profile, which qualitatively matches the data. We also discuss gravity effects, varying initial conditions, and daughter drops resulting from partial coalescence.

In our study of rising drops, we examine three distinct physical setups. In the first setup, we examine a drop coated in insoluble surfactant rising in a uniform ambient. Our results for an unstratified ambient show good agreement with earlier work, and fill a gap between results for zero Reynolds number and intermediate Reynolds number. In our second setup, we study drops rising in a linear density stratification, with and without surfactant. Entrainment effects on the rising drop are isolated and used to compute an effective buoyancy of entrained fluid. In our third setup, we present velocity profiles of a clean drop entering a layer of soluble surfactant. The surfactant layer "sucks" the drop in, before it transitions to a terminal Rising speed.

Lastly, we extend our method to track electric fields and charges in the bulk fluid and on the surface. Such a numerical method has applications to electrically induced drop deformation, the coalescence of charged droplets, and electro-wetting. This extension of our method is validated by examining a simple test case.

Acknowledgements

We acknowledge support from NSF grant DMS 0808129, and from the UC Merced Graduate Dean's Dissertation Fellowship for 2015-2015, and for the summer of 2015.

I would like to thank my advisor, Francois Blanchette, for teaching me how think, to write, and to speak like a scientist for celebrating my successes, and patiently encouraging me through setbacks and disappointments, and for showing me how research is done.

I would also like to thank the other members of my committee, Mayya Tokman and Karin Leiderman, for their helpful advice, and the professors whove had me as a student: Arnold Kim, Boaz Ilan, Harish Bhat, and Yue Lei thank you for training me in applied math; and thank you to Mike Sprague for inspiring me to go into fluid dynamics.

Thank you to my friends and colleagues, Mac, Terese, and Anna for keeping me sane during the course of my work at UC Merced. In addition, I would like to thank my parents, Doug and Vera Martin, for supporting me, and for coming to my dissertation defense.

Contents

Chapter 1

Introduction

1.1 Multiphase Flow

Fluid mechanics is the study of materials, such as liquids and gases, that deform freely under an applied stress, and assume the shape of their container. Although the study of fluid mechanics dates back to ancient times [1], it reached its modern form in the mid 19^{th} century, with the derivation of a set of governing equations - the Navier-Stokes equations. Derived from Newton's second law and the law of mass conservation, the Navier-Stokes equations accurately model a vast number of problems, in physical settings ranging from the motion of a single cell in the human body, to flow in a pipe, to the earth's atmosphere, and even to astrophysical settings, such as accretion disks.

Due to the presence of a highly nonlinear inertial term, the Navier-Stokes equations do not admit an exact analytic solution in most settings. However, George Gabriel Stokes, one of the founders of modern fluid mechanics, managed to obtain a number of solutions in the special case of creeping flow - also called Stokes flow - in which inertia is negligible. One of his best known solutions concerns flow around a solid sphere falling at a steady speed in a homogeneous liquid. Stokes was able to compute the flow field of the surrounding fluid and the drag it exerted on the sphere - from which he obtained an expression for the speed of the falling sphere, given by [2]:

$$U_{\text{St}} = \frac{2}{9} R_0^2 g \frac{\rho_s - \rho_f}{\mu} \tag{1.1}$$

where R_0 is the radius of the sphere, g is the coefficient of gravity, μ is the viscosity of the surrounding fluid, ρ_s is the density of the sphere, and ρ_f is the density of the fluid. In 1911, the fluid flow about of a steadily moving spherical drop was solved simultaneously by Jacques Hadamard [3] and Witold Rybczynski [4]. By computing the flow field both inside and outside the drop, they managed to obtain the speed of the rising drop:

$$U_{\text{HR}} = \frac{2}{3} R_0^2 g \frac{\rho_E - \rho_I}{\mu_E} \frac{\mu_E + \mu_I}{2\mu_E + 3\mu_I} \tag{1.2}$$

where ρ_E, ρ_I and μ_E, μ_I represent the respective density and viscosity of the exterior, interior fluid. Notice that as the viscosity of the interior fluid goes to infinity, i.e. $\mu_E/\mu_I \longrightarrow 0$, the stokes speed (Eq. (1.1)) is recovered.

The problem considered by Hadamard and Rybczynski is an example of multiphase flow - fluid flow near an interface between two or more immiscible fluids where surface tension plays a dominant

role. Multiphase flow abounds in nature and in everyday life: water in a sink, raindrops, mists, capillary waves, oil in water, tears of wine, lava flows, condensation, air and liquid in the respiratory system - all are examples of multiphase flow. A better understanding of multiphase flow holds the promise of advances in the fields of biology, medicine, climate science, weather prediction, and a variety of applications in industry. Painting and jet printing are examples of applications in which the interactions of tiny droplets on a scale difficult to directly observe produce unwanted results (such as splattering). In the pharmaceutical industry, it is often important to mix fluids containing medicine on a very small scale, at which direct mechanical motion (like stirring with a straw) cannot be applied. In that case, gradients in surface tension can be used to produce the mixing effects automatically.

A good understanding of multiphase flow is also essential to the rapidly growing field of microfluidics - the manufacture of devices designed to precisely manipulate tiny amounts of fluid. Microfluidic devices have applications to a wide range of fields, including the handling of quantum dots, the manufacture of plastics, inkjet printing, and especially to microbiology, where they are revolutionizing the field. DNA molecules, proteins, individual cells, bacterial colonies - all can be precisely manipulated, often on a massive scale, using microfluidic devices. The behavior of infectious bacteria, for instance, can be studied under carefully controlled circumstances. Electric fields, chemical gradients, and populations of competing microorganisms can all be introduced in a controlled manner. The manipulation of fluids, particularly droplets, with such precision requires a profound understanding of surface tension, which is a dominant force at such length-scales.

1.2 Surface Tension

Surface tension arises as a consequence of intermolecular attraction. Given two substances whose molecules have differing levels of intermolecular attraction, the substance whose molecules have greater attraction will draw together and exclude those molecules with a weaker attraction. For instance, water, with its highly polar molecules, exhibits a much stronger intermolecular attraction than oil. As a result, water and oil are said to be immiscible - they don't mix. In miscible fluids, such as water and ethanol, the two species of molecules exhibit similar levels of intermolecular attraction. When two immiscible fluids come into contact, the molecules of each kind are drawn by intermolecular forces toward the interior of their own fluid body. This results in a tendency to minimize the surface area of the interface between the two fluids. Given that a spherical body has a minimal surface area, surface tension is the reason why jets of fluid often break apart into spherical drops, and why, in the absence of exterior forces, drops naturally assume a spherical shape. Surface tension can be measured by computing the amount of energy that is added to the fluid interface per unit area:

$$\gamma = \frac{\partial E}{\partial A} \tag{1.3}$$

where E is the surface energy and A is surface area. For a given pressure and temperature, the coefficient, γ, of surface tension is a characteristic physical property of two substances. For example, the surface tension of air and water at room temperature ($20°C$) and atmospheric pressure is $\gamma_{\text{air/water}} = 72.86 \times 10^{-3}\text{N/m}$.

Surface tension affects the stress at the interface, as described by the Young-Laplace equations:

$$[\mathbf{n} \cdot \widetilde{\mathbb{T}}] = \gamma\kappa\mathbf{n} + \nabla\gamma \tag{1.4}$$

where $[\mathbf{n}\cdot\widetilde{\mathbb{T}}]$ represents the stress jump across the interface,[1] κ is the total (twice the mean) curvature of the interface, and $\mathbf{n}$ is the unit normal to the interface. The first term on the right accounts for

[1] Here, $\widetilde{\mathbb{T}}$ is the total stress. We later use $\mathbb{T}$ (no tilde) to represent the viscous stress.

the change in pressure across the interface, while the second term on the right accounts for the tangential stress jump due to local variations in surface tension. The curvature term represents the energy minimizing potential of the surface. Flat interfaces have already minimized area locally, but curved interfaces have extra molecules at or near the surface - leading to a stress at the interface. For example, in the absence of external forces, a spherical drop is at equilibrium because it has globally minimized its surface area, but locally, at each point the surface seeks to flatten out, resulting in a stress across the interface that is proportional to the curvature.

In many applications, the surface tension is assumed constant and uniform throughout the system, so that $\nabla\gamma = \mathbf{0}$, and this is often a good approximation. In general, however, γ can vary locally due to a variety of factors, including variations in temperature within the fluid body, variations in chemical composition of a fluid mixture (such as alcohol and water), and the presence of surfactants. Local variations in surface tension cause tangential motion along the surface as fluid moves in the direction of increasing tension. Thus, regions of low surface tension tend to expand, while regions of high surface tension tend to contract. For instance, when a bar of soap floats on top of a body of water - as in a sink, the soap lowers the surface tension of the air/water interface. As a consequence, the portion of the surface contaminated by the soap will flow outward, seeking to bring the surface into equilibrium by covering it entirely. The forces associated to this motion are called Marangoni forces.

1.3 Surfactants

We focus on Marangoni forces generated by surfactants - molecules that prefer to reside on fluid interfaces. A wide range of chemical substances can act as surfactants, and every day examples include soaps, oils, detergents, foaming agents, wetting agents, and dispersants. Even dust can act as a surfactant. Many surfactant molecules have hydrophillic (polar) and hydrophobic (non-polar) components, so that when they reside on an interface between water and some other fluid, such as air or oil, they can minimize energy by having the hydrophillic component face the water, and the hydrophobic component face away from the water. Thus, surfactants find it energetically favorable to reside on fluid interfaces. As a consequence, surfactants reduce surface tension on the fluid interface. By locally altering surface tension, surfactants affect flow near fluid interfaces on a macroscopic level, and can fundamentally alter the dynamics of a given problem, generating Marangoni flows from areas of high concentration toward areas of low concentration.

Depending on the species of surfactant, and the fluids with which it interacts, the surfactant may be soluble (able to dissolve in the fluid), or insoluble - only able to reside on the surface. The process by which surfactants move from the bulk to the interface is called adsorption, the process by which they leave the interface is called desorption. Collectively, these two processes are called sorption. Because surfactants prefer to reside on interfaces, adsorption often takes place more quickly than desorption. However, when the concentration of surfactant molecules on the surface is sufficiently high, the process of desorption can dominate. Indeed, because there is only a finite amount of space on a fluid interface, there exists a maximum packing concentration of surfactant molecules on the surface which cannot be exceeded. If the surfactant is soluble, the molecules will rapidly desorb from the surface when the maximum packing concentration is approached. If the surfactant is insoluble, then the surface pressure of the interface increases without bound.

Accounting for surfactant effects on surface tension is a complex physiochemical problem that has inspired decades of research, and is still the subject of ongoing investigation [5, 6]. The simplest approach is to use a linear elasticity relation between local surfactant concentration, Γ, and surface tension, γ. This approach yields a good approximation in many cases, and is frequently used by

researchers [7–11]. However, it does not account for the carrying capacity of the surface. In general, the amount of surfactant a surface can adsorb is limited by a maximum packing concentration, Γ_∞, of surfactant molecules on the surface. The simplest surfactant relation that accounts for the maximum packing concentration is the Langmuir relation [11]:

$$\gamma - \gamma_{\max} = \mathcal{R}T\Gamma_\infty \ln\left(1 - \frac{\Gamma}{\Gamma_\infty}\right) \quad . \tag{1.5}$$

Here, $\gamma_{\max}$ is the maximum surface tension, obtained on a clean (surfactant free) interface, $\mathcal{R}$ is the ideal gas constant, T is the temperature, and Γ_∞ is the maximum packing concentration of surfactant molecules on the surface. The Frumkin relation, given as [12]

$$\gamma - \gamma_{\max} = \mathcal{R}T\Gamma_\infty \left(\ln\left(1 - \frac{\Gamma}{\Gamma_\infty}\right) + \frac{\lambda}{2}\left(\frac{\Gamma}{\Gamma_\infty}\right)^2\right) \tag{1.6}$$

generalizes the Langmuir relation by accounting for intermolecular attraction. In particular, this is done by the rightmost term in equation (1.6), which is scaled by an interaction parameter, λ. In what follows, we will be using a linear elasticity relation, for simplicity. However, we remain mindful of the limitations of this approach.

1.4 Numerical Methods for Tracking Multiphase Flow

Since computers came to widespread use in the 1960's, numerical methods have become a major force in fluid dynamics, opening up avenues of mathematical analysis out of reach of direct theoretical calculation. Numerical methods employ computer algorithms to obtain approximate solutions to partial differential equations. This allows researchers to study systems of equations far too complex to admit an analytic solution. However, a major problem with numerical methods is that errors can accumulate over numerous iterations - particularly when advancing a physical system in time - resulting in serious inaccuracies, or even the complete breakdown of the simulation. As a consequence, a field of numerical analysis has been developed, in which researchers carefully examine the potential pitfalls of existing methods, determining under what circumstances the method is stable (i.e. accurately and reliably solves the problem), and under what circumstances it is unstable (i.e. the simulation breaks down).

Within the last two or three decades, numerical methods have been developed that accurately track interfaces between fluids [13–18]. Many approaches to multiphase flow combine the two fundamental approaches to fluid dynamics: the Eulerian approach, and the Lagrangian approach. In the Eulerian approach, the fluid velocity field is tracked relative to a fixed spatial domain. In the Lagrangian approach, the spatial positions of individual particles are tracked in time - so that the coordinates represent the locations of individual particles, rather than fixed locations in space [15].

In most numerical approaches to multiphase flow, the Navier-Stokes equations are solved on an Eulerian grid using either finite differences (FD) or finite element methods (FEM). In finite element methods, the governing equations are rewritten in integral, rather than differential form, and the physical domain is partitioned into small elements, usually triangles, or in the case of fully 3D simulations, tetrahedrons. Finite element methods have the advantage that they can handle arbitrary domains, but they can be difficult and computationally expensive to implement. Finite differences, on the other hand, take a simple and direct approach to solving differential equations: approximating derivatives with ratios of small, incremental differences.

On solving the Navier-Stokes equations numerically, the Eulerian velocity field is obtained. The velocity is then coupled to a moving interface, which is tracked using more specialized methods. One

such approach, the level set (LS) method, treats the interface as a level set of a continuous function [14, 16]. This approach is frequently combined with adaptive meshes to get good conservation properties at the interface [17,19]. The Volume Of Fluid (VOF) method computes the concentration of a particular fluid in each grid cell, and advects it with the fluid [13, 20]. This method was later coupled with a front tracking method, which advects markers with the fluid, and interpolates between them with cubic splines [15]. Together with marker tracking, the VOF method achieves excellent accuracy at the interface, but does not easily handle topological changes. We use a VOF method coupled with marker tracking, and focus on applications where topological changes are not a significant issue.

As numerical methods of studying fluid interfaces have improved, researchers been able to examine increasingly realistic settings, even accounting for surfactant effects. Within the last decade, there has been an outpouring of numerical studies employing a wide range of methods to track surfactant on a fluid interface. Tryggvason, *et al.* [21] developed a front tracking method to track surfactant on an interface, by advecting markers with the moving front. Another front tracking method [22] solves for surface concentration of surfactant by interpolating from a bulk concentration. Lai, *et al.* [23] developed an immersed boundary (IB) method for tracking surfactant, which has been adapted by others for the study of vesicles [24] and rapid sorption [25]. Khatri and Tornberg [26, 27] introduced an embedded boundary method for tracking surfactant, in which the fluid interface is "embedded" in the Eulerian grid. Further methods that employ Eulerian bulk fluid domains include an arbitrary Lagrangian-Eulerian (ALE) finite element mesh [28]; level sets [29]; and a complex phase field domain [30]. Non-continuum methods, such as purely Lagrangian particle tracking [31, 32], and lattice Boltzmann methods [33] have also been employed.

1.5 In this Dissertation

In this dissertation, we track the surfactant using a Lagrangian approach similar to that of Tryggvason, *et al.* [21], that automatically conserves mass, and employ our method to account for surfactants for the first time in two widely studied problems: coalescing drops and bubbles, and drops rising in a stratified medium. Our method uses numerical simulations based on the VOF method with front tracking. We solve the Navier-Stokes equations using finite differences on a staggered MAC (marker and cell) grid. The system is advanced in time using a second order Runge-Kutta method in some cases, and a first order Euler, in others. The viscous and nonlinear terms in the Navier-Stokes are both computed using centered finite differences. The pressure is computed using the projection method [34], which results in a Poisson-type equation for the pressure that enforces conservation of mass. This is inverted using iterative methods, executed on a linear multigrid, for computational efficiency.

In chapter 2, we introduce the equations of multiphase flow in a general, dimensional form. Then, in chapter 3, we present in detail our numerical method and its validation. In chapter 4, we present our study of coalescing drops. In particular, we focus on the phenomenon of partial coalescence, in which a drop merging with a reservoir - or another drop - pinches off to form a daughter drop. Partial coalescence happens in a variety of natural settings, such as cloud formation, mists, and aerosols in the earth's atmosphere; and in a variety of industrial settings, such as painting and inkjet printing. By tracking the merging interface numerically, we determine circumstances under which coalescence is total (the drop completely merges with the reservoir) or partial. Although this process has been studied for the idealized case in which surfactants are not present, we account for surfactants on the merging interface, for the first time, thereby providing a much more realistic picture of coalescence events. In addition, we examine gravity effects, differing initial conditions, and the daughter drops produced by partial coalescence, to obtain a complete physical picture.

In chapter 5, we apply our method to rising surfactant-laden drops. This is directly applicable to oil drops rising in the ocean, as happened in the 2010 BP oil spill. We study three setups: a drop coated with insoluble surfactant rising in a uniform ambient; a drop coated with insoluble surfactant rising in a density stratification, as happens in pycnoclines in the ocean; and a clean drop entering a layer of dissolved surfactant, as happens if dispersants have been applied, as is usually done in the case of oil spills in the ocean. Being able to predict the rise time of oil drops is essential to containing large oil spills, and this study promises to improve the accuracy of such predictions.

In chapter 6, we present an extension of our method to a whole new class of problems: tracking electric charge on a fluid interface. The coalescence of charged drops occurs in a variety of settings, most notably in thunder clouds. The study of charged drops is also important in dewetting solid surfaces. In particular, solid surfaces can be cleaned by applying an electric field, causing the drops to jump from the interface. The application to electric fields is a natural extension of our method for tracking surfactants. In §6.1, we present the equations electro-hydrodynamics, first in dimensional, then in dimensionless form. In §6.2, we describe our method for solving these equations numerically, and in §6.3, we present a validation of our method, by examining a simple test case that admits an analytic solution. We then conclude this dissertation in Chapter 7.

Chapter 2

Equations of Multiphase Flow

2.1 Equations of Fluid Motion (Dimensional)

All phases of the fluid obey the incompressible Navier-Stokes equations, given in dimensional form as

$$\nabla \cdot \mathbf{u} = 0 \tag{2.1}$$

$$\rho \frac{\partial \mathbf{u}}{\partial t} + \rho \mathbf{u} \cdot \nabla \mathbf{u} = -\nabla P + \nabla \cdot \left(\mu(\nabla \mathbf{u} + \nabla \mathbf{u}^T)\right) - g(\rho - \rho_a)\mathbf{k} + \delta_s \mathbf{F}_s \quad . \tag{2.2}$$

Equation (2.1) describes incompressibility, or volume conservation, and is valid even in the presence of varying density and viscosity - so long as these variations are based on fluid composition rather than fluid compression. Equation (2.2) is a momentum balance. The two terms on the lefthand side represent the convective and advective derivatives of the fluid velocity, and the righthand side contains the forcing terms, representing, from left to right: pressure, viscosity, gravity, and surface forces. P is the dynamic pressure, obtained by subtracting the static pressure from the mechanical pressure: $P = P_{\text{mech}} - \rho_a z g$, where z is the vertical position coordinate. Here, ρ_a is a constant background density. In many problems, ρ_a is the density of the ambient fluid, such as air or water. The viscous term does not reduce to the familiar form $\mu \nabla^2 \mathbf{u}$ because the viscosity is not constant in our domain. In the gravity term, $\mathbf{k}$ is a unit vector in the vertical direction.

The delta function, $\delta_s(\mathbf{x})$, in Eq. (2.2) is nonzero only on the interface, and can be defined as a distributional derivative of an indicator function, ϕ, which equals 1 on one fluid and 0 on the other. It multiplies the surface force, $\mathbf{F}_s$. In the applications we consider, the surface force takes the form

$$\mathbf{F}_s = \gamma \kappa \mathbf{n} + \nabla_s \gamma - gh(\rho_f - \rho_a)\mathbf{k} \tag{2.3}$$

where $\mathbf{n}$ is the outward unit normal to the surface, κ is the curvature of the interface, γ is the surface tension, and $\nabla_s = (\mathbf{I} - \mathbf{nn}) \cdot \nabla$ is the projection of the gradient operator onto the surface. The term $\gamma \kappa \mathbf{n}$, as described by [13], accounts for the stress jump across the interface. Previous work [35] described how the term $\nabla_s \gamma$ accounts for tangential stresses (Marangoni forces) on the surface, due to surface tension gradients. The term $-gh(\rho_f - \rho_a)\mathbf{k}$ accounts for the buoyancy of a soap film: h is the film thickness and ρ_f is the density of the film. This term, described by [36], does not appear in multiphase flow equations, except when one is tracking soap films, which we do in one of our applications. In addition, we move the interface with the fluid, according to the rule

$$\frac{d\mathbf{x}_s}{dt} = \mathbf{u}|_s \quad . \tag{2.4}$$

The density and viscosity depend on the aforementioned indicator function, ϕ, which equals 1 when we are on the drop or interior fluid, and 0 when we are on the ambient (background fluid). They may also depend on the concentration, c, of a chemical or stratifying agent, such as salt or temperature. Assuming both dependencies are linear, the density and viscosity are given by

$$\rho = \phi\rho_d + (1-\phi)\left(c\rho_c + (1-c)\rho_a\right) \tag{2.5}$$

$$\mu = \phi\mu_d + (1-\phi)\left(c\mu_c + (1-c)\mu_a\right) \tag{2.6}$$

where ρ_d, ρ_a, ρ_c and μ_d, μ_a, μ_c are the respective densities and viscosities of the drop, the ambient, and the ambient in the presence of a stratification agent, c - particularly, when $c = 1$.

The stratifying agent, c, satisfies an advection-diffusion equation, given by

$$\frac{\partial c}{\partial t} + \mathbf{u}\cdot\nabla c = \nabla\cdot(k_D\nabla c) \tag{2.7}$$

where k_D is a diffusion coefficient.

2.2 Surfactant Tracking (Dimensional)

The surfactant concentration can also be tracked using advection-diffusion equations. The surfactant concentration, Λ, in the bulk fluid, satisfies the relation

$$\frac{\partial \Lambda}{\partial t} + \mathbf{u}\cdot\nabla\Lambda = \nabla\cdot(k_\Lambda\nabla\Lambda) - \delta_s J(\Gamma, \Lambda|_s) \tag{2.8}$$

where $J(\Gamma, \Lambda|_s)$ accounts for surfactant adsorption onto the interface, Γ is the concentration of surfactant on the interface, and k_Λ is a diffusion coefficient for surfactant in the bulk. The surfactant concentration on the interface satisfies an advection-diffusion equation restricted to the interface [37]:

$$\frac{\partial \Gamma}{\partial t} + \nabla_s\cdot(\Gamma\mathbf{u}) = \nabla_s\cdot(k_\Gamma\nabla\Gamma) + J(\Gamma, \Lambda|_s) \tag{2.9}$$

where k_Γ is a diffusion coefficient for Γ. Here, the surface divergence of an arbitrary vector $\mathbf{v}$ with normal component v_n is given by $\nabla_s\cdot\mathbf{v} = \nabla\cdot\mathbf{v} - \partial v_n/\partial n$, where n is a spatial coordinate normal to the interface. The bulk exchange is described by the Langmuir-Hinshelwood kinetic equation [11,38]:

$$J(\Gamma, \Lambda|_s) = k_{\text{ad}}\Lambda|_s\Big(1 - \frac{\Gamma}{\Gamma_\infty}\Big) - k_{\text{de}}\Gamma \quad . \tag{2.10}$$

The coefficients $k_{\text{ad}}, k_{\text{de}}$ are kinetic constants of adsorption and desorption, respectively, and Γ_∞ is the maximum packing concentration on the surface.

2.3 Surface Tension (Dimensionless)

In general, the surface tension may depend on two factors: the concentration, Γ, of surfactants on the interface, and the concentration, c, of a stratifying agent, such as temperature or salinity, or chemical composition. In the problems we study, we will not be accounting for surface tension variations due to changes in chemical composition or a stratifying agent.

The linear relation we use can be derived from a Taylor expansion of the Langmuir relation (1.5). If we scale our surface tension and surfactant concentration using equilibrium values: $\gamma_{\text{new}} = \gamma_{\text{old}}/\gamma_0$, $\Gamma_{\text{new}} = \Gamma_{\text{old}}/\Gamma_0$, then Eq. (1.5) becomes

$$\alpha_\gamma \gamma = 1 + \text{El} \ln(1 - \alpha_\Gamma \Gamma) \tag{2.11}$$

where we have used the nondimensional numbers

$$\alpha_\gamma = \frac{\gamma_0}{\gamma_{\max}} \qquad \alpha_\Gamma = \frac{\Gamma_0}{\Gamma_\infty} \quad \text{and} \quad \text{El} = \frac{\mathcal{R}T\Gamma_\infty}{\gamma_{\max}} \quad .$$

Here, El is known as the elasticity number. Putting equilibrium values into Eq. (2.11), obtain

$$\alpha_\gamma = 1 + \text{El} \ln(1 - \alpha_\Gamma) \tag{2.12}$$

and hence

$$\gamma = \frac{1 + \text{El} \ln(1 - \alpha_\Gamma \Gamma)}{1 + \text{El} \ln(1 - \alpha_\Gamma)} \quad . \tag{2.13}$$

We wish to reduce the number of parameters further by following other authors [10, 11], and approximating Eq. (2.13) with a linear relation. Compute

$$\gamma'(1) = -\frac{\text{El}}{\alpha_\gamma} \frac{\alpha_\Gamma}{1 - \alpha_\Gamma} \quad .$$

Then a Taylor expansion about $\Gamma = 1$ gives

$$\gamma = 1 - \frac{\text{El}}{\alpha_\gamma} \frac{\alpha_\Gamma}{1 - \alpha_\Gamma} (\Gamma - 1) + \mathcal{O}((\Gamma - 1)^2) \quad .$$

Define

$$\beta = \frac{\text{El}}{\alpha_\gamma} \frac{\alpha_\Gamma}{1 - \alpha_\Gamma} \quad .$$

Then we arrive at a linear approximation to Eq. (2.13):

$$\gamma = 1 + \beta(1 - \Gamma) \quad . \tag{2.14}$$

We will be using Eq. (2.14) everywhere, except in a few cases where we wish to validate against the nonlinear relation. The elasticity coefficient β, defined in Eq. (2.14) as

$$\beta = -\left.\frac{\partial \gamma}{\partial \Gamma}\right|_{\Gamma_0} \quad , \tag{2.15}$$

represents the amount by which the surface tension decreases in response to a unit increase in surfactant concentration. Due to our choice of scales γ_0 and Γ_0, β is proportional to the equilibrium concentration of surfactant. For fixed γ_0, Γ_0, the parameter β measures the potency of the surfactant.

Next, we would like to determine the range of values of Γ for which this approximation is valid. For this, we compute the n^{th} order derivative:

$$\gamma^{(n)}(1) = -\frac{\text{El}}{\alpha_\gamma} \left(\frac{\alpha_\Gamma}{1 - \alpha_\Gamma} \right)^n \quad .$$

Thus, Eq. (2.13) has Taylor expansion

$$\gamma = 1 - \frac{\text{El}}{\alpha_\gamma} \sum_{n=1}^{\infty} \frac{1}{n!} \left(\frac{\alpha_\Gamma(1 - \Gamma)}{1 - \alpha_\Gamma} \right)^n$$

and our approximation should hold when

$$\left| \frac{\alpha_\Gamma(1 - \Gamma)}{1 - \alpha_\Gamma} \right| = \left| \frac{\Gamma - \Gamma_0}{\Gamma_\infty - \Gamma_0} \right| \ll 1 \quad .$$

Chapter 3

Method

All setups we consider are axially symmetric, and as such, we model the fluid interface as a surface of revolution of a 1D curve, and use axisymmetric cylindrical coordinates (see figure 3.1). In particular, points in polar half plane that constitutes our computational domain are represented by the ordered pair (r, z), where r is the distance to the axis and z is the vertical position coordinate. The velocity vector is written $\mathbf{u} = (u, v)$ where u is the radial coordinate and v is the vertical coordinate.

Points on the interface are modeled as functions $(r(s), z(s))$ of the arclength, s, from some point on the axis. Whenever we are modeling a single drop, then this point is at the top of the drop. In that case, we let R_0 be the drop radius, z_0 be the vertical coordinate of the drop center (the horizontal coordinate will be zero, since the drop is always on the axis), and $R = (r^2 + (z - z_0)^2)^{1/2}$ is the distance to the drop center. Other quantities on the surface, such as surfactant concentration, $\Gamma(s)$, and surface tension, $\gamma(s)$, are treated similarly.

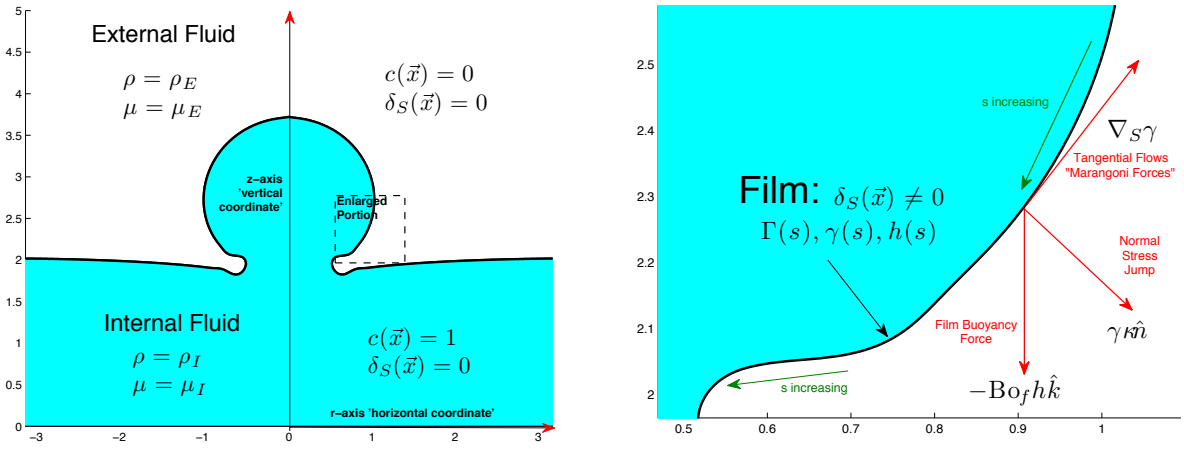

Figure 3.1: Left: The axially symmetric domain considered. Right: Close-up of the front, parameterized in terms of arc length, s, starting from the crest. The functions $\Gamma(s), \gamma(s), h(s)$ represent the surfactant concentration on the surface, surface tension, and film thickness, respectively. A force diagram for the surface forces is included (see equation (4.11)).

Following the front tracking algorithm presented by [15], the interface is tracked using markers that are advected with the fluid in a Lagrangian manner. We interpolate between the markers using cubic splines, allowing for a smooth curvature on the surface. The Lagrangian front is related to the Eulerian grid using linear interpolation. The markers are redistributed at every timestep, to maintain a distance between markers of roughly one grid square. Corrections are made that account for the discontinuous pressure jump at the interface, and surface forces are computed by averaging over one grid square.

3.1 Marker and Cell (MAC) Grid

Position coordinates for the Eularian grid are given by (r_i, z_j), where $i = 0, \ldots, n_r$ and $j = 0, \ldots, n_z$ are indices for the radial and vertical directions, respectively. The position coordinates satisfy $r_{i+1} = r_i + h$ and $z_{j+1} = z_j + h$, where h is a mesh-width. The staggered MAC grid divides the physical domain into square cells, with dimensions $h \times h$, whose sides are positioned at the grid-lines, $r = r_i$, $z = z_j$ (see figure 3.2). Scalar quantities are stored at nodes in the cell centers. For instance, the pressure component, $P_{i,j}$ is stored at the location $(r_{i+1/2}, z_{j+1/2})$. Vector quantities are stored on the sides of grid-cells. The horizontal component of velocity, U_i, is stored at position $(r_i, z_{j+1/2})$, and the vertical component, V_j, is stored at $(r_{i+1/2}, z_j)$.

A major advantage of the MAC grid is that differentiating scalar quantities, like the pressure, can be done by taking centered differences across the length of a single cell, thus eliminating the need for physical boundary conditions for scalar fields. The gradient of the pressure, $\nabla^h P_{i,j}$, yields two components, defined by backward differences:

$$D_r^-[P_{i,j}] = \frac{P_{i,j} - P_{i-1,j}}{h} \quad \text{and} \quad D_z^-[P_{i,j}] = \frac{P_{i,j} - P_{i-1,j}}{h}$$

where $D_r^- P_{i,j}$ resides on the left wall of cell i, j and $D_z^- P_{i,j}$ resides on the bottom wall of the cell. The divergence is taken using forward differences, so as to ensure that the resultant scalar resides at cell centers. In particular,

$$\nabla^h \cdot (U_{i,j}, V_{i,j}) = \frac{r_{i+1} U_{i+1,j} - r_i U_{i,j}}{r_{i+1/2} h} + \frac{V_{i,j+1} - V_{i,j}}{h}$$

(recall that we are using axisymmetric cylindrical coordinates).

3.1.1 Viscous Term

In an axially symmetric system with non-constant viscosity, care must be taken in writing the viscous term, $\nabla \cdot \mathbb{T}$. The viscous stress tensor, $\mathbb{T}$, has components

$$\mathbb{T} = \mu(\nabla \mathbf{u} + \nabla \mathbf{u}^T) = \begin{pmatrix} \tau_{rr} & \tau_{r\theta} & \tau_{rz} \\ \tau_{\theta r} & \tau_{\theta\theta} & \tau_{\theta z} \\ \tau_{zr} & \tau_{z\theta} & \tau_{zz} \end{pmatrix} = \begin{pmatrix} 2\mu \frac{\partial u}{\partial r} & 0 & \mu\left(\frac{\partial u}{\partial z} + \frac{\partial v}{\partial r}\right) \\ 0 & 2\mu \frac{u}{r} & 0 \\ \mu\left(\frac{\partial u}{\partial z} + \frac{\partial v}{\partial r}\right) & 0 & 2\mu \frac{\partial v}{\partial z} \end{pmatrix} \tag{3.1}$$

Here, u and v are the respective radial and vertical components of the velocity field. Taking the divergence yields

$$\nabla \cdot \mathbb{T} \cdot \mathbf{e}_r = \frac{1}{r} \frac{\partial}{\partial r} (r \tau_{rr}) + \frac{\partial \tau_{rz}}{\partial z} - 2\mu \frac{u}{r^2} \tag{3.2}$$

$$\nabla \cdot \mathbb{T} \cdot \mathbf{e}_z = \frac{1}{r} \frac{\partial}{\partial r} (r \tau_{zr}) + \frac{\partial \tau_{zz}}{\partial z} \tag{3.3}$$

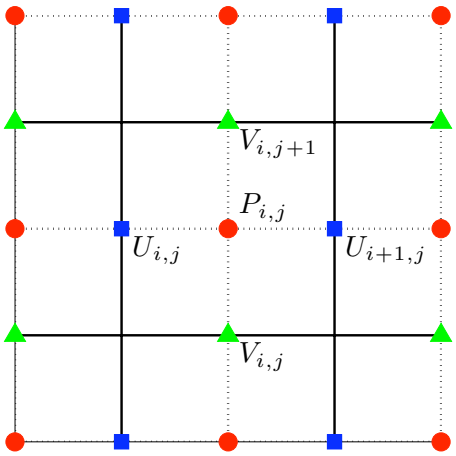

Figure 3.2: A staggered Marker and Cell (MAC) grid. Scalar fields, such as the pressure, are tracked on markers at the cell centers, while vector fields like the velocity are tracked on cell walls.

After some simplification[1], we obtain the following form for the viscous term in the Navier-Stokes:

$$\nabla \cdot \mathbb{T} = \left(\frac{\mu}{r}\frac{\partial}{\partial r}\left(r\frac{\partial u}{\partial r}\right) + \mu\frac{\partial^2 u}{\partial z^2} - \mu\frac{u}{r^2}\right)\mathbf{e}_r + \left(\frac{\mu}{r}\frac{\partial}{\partial r}\left(r\frac{\partial v}{\partial r}\right) + \mu\frac{\partial^2 v}{\partial z^2}\right)\mathbf{e}_z \quad . \tag{3.4}$$

This can be computed in a straightforward manner by taking differences on the MAC grid.

3.1.2 Advection Term

In axisymmetric cylindrical coordinates, the advection term takes on the same form as in cartesian coordinates:

$$\mathbf{u}\cdot\nabla\mathbf{u} = \left(u\frac{\partial u}{\partial r} + v\frac{\partial u}{\partial z}\right)\mathbf{e}_r + \left(u\frac{\partial v}{\partial r} + v\frac{\partial v}{\partial z}\right)\mathbf{k}$$

Because this term is nonlinear, their is no "natural" way to approximate it on a MAC grid, and there is more than one possible approach. We chose to approximate the derivatives using centered differences across two grid-squares:

$$D_r^c[U_{i,j}] = \frac{U_{i+1,j} - U_{i-1,j}}{2h}$$

and similarly for the other derivatives. Altogether, we put

$$\begin{aligned} \text{adv}_{i,j}^r &= U_{i,j}D_r^c[U_{i,j}] + V_{i-1/2,j+1/2}D_z^c[U_{i,j}] \\ \text{adv}_{i,j}^z &= U_{i+1/2,j-1/2}D_r^c[V_{i,j}] + V_{i,j}D_z^c[V_{i,j}] \end{aligned} \tag{3.5}$$

where the velocities at the half indices are computed using linear interpolation from the velocities at the whole indices.

[1] See Appendix A.1 for details of the computation.

3.2 Scalar Field Tracking

We track scalar fields in the bulk by discretizing equations of the form (2.7):

$$\frac{\partial c}{\partial t} + \mathbf{u} \cdot \nabla c = \nabla \cdot (k_D \nabla c)$$

on our MAC grid. The discrete scalar field, $c^t_{i,j}$ at timestep t, is computed at the centers of cell i, j, along with the pressure (see figure 3.2). For an Euler timestep, the successive value at that location is given by

$$c^{t+1}_{i,j} = c^t_{i,j} + \Delta t \left(-(U^t_{i,j}, V^t_{i,j}) \cdot \nabla^h c^t_{i,j} + \nabla^h \cdot (k_{i,j} \nabla^h c^t_{i,j}) \right) \tag{3.6}$$

where $(U^t_{i,j}, V^t_{i,j})$ is the velocity field associated to cell i, j, ∇^h is a vector of backwards differences described in §3.1, and $k_{i,j}$ is the diffusion coefficient, which can vary (in particular, it can change values across the interface). Because $\nabla^h c^t_{i,j}$ resides on the cell walls, as do the components of the velocity field, we can take the dot product without loss of accuracy. After that, however, we must interpolate to estimate the value of $(U^t_{i,j}, V^t_{i,j}) \cdot \nabla^h c^t_{i,j}$ at the cell center, where $c^{t+1}_{i,j}$. The laplacian in the last term of Eq. (3.6) combines the differential operations described in §3.1.

3.2.1 Scalar Field Conservation

We validate our method for tracking scalar fields by modeling a drop rising through a sharp density stratification and measuring how well the mass of the stratifying agent is conserved over time for different resolutions. We use a small cylindrical domain with a radius of 4 drop radii and a height of 8 drop radii. After beginning our simulation with the drop a distance of 1.5 drop radii above the bottom of the container, we allowed the drop to rise through a sharp density stratification at $z = 4$, and stop the simulation when the drop is 1.5 radii away from the top of the container. We allow the stratification agent to diffuse in both the drop and the ambient, with a diffusion coefficient of 1/4000. The error in mass conservation is the percent variation in the mass M_f of the scalar field. The results, shown in table 3.1 show an objectively small error and better than second order convergence. The dimensionless time, t, of the simulation is also given. We chose not to use a fixed time increment because the error in mass conservation is not uniform in time. Instead, it peaks while the drop is entering the stratification, and decreases by an order of magnitude before the drop reaches the top.

h	ΔM_f	t	Order
1/4	3.73×10^{-4}	25.16	NA
1/8	3.68×10^{-5}	22.12	3.34
1/16	2.26×10^{-6}	20.70	4.02
1/32	1.93×10^{-7}	20.04	3.54

Table 3.1: Error in scalar field mass conservation (second column) against resolution (first column). The third column shows the duration of the simulation in dimensionless time, and the last column shows the order of convergence. The drop rose in a cylinder with radius 4 drop radii and height 8, with a density stratification at $z = 4$. The stratification agent diffused freely inside and outside the drop, with a diffusion coefficient of 1/4000 everywhere.

3.3 Front Tracker

The interface is modeled as a surface of revolution of a two-dimensional front (see figure 3.3), which is tracked using markers that are advected with the fluid. We interpolate between the markers using cubic splines. In particular, we associate to each of N markers, an arc-length s_k, measured from some initial marker on the axis, and position coordinates (r_k, z_k), which are treated as functions of the arc-length, s. These are advanced in time using Eq. (2.4). By tabulating second derivatives (r_k'', z_k'') associated to the front, we are able to compute position coordinates $\mathbf{x}(s)$, and their derivatives, $\mathbf{x}'(s), \mathbf{x}''(s)$. The Lagrangian front is connected to the Eulerian grid using linear interpolation. Intersections of the front with gridlines are carefully tabulated, along with first derivatives. Finally, the markers are redistributed at every timestep, in order to maintain a distance between markers of roughly one gridsquare: $\Delta s \approx h$.

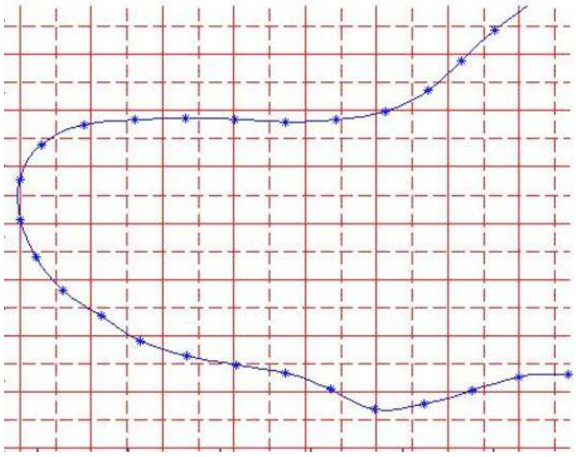

Figure 3.3: The Eulerian grid is shown in red. The solid lines mark grid cells, while the dotted lines pass through cell centers. The front is shown in blue, with asterisks for the markers. Between each marker, the position coordinates are tracked using cubic splines.

3.4 Computation of Surface Force

To track the surface force,

$$\mathbf{F}_s = \gamma\kappa\mathbf{n} + \nabla_s\gamma - gh(\rho_f - \rho_a)\mathbf{k}$$

given by Eq. (2.3), we follow the axially symmetric front tracking algorithm, presented by Zaleski and Popinet in 1999 [15]. We decompose the curvature term into radial and two dimensional components, and apply one of the Frenet-Serret formulas ($d\mathbf{t}/ds = \kappa_{2\mathrm{D}}\mathbf{n}$) to the 2D term:

$$\kappa\mathbf{n} = (\kappa_{\mathrm{axi}} + \kappa_{2\mathrm{D}})\,\mathbf{n} = \kappa_{\mathrm{axi}}\mathbf{n} + \frac{d\mathbf{t}}{ds} \quad . \tag{3.7}$$

Here, $\mathbf{t}$ is the unit tangent vector in the direction of increasing s. The radius $\kappa_{\mathrm{axi}}^{-1}$ of curvature with respect to the axis of symmetry goes from the point on the curve to the axis of symmetry along a perpendicular trajectory. Geometrically,

$$r\kappa_{\mathrm{axi}} = \cos\varphi = \frac{dz}{ds} \tag{3.8}$$

where φ is the angle the radius of curvature κ_{axi}^{-1} makes with the axis of symmetry. In addition, the gradient of the surface tension can be rewritten in terms of the unit tangent:

$$\nabla_s \gamma = \mathbf{t} \frac{d\gamma}{ds} \quad . \tag{3.9}$$

Now, write the average surface force $\overline{\mathbf{F}}_{ij}$ in grid cell i, j using equations (3.7), (3.8), and (3.9):

$$\overline{\mathbf{F}}_{ij} = \frac{1}{h^2} \iint_{\text{cell}} \delta_s \mathbf{F}_s dA = \frac{1}{h^2} \iint_{\text{cell}} \delta_s \left(\frac{\gamma}{r} \frac{dz}{ds} \mathbf{n} + \gamma \frac{d\mathbf{t}}{ds} + \mathbf{t} \frac{d\gamma}{ds} - gh(\rho_f - \rho_a)\mathbf{k} \right) dA \quad .$$

We can collapse two terms using the product rule:

$$\gamma \frac{d\mathbf{t}}{ds} + \mathbf{t} \frac{d\gamma}{ds} = \frac{d}{ds}(\gamma \mathbf{t}) \quad .$$

The delta function turns the area integral into a line integral along the interface. Altogether,

$$h^2 \overline{\mathbf{F}}_{ij} = \gamma(s_2)\mathbf{t}(s_2) - \gamma(s_1)\mathbf{t}(s_1) + \int_{s_1}^{s_2} \left(\frac{\gamma}{r} \frac{dz}{ds} \mathbf{n} - gh(\rho_f - \rho_a)\mathbf{k} \right) ds \tag{3.10}$$

where s_1, s_2 are the values of arc-length at which the front intersects the bounds of cell i, j.

Since the parametrization is in terms of arc-length,

$$\mathbf{t}(s) = \big(r'(s), z'(s)\big) \quad \text{and} \quad \mathbf{n}(s) = \big(-z'(s), r'(s)\big) \quad .$$

Thus, the surface force in each cell has the following expression in cylindrical coordinates:

$$\overline{\mathbf{F}}_{ij} \cdot \mathbf{e}_r = \gamma(s_2) r'(s_2) - \gamma(s_1) r'(s_1) - \int_{s_1}^{s_2} \frac{\gamma}{r} \Big(\frac{dz}{ds} \Big)^2 ds \tag{3.11}$$

$$\overline{\mathbf{F}}_{ij} \cdot \mathbf{k} = \gamma(s_2) z'(s_2) - \gamma(s_1) z'(s_1) + \int_{s_1}^{s_2} \left(\frac{\gamma}{r} \frac{dz}{ds} \frac{dr}{ds} - gh(\rho_f - \rho_a) \right) ds \quad . \tag{3.12}$$

Because we track the values of r, r', z, z' at intersections between the front and the grid, a numerical computation of the terms (3.11) and (3.12) can be done using trapezoidal integration and spline interpolation.

3.5 Projection Method for Pressure

The pressure is computed using a projection method developed by Brown, et al, in 2001 [34], which results in a Poisson equation for the pressure that enforces conservation of mass. This is inverted using iterative methods, executed on a linear multigrid, for computational efficiency.

Supposing, for a moment, we use a simple Euler timestep, the Navier-Stokes solver could be described as follows

$$\mathbf{u}^{t+1} = \mathbf{u}^t - \frac{\Delta t}{\rho} \nabla P + \Delta t f(\mathbf{u}^t) \tag{3.13}$$

where Δt is the time increment, t indexes the timestep, and the function f encompasses all of the forcing terms except the pressure. We wish to compute the pressure that will enforce continuity:

$\nabla \cdot \mathbf{u} = 0$. To accomplish this, we will need to deal with the divergence of the partially updated velocity, $\mathbf{u}^*$, that we obtain before taking the pressure into account. So define

$$\mathbf{u}^* = \mathbf{u}^t + \Delta t f(\mathbf{u}^t)$$

Then Eq. (3.13) becomes

$$\mathbf{u}^{t+1} = \mathbf{u}^* - \frac{\Delta t}{\rho} \nabla P \tag{3.14}$$

Taking the divergence of Eq. (3.14), we seek to solve the following Poisson equation

$$\nabla \cdot \mathbf{u}^{t+1} = \nabla \cdot \mathbf{u}^* - \Delta t \nabla \cdot \left(\frac{1}{\rho} \nabla P \right) = 0 \tag{3.15}$$

for the pressure, P. We apply Neumann conditions (no normal derivative) at the walls. Numerically, this gives rise to a finite difference equation:

$$\nabla^h \cdot (\rho_{i,j}^{-1} \nabla^h P_{i,j}) = \Delta t^{-1} \nabla^h \cdot (U^*_{i,j}, V^*_{i,j}) \tag{3.16}$$

where we use the derivatives, ∇^h, defined in §3.1. In keeping with our use of the MAC grid, the inverse density is evaluated on cell walls, along with the components of velocity (see figure 3.2). Eq. (3.16) can be written as an affine equation in terms of the component $P_{i,j}$:

$$A_{i,j} P_{i,j} + B_{i,j} = \phi_{i,j}$$

where

$$\begin{aligned}
A_{i,j} &= -\frac{r_i \rho^{-1}_{i-1/2,j} + r_{i+1} \rho^{-1}_{i+1/2,j}}{r_i h^2} - \frac{\rho^{-1}_{i,j-1/2} + \rho^{-1}_{i,j+1/2}}{h^2} \\
B_{i,j} &= \frac{r_i P_{i-1,j} \rho^{-1}_{i-1/2,j} + P_{i+1,j} r_{i+1} \rho^{-1}_{i+1/2,j}}{r_i h^2} + \frac{P_{i,j-1} \rho^{-1}_{i,j-1/2} + P_{i,j+1} \rho^{-1}_{i,j+1/2}}{h^2} \\
\text{and} \quad \phi_{i,j} &= \Delta t^{-1} \nabla^h \cdot (U^*_{i,j}, V^*_{i,j}) \quad .
\end{aligned}$$

A one-step inversion is not possible, since the constant term, $B_{i,j}$, depends pressure components $P_{i\pm1,j}, P_{i,j\pm1}$. This equation can be inverted iteratively, by putting $P^{(n+1)}_{i,j} = (\phi^{(n)}_{i,j} - B^{(n)}_{i,j})/A^{(n)}_{i,j}$.

A straightforward approach would be extremely costly in computational terms, requiring an enormous number of iterations to arrive at the correct, updated pressure. The linear multigrid for the Poisson equation reduces the workload enormously. The pressure is updated ("relaxed on") a few times, first on a full $2^N \times 2^N$ grid. The result is coarsened to a $2^{N-1} \times 2^{N-1}$ grid - and we relax on this grid a few times. This process is repeated until we arrive at a 2×2 grid, and the residuals are stored at each stage. The problem is then solved exactly on the 2×2 grid, using a large number of iterations. Next, we begin refining the grid again, by copying the newly computed pressure, and subtracting the previously stored residuals, until we again arrive at a $2^N \times 2^N$ grid. This entire process is repeated until the final residual is sufficiently small.

3.5.1 Pressure on a Stationary Drop

We validated our method for computing a discontinuous pressure field by computing the pressure field for a stationary spherical drop, centered on the axis. We used a cylindrical domain of $0 \le r \le 4$ and $0 \le z \le 8$, centered the drop at $(r, z) = (0, 4)$, and computed the pressure over one timestep for different resolutions. The drop radius used was $R_0 = 1$ and the surface tension was $\gamma = 10$, so that the pressure inside the drop should be $P_0 = 2\gamma/R_0 = 20$. This yields a theoretical pressure field

over the domain of $P_0\phi$, where ϕ is an indicator function that is 1 inside the drop and 0 outside. We compute the error as a function of the meshwidth, h, as

$$\epsilon_p(h) = \frac{\left\|P^c_{i,j} - P^{\text{th}}_{i,j}\right\|_p}{P_0} \quad \text{where} \quad P^{\text{th}}_{i,j} = \phi_{i,j} P_0. \tag{3.17}$$

Here, $\|\cdot\|_p$ is the p-norm of a grid function, and $\phi_{i,j}$ is a discrete indicator function, which returns the fraction of cell i, j that is inside the drop.

Table 3.2 gives the results for two norms: the 1-norm ($p = 1$) and the max norm ($p = \infty$). For $p = 1$, convergence is first order, but for the max norm, the error is not converging at all. In particular, the error takes the form of spikes on cells that intersect the interface. Although the proportion of the domain that is occupied by these spikes decreases with order 1, the magnitude of the spikes does not decrease with increasing resolution. This is a consequence of the discontinuity across the interface, and is unavoidable given the method we use.

Error vs Resolution in Pressure Computation

Meshwidth	1/8	1/16	1/32	1/64	1/128	1/256
Error (1-norm)	3.695×10^{-3}	2.150×10^{-3}	1.065×10^{-3}	5.95×10^{-4}	3.00×10^{-4}	1.55×10^{-4}
Max Error	0.271	0.299	0.280	0.328	0.359	0.364

Table 3.2: Error in pressure computation against meshwidth for a stationary spherical drop, computed over 1 timestep. The resolution is given by the meshwidth, h. The error is computed using Eq. (3.17), for $p = 1, \infty$.

3.6 Pressure Correction

Following Zaleski and Popinet (1999) [15], corrections are made that account for the discontinuous pressure jump at the interface. In the standard method, errors in computing the pressure jump at the interface result in significant spurious currents, which are orthogonal to the grid and are present even if the corresponding physical system is stationary. By correcting the standard computation with a much more careful accounting, Zaleski and Popinet managed to reduce the spurious currents by several orders of magnitude.

Let X be the point of intersection between the front and some horizontal line $z = z_j$, between the vertical lines $r = r_{i-1/2}, r = r_{j+1/2}$. Denote by A and B, respectively, the intersections of these lines with $z = z_j$ (see Figure 3.4). Then the closest pressure node will be $P_{i,j}$, and the traditional method for computing the pressure jump across the front is given by

$$\int_B^A Pdr \approx P^0_{i,j} = \begin{cases} (P_{i,j} - P_{i-1,j})\, h & \text{if} \quad AX < h/2 \\ (P_{i+1,j} - P_{i,j})\, h & \text{if} \quad AX \geq h/2 \end{cases}$$

A much better approximation is obtained by using the distances AX, BX as weights, placing

$$\int_B^A Pdr \approx P^e_{i,j} = \begin{cases} AX \cdot P_{i-1,j} + BX \cdot P_{i,j} & \text{if} \quad AX < h/2 \\ AX \cdot P_{i,j} + BX \cdot P_{i+1,j} & \text{if} \quad AX \geq h/2 \end{cases}$$

The corresponding corrections to the normal pressure increment $hP_{i,j}$ are defined as

$$I_{i,j}[P] = P^e_{i,j} - hP_{i,j} = \begin{cases} AX(P_{i,j-1} - P_{i,j}) & \text{if} \quad AX < h/2 \\ BX(P_{i,j+1} - P_{i,j}) & \text{if} \quad AX \geq h/2 \end{cases}$$

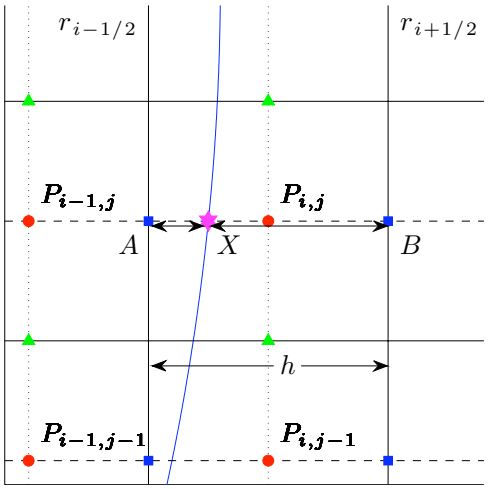

Figure 3.4: A horizontal pressure correction for the pressure jump across the front, centered at X. In this case, $AX < h/2$, so the pressure correction is $I_{i,j} = AX(P_{i,j-1} - P_{i,j})$.

Then the gradient, approximated as a backward difference,

$$D_- I_{i,j} = \frac{I_{i,j} - I_{i,j-1}}{\Delta z}$$

is added in the velocity $V_{i-1/2,j-1/2}$ in the Navier-Stokes solver, as a forcing term. Vertical pressure corrections are computed similarly.

3.6.1 Spurious Currents Near a Stationary Drop

The effectiveness of our pressure correction routine can be measured by how well it suppresses spurious currents near a stationary drop. We ran simulations of a spherical drop of radius $R_0 = 1$ at rest in the absence of gravity, on a domain of $0 \le r \le 4$ and $0 \le z \le 8$. As with the pressure test, the drop is centered on the axis, at $z_0 = 4$. The viscosity used is $\mu = 0.05$, and the surface tension is $\gamma = 10$. We measure the spurious currents using the 1-norm of the array of velocity magnitudes, computed at cell centers. In particular, we put

$$U_{\max} = \left\| \sqrt{U^2_{i+1/2,j} + V^2_{i,j+1/2}} \right\|_1 \quad . \tag{3.18}$$

The half-indices in equation (3.18) represent values averaged over the cell center, and were chosen to make sure that the velocity magnitude resides at cell centers on the MAC grid.

Figure 3.5 show the magnitude of the spurious currents against the number of timesteps taken, for a meshwidth of $h = 1/32$. The spurious currents develop unevenly in time, and level off before 3000 timesteps, at which point they are quite large. We ran simulations of stationary drops for 3000 timesteps with and without pressure corrections, and measured the spurious currents at the end of the simulation. The results, shown in table 3.3, demonstrate that the pressure correction reduces the spurious currents by 2 or 3 orders of magnitude.

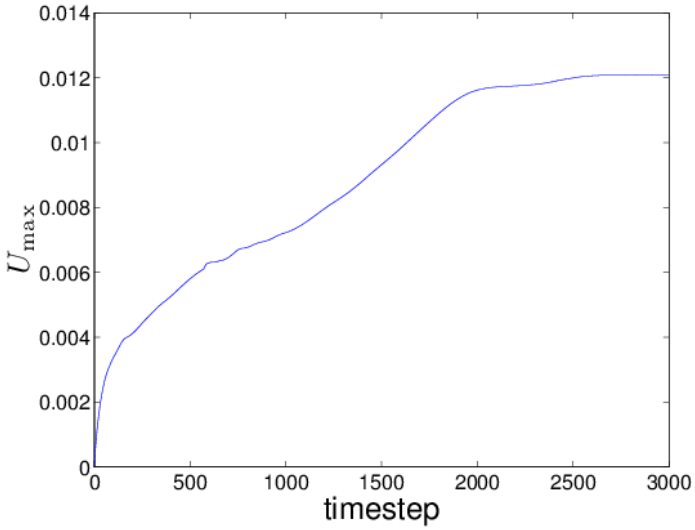

Figure 3.5: The magnitude of spurious currents around a stationary drop, for a meshwidth of $h = 1/32$. $U_{\max}$ is described in equation (3.18).

Magnitude of Spurious Currents

Meshwidth	1/8	1/16	1/32	1/64	1/128	1/256
$U_{\max}$ Uncorrected	0.0811	0.0215	0.0121	2.50×10^{-3}	7.46×10^{-4}	1.79×10^{-4}
$U_{\max}$ Corrected	2.06×10^{-4}	1.50×10^{-4}	1.31×10^{-5}	5.97×10^{-6}	7.22×10^{-7}	2.79×10^{-7}
Improvement	393	143	922	419	1032	641

Table 3.3: The magnitude of spurious currents around a stationary drop, after 3000 timesteps, with and without pressure corrections. The improvement is defined as $U_{\max}$ without corrections divided by $U_{\max}$ with corrections. $U_{\max}$ is described in equation (3.18).

3.7 Surfactant Tracking

Because we already keep track of the position of the markers on the front, it is convenient to track surfactant using a Lagrangian approach that automatically conserves mass in the absence of sorption. The surfactant concentration at each marker is advanced in time in three stages (see figure 3.6, left): updating the surfactant concentrations using local masses computed before and after advancing the front; redistributing the front and the surfactant masses to maintain equal spacing between markers and conserve surfactant mass; and adding forcing terms, such as diffusion and sorption, to the new concentration. For clarity, we use a different notation for each stage of advancement:

$$\Gamma_j^{t-1} \xrightarrow{\text{advance front, update using local masses}} \Gamma_j^* \xrightarrow{\text{redistribute using total masses}} \Gamma_k' \xrightarrow{\text{add sorption and diffusion}} \Gamma_k^t \quad .$$

In what follows, we discuss how to track surfactant on a single spheroidal drop, centered on the axis. Tracking surfactant on other types of fronts, such as a drop merging with a reservoir, is done similarly.

At time $t-1$, we have a front consisting of n^{t-1} markers, indexed by j, where $0 \le j \le n^{t-1}$. We compute the mass of surfactant near the j^{th} marker at time $t-1$:

$$m_j^{t-1} = \Gamma_j^{t-1} \Delta A_j^{t-1} \tag{3.19}$$

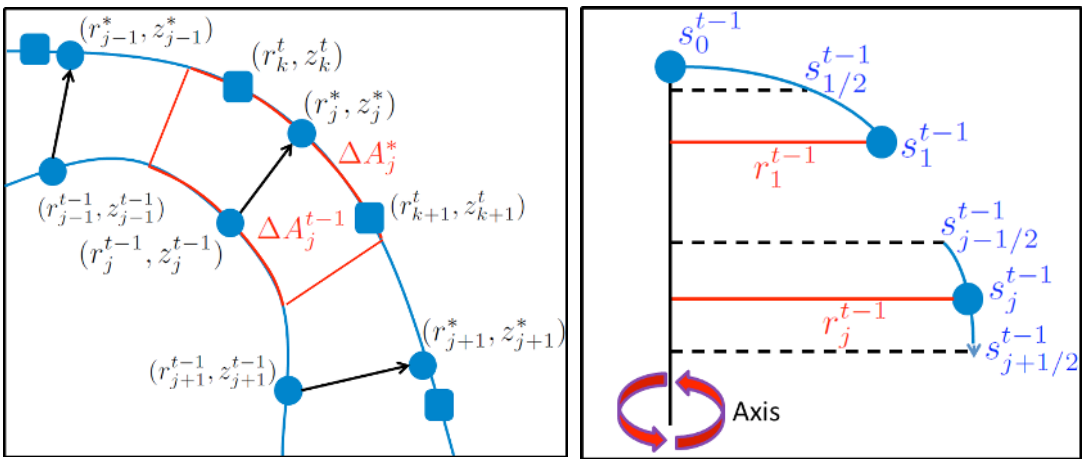

Figure 3.6: Left: An illustration of the front being advanced. The rounded squares represent redistributed markers. Right: An illustration of the area elements being computed. The first (top) and last area elements are approximated as portions of a small cap on the axis. In between (bottom), the area elements are approximated as revolutions of arcs between the points described by $s^{t-1}_{j-1/2}$ and $s^{t-1}_{j+1/2}$. The black dotted lines bound the relevant areas.

where Γ^{t-1}_j is the surfactant concentration at the j^{th} marker at time $t-1$, and ΔA^{t-1}_j represents the associated area element (see figure 3.6, right). On the axis, ΔA^{t-1}_j is approximated by the surface area of a small cap about the axis:

$$\Delta A^{t-1}_0 = \frac{1}{4}\pi s^{t-1}_1 r^{t-1}_1 \quad \text{and} \quad \Delta A^{t-1}_{n^{t-1}-1} = \frac{1}{4}\pi(s^{t-1}_{n^{t-1}-1} - s^{t-1}_{n^{t-1}-2}) r^{t-1}_{n^{t-1}-2} \quad .$$

Away from the axis, it is a narrow strip made by revolving the arc from $s^{t-1}_{j-1/2}$ to $s^{t-1}_{j+1/2}$ about the axis:

$$\Delta A^{t-1}_j = 2\pi r^t_j \Delta s^{t-1}_j \quad .$$

Here, r^{t-1}_j is the distance of the j^{th} marker to the axis at time $t-1$, and $\Delta s^{t-1}_j = \frac{1}{2}(s^{t-1}_{j+1} - s^{t-1}_{j-1})$ for $1 \le j \le n^{t-1} - 2$. After the markers are advected with the fluid to positions (x^*_j, y^*_j) and new arc-lengths s^*_j are computed, but before they are redistributed, we update surfactant concentration to a temporary value Γ^*_j, by inverting Eq. (3.19):

$$\Gamma^*_j = \frac{m^{t-1}_j}{\Delta A^*_j} = \frac{\Delta A^{t-1}_j}{\Delta A^*_j}\Gamma^{t-1}_j \quad . \tag{3.20}$$

Notice that Eq. (3.20) conserves the mass associated to each marker *by definition*.

Next, we redistribute the markers to equally spaced positions, (x^t_k, y^t_k), and compute new arc-lengths, s^t_k, associated to these positions. The redistributed markers are indexed by k, such that $0 \le k \le n^t - 1$, where n^t is the new number of markers. We also redistribute the surfactant concentrations in such a way as to conserve surfactant mass. We begin by forming arc-length intervals of

$$\Delta s^*_j = \frac{1}{2}(s^*_{j+1} - s^*_{j-1}) \quad \text{and} \quad \Delta s^t_k = \frac{1}{2}(s^t_{k+1} - s^t_{k-1})$$

before and after redistribution, respectively, and write the arc-lengths midway between markers as

$$s^*_{j-1/2} = \frac{s^*_{j-1} + s^*_j}{2} \quad \text{and} \quad s^t_{k-1/2} = \frac{s^t_{k-1} + s^t_k}{2} \quad .$$

We would like to chose our redistributed surfactant concentrations, Γ'_k, to enforce mass conservation. This can be done by going through the markers and choosing the redistributed surfactant concentrations to conserve total mass up to that point. Since the first marker doesn't change, we set $\Gamma'_0 = \Gamma^*_0$. This fixes the redistributed mass in a small area about the axis of radius $r^t_1/2$ to

$$m'_0 = \frac{1}{4}\pi s^t_1 r^t_1 \Gamma^*_0$$

Now, suppose $1 \leq k$. Each marker k is associated to a surfactant concentration Γ'_k, and a mass element m'_k on a strip between $s^t_{k-1/2}$ and $s^t_{k+1/2}$. We begin by computing the total surfactant mass up to $s^t_{k-1/2}$ using redistributed surfactant concentrations:

$$M'_{k-1/2} = 2\pi \int_0^{s^t_{k-1/2}} \Gamma(s) r(s) ds = \frac{1}{4}\pi s^t_1 r^t_1 \Gamma'_0 + 2\pi \sum_{i=1}^{k-1} \Gamma'_i r^t_i \Delta s^t_i \quad . \tag{3.21}$$

Next, we compute the surfactant mass up to $s^t_{k+1/2}$ using the non-redistributed markers:

$$M'_{k+1/2} = 2\pi \int_0^{s^t_{k+1/2}} \Gamma(s) r(s) ds = 2\pi \int_0^{s^*_{J-1/2}} \Gamma(s) r(s) ds + 2\pi \int_{s^*_{J-1/2}}^{s^t_{k+1/2}} \Gamma(s) r(s) ds$$

where $J = \max\{j : s^*_{j-1/2} \leq s^t_{k+1/2}\}$. The above integrals on the right can be computed separately:

$$M^*_{J-1/2} \equiv 2\pi \int_0^{s^*_{J-1/2}} \Gamma(s) r(s) ds = \frac{1}{4}\pi s^*_1 r^*_1 \Gamma^*_0 + 2\pi \sum_{1 \leq j < J} \Gamma^*_j r^*_j \Delta s^*_j$$

$$M_{\text{gap}} \equiv 2\pi \int_{s^*_{J-1/2}}^{s^t_{k+1/2}} \Gamma(s) r(s) ds = 2\pi \Gamma^*_J r^*_J \Delta s_{\text{gap}} \quad \text{where} \quad \Delta s_{\text{gap}} = s^t_{k+1/2} - s^*_{J-1/2}$$

Then the new surfactant concentration, Γ'_k, should correspond to a mass of $2\pi r^t_k \Gamma'_k \Delta s^t_k = M'_{k+1/2} - M'_{k-1/2}$. Solve to obtain

$$\Gamma'_k = \frac{M'_{k+1/2} - M'_{k-1/2}}{2\pi r^t_k \Delta s^t_k} \quad . \tag{3.22}$$

Continuing in this manner, it is possible to choose the redistributed surfactant concentrations for all of the markers so as to conserve surfactant exactly. However, because the mass element associated to the last marker is quite small in comparison to other mass elements, this will result in sharp gradients in surfactant concentration near the last marker. As such, instead of moving from the top of the drop to the bottom, we move independently from the ends (top and bottom) toward the middle. It is convenient to choose our new number of markers to be odd: $n^t = 2\ell + 1$ where ℓ is the index of the middle marker, which has the greatest associated area element. Thus, we apply the method described in the previous paragraph to all markers indexed by k such that $0 \leq k < \ell$, and we apply a similar method to the markers by k such that $\ell < k \leq n^t - 1$, except that we move backward from the last marker at $k = n^t - 1$. The middle marker is chosen to conserve total surfactant mass:

$$\Gamma'_k = \frac{M^* - M'_{\ell+1/2} - M'_{\ell-1/2}}{2\pi r^t_\ell \Delta s^t_\ell} \quad , \tag{3.23}$$

where M^* is the total surfactant mass before redistribution; $M'_{\ell-1/2}$ is the total surfactant mass from the top to $s_{\ell-1/2}$, computed after redistribution by moving from $k = 0$ to $k = \ell - 1$; and $M'_{\ell+1/2}$ is the total surfactant mass from the bottom to $s_{\ell+1/2}$, computed after redistribution by moving from $k = n^t - 1$ to $k = \ell + 1$.

After redistributing, we add the diffusion and sorption terms:

$$\Gamma_k^t = \Gamma'_k + \Delta t\big(k_D \nabla^2 \Gamma'_k + J(\Gamma'_k, (\Lambda|_s)_k)\big)$$

where k_D is a diffusion coefficient. The diffusive term is a discretization of the Laplacian

$$\nabla^2 \Gamma = \frac{1}{r}\frac{\partial}{\partial s}\left(r\frac{\partial \Gamma}{\partial s}\right)$$

(here we have neglected the time dependence). We approximate as

$$(\nabla^2\Gamma)_k = \frac{r_{k+\frac{1}{2}} D_{k+\frac{1}{2}} - r_{k-\frac{1}{2}} D_{k-\frac{1}{2}}}{r_k(s_{k+\frac{1}{2}} - s_{k-\frac{1}{2}})} \quad \text{where} \quad D_{k+\frac{1}{2}} = \frac{\Gamma_{k+1} - \Gamma_k}{s_{k+1} - s_k} \quad . \tag{3.24}$$

At the axis, we must use an alternate method, because $r = 0$. So use L'hopitals rule to compute an alternate representation, and apply the fact that $\frac{\partial r}{\partial s} = \pm 1$ at the axis:

$$\lim_{r\to 0} \nabla^2\Gamma = \lim_{r\to 0}\left(\frac{\partial^2\Gamma}{\partial s^2} \pm \frac{1}{r}\frac{\partial \Gamma}{\partial s}\right) = \lim_{r\to 0}\left(\frac{\partial^2\Gamma}{\partial s^2} \pm \frac{\frac{\partial}{\partial s}\frac{\partial \Gamma}{\partial s}}{\frac{\partial}{\partial s} r}\right) = 2\frac{\partial^2\Gamma}{\partial s^2}\bigg|_{r=0} \quad .$$

With symmetry at the axis, the end terms become

$$(\nabla^2\Gamma)_0 = \frac{4}{s_1^2}(\Gamma_1 - \Gamma_0) \quad \text{and} \quad (\nabla^2\Gamma)_{n-1} = -\frac{4(\Gamma_{n-1} - \Gamma_{n-2})}{(s_{n-1} - s_{n-2})^2} \tag{3.25}$$

where the markers are indexed from $k = 0$ to $k = n - 1$. Notice that the above form for $(\nabla^2\Gamma)_{n-1}$ is valid whether or not the front ends on the axis, so long as the front is horizontal at the wall. This diffusion is mass-conserving if the arc-length is constant between different markers - which is enforced by redistributing the markers every timestep. To see this, sum over the n markers (again, ignoring the time dependence):

$$\begin{aligned}
M_{\text{New}} &= \sum_{k=0}^{n-1} \left(\Gamma_k + \Delta t k_D (\nabla^2\Gamma)_k\right) \Delta A_k \\
&= \sum_{k=0}^{n-1} \left(\frac{m_k}{\Delta A_k} + \Delta t k_D (\nabla^2\Gamma)_k\right) \Delta A_k \\
&= \sum_{k=0}^{n-1} m_k + \Delta t k_D \Bigg(\sum_{k=1}^{n-2} (2\pi r_k \Delta s) \frac{r_{k+\frac{1}{2}} D_{k+\frac{1}{2}} - r_{k-\frac{1}{2}} D_{k-\frac{1}{2}}}{r_k \Delta s} \\
&\quad + 4\pi(\Delta s/2) r_{1/2} \frac{\Gamma_1 - \Gamma_0}{\Delta s^2} - 4\pi(\Delta s/2) r_{n-3/2} \frac{\Gamma_{n-1} - \Gamma_{n-2}}{\Delta s^2} \Bigg) \quad \text{(By Eq. (3.24) and (3.25))} \\
&= M_{\text{Old}} + 2\pi \Delta t k_D \left(r_{n-\frac{3}{2}} D_{n-\frac{3}{2}} - r_{\frac{1}{2}} D_{\frac{1}{2}} + \frac{r_{1/2}}{\Delta s}(\Gamma_1 - \Gamma_0) - \frac{r_{n-3/2}}{\Delta s}(\Gamma_{n-1} - \Gamma_{n-2}) \right) \\
&\qquad \text{(Telescoping the sum)} \\
&= M_{\text{Old}} \quad .
\end{aligned}$$

3.8 Surfactant Exchange Terms

Numerically, we have two exchange terms that look very different: a term $(J_s)_k^t$ that is added to the markers, to track changes on the surfactant concentration on the surface; and a term $(J_b)_{i,j}^t$ that is

added to the cells crossed by the interface, to track changes in the surfactant concentration in the bulk. The exchange term for the bulk can be computed by averaging over one grid cell. The delta function converts the area integral into an integral along the front:

$$(J_b)_{i,j} = \frac{1}{h^2} \iint_{\text{cell}} \delta_s J(\Gamma, \Lambda|_s) dA = \frac{1}{h^2} \int_{s_1}^{s_2} J(\Gamma, \Lambda|_s) ds$$

where h is the mesh-width and s_1, s_2 are the locations (measured by arc-length from the crest) where the front enters and leaves the cell. The exchange term for the surface can be accurately computed by evaluating a local integral about each marker:

$$(J_s)_k = \frac{1}{\Delta s_k} \int_{s_{k-1/2}}^{s_{k+1/2}} J(\Gamma, \Lambda|_s) ds$$

where $\Delta s_k = s_{k+1/2} - s_{k-1/2}$. Both surface integrals are computed numerically using trapezoidal integration. $J(\Gamma, \Lambda|_s)$ is given by Eq. (2.10), and depends only on arc-length. The surface concentration, $\Gamma(s)$, is obtained by linear interpolation from the markers, and the bulk concentration, $\Lambda|_s$, is obtained using bilinear interpolation from adjacent cells.

3.8.1 Desorption Test

We test our method of computing the surfactant exchange by computing an exact solution for a simple test case. Our simple test case involves a drop at rest in a stationary fluid that only undergoes desorption. In particular, we set $k_{\text{ad}} = 0$ in Eq. (2.10), to get

$$J(\Gamma, \Lambda|_s) = -k_{\text{de}}\Gamma \tag{3.26}$$

We assume that initially the surfactant is uniformly distributed on the drop surface, with $\Gamma(s, t = 0) = 1$. Then the surfactant mass on the surface and in the bulk at time t are given respectively by

$$M_\Gamma(t) = 4\pi R_0^2 e^{-k_{\text{de}}t} \quad \text{and} \quad M_\Lambda(t) = 4\pi R_0^2 (1 - e^{-k_{\text{de}}t}) \quad . \tag{3.27}$$

We allowed surfactant to desorb from the surface until $t = 3$, computed the total surfactant mass on the surface and in the bulk, and compared them against the values obtained from Eq. (3.27). The results, shown in table 3.4, demonstrate first order accuracy.

Resolution	Percent Error of	
	M_Γ	M_Λ
$(32/4)^2$	3.6×10^{-4}	0.0116
$(64/4)^2$	1.2×10^{-4}	0.0040
$(128/4)^2$	4.3×10^{-5}	0.0014
$(256/4)^2$	1.5×10^{-5}	5.0×10^{-4}

Table 3.4: Error in surfactant mass versus resolution for desorption from the surface of a stationary drop. The error is measured as $(M_c - M_{\text{th}})/M_{\text{th}}$, where M_c is the surfactant mass obtained from the simulation, and M_{th} comes from Eq. (3.27), at $t = 3$. A desorption rate of $k_{\text{de}} = 1$ was used.

3.8.2 Surfactant Mass Conservation

We also tested the conservation of total surfactant mass for the full sorption routine, with $k_{\text{de}} = 0.02$ and $k_{\text{ad}} = 0.2$. In this case, we made our test more rigorous by introducing motion to the drop.

In particular, we started the simulation with a spheroidal drop with aspect ratio $R_z/R_r = 1.5$ and allowed the system to relax over three units of time. We started the simulation with no surfactant in the bulk and measured our error against the total initial surfactant mass. We found that the error is small, and decays significantly with resolution - though the decay appears uneven (table 3.5). The percent change in bulk, surface, and total surfactant mass for a resolution of $(128/4)^2$ has also been plotted (figure 3.7).

Resolution	$\Delta M(t)/M(t=0)$
$(32/4)^2$	1.6×10^{-3}
$(64/4)^2$	1.3×10^{-3}
$(128/4)^2$	7.24×10^{-4}
$(256/4)^2$	4.48×10^{-4}

Table 3.5: Percent change in surfactant mass for an oscillating drop undergoing sorption ($k_{\text{de}} = 0.02$ and $k_{\text{ad}} = 0.2$), at $t = 3$.

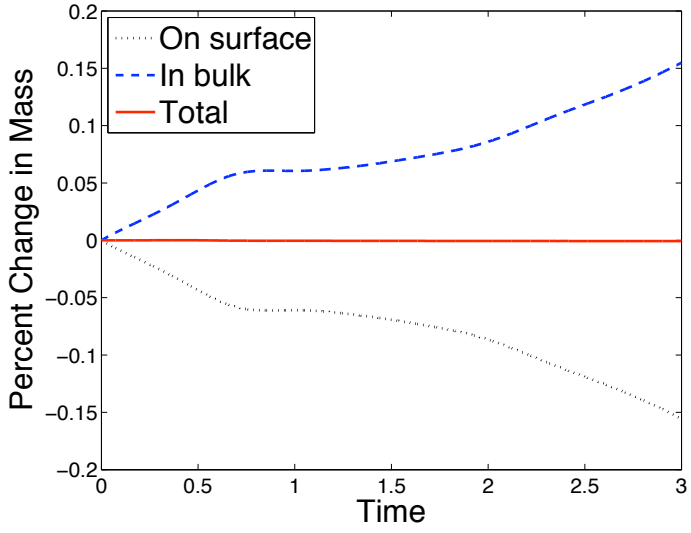

Figure 3.7: Percent change in surfactant mass for an oscillating drop undergoing sorption ($k_{\text{de}} = 0.02$ and $k_{\text{ad}} = 0.2$).

3.9 Oscillations of an Irrotational Drop

As a dynamic validation of our method, we studied the oscillations of a perturbed spherical drop, whose oscillation frequency has been analyzed for certain specific cases [40]. For a liquid drop surrounded by a gas of negligible density and viscosity, the oscillation frequency of the n^{th} mode of frequency is found to be

$$\omega_n^2 = \frac{\gamma}{\rho R_0^3}(n+2)n(n-1) \tag{3.28}$$

where γ is the surface tension, R_0 is the drop radius, and ρ is the liquid density. We computed the oscillation frequency for the primary mode of oscillation ($n = 2$) of a perturbed liquid drop with an initial aspect ratio of 1.05 and a dimensionless viscosity of $\mu_d = 0.02$, surrounded by gas. At a resolution of $(512/5.0)^2$, the accuracy obtained was excellent, differing from the theoretical

Liquid/Liquid System		
Resolution	ΔM	ΔE
$(32/5.0)^2$	2.24%	0.43%
$(64/5.0)^2$	0.28%	0.27%
$(128/5.0)^2$	0.24%	0.072%
$(256/5.0)^2$	0.073%	0.039%
$(512/5.0)^2$	0.038%	0.015%

Liquid/Gas System		
Resolution	ΔM	ΔE
$(32/5.0)^2$	3.86%	4.36%
$(64/5.0)^2$	1.68%	3.50%
$(128/5.0)^2$	1.40%	2.45%
$(256/5.0)^2$	0.62%	1.50%
$(512/5.0)^2$	0.044%	0.18%

Table 3.6: Percent variations in interior fluid mass, M, and energy budget, E, for a pair of nearly spherical merging drops, coated in surfactant, after 3.0 time units. For the liquid/liquid system, the density and viscosity of the drops and the ambient fluid are identical, while for the liquid/gas system the merging drops have a density and viscosity that are 10 times greater than that of the surrounding fluid. In all cases the viscosity of the drops was set to $\mu_d = 0.02$, we used a coefficient of $\beta = 0.1$ for the surfactant relation (2.14), and no gravity. The domain used had radial width $L_r = 5.0$ and height $L_z = 5.0$; the configuration of merging drops was placed in the interior.

solution by no more than 0.33%. Unfortunately, because the perturbations of the drop were small in comparison to the drop size, the drop oscillations could not be resolved for resolutions below $(512/5.0)^2$.

3.10 Additional Conservation Properties

3.10.1 A Pair of Merging Drops

A direct validation of our method as a whole may be obtained by verifying conservation of drop mass, M, and the energy, E, of the system. Energy can be tracked using an energy budget [39] for a multiphase flow system involving two immiscible fluids, and accounting for possible variations in density and viscosity. Thus, we estimate the accuracy of our code by computing the relative variation of a quantity $X(t)$, as

$$\Delta X = \frac{\max_t(X(t)) - \min_t(X(t))}{X(0)}$$

To make this validation applicable to the partial coalescence problem, we tested the code by running it for $t = 3.0$ units of nondimensional time - most of the trials we ran studying partial coalescence ran for 2 to 3 units of time. We modeled three setups: a perturbed drop, with initial aspect ratio 2.0, allowed to relax under the influence of surface tension; a "peanut configuration" consisting of two nearly spherical drops which have begun merging and are allowed to relax over time; and a spherical drop allowed to fall to the ground (no-slip and no penetration boundary), and bounce.

Table 3.6 shows the variations of fluid mass, surfactant mass, and energy budget against resolution for the peanut configuration. The results for the stretched and falling drop were similar. In all cases, fluid mass, surfactant mass, and energy budget converge with increasing resolution, achieving very good accuracy with a resolution of $(512/5.0)^2$. The errors are larger for the liquid/gas system - a fact which we attribute to computational difficulties arising from the sheer drop in pressure, density, and viscosity across the interface. In particular, the viscous stress tensor is discontinuous across the interface, due to the discontinuity in the viscosity. Thus, when we take the divergence of the stress tensor to obtain the viscous term in the Navier-Stokes, we introduce errors near the interface.

Similarly, the inverse density multiplies the forcing terms in the Navier-Stokes - and thus, the density discontinuity introduces numerical errors near the interface.

Also in the case of the liquid/gas system, conservation properties are relatively poor for resolutions up to and including $(256/5.0)^2$; but dramatically improve upon increasing resolution to $(512/5.0)^2$, typically by a factor of about 10. For all problems involving a liquid/gas system, we use a resolution of $(512/5.0)^2$. For the most part, both cases exhibit first order convergence for fluid mass, surfactant mass, and energy. A notable exception occurs when moving from a resolution of $(64/5)^2$ to $(128/5)^2$, in which case improvements in mass conservation were marginal. We believe this is due to the complexity of the code. As resolution improves, more components attain a minimal level of accuracy to achieve first order convergence. By the time we reach a resolution of $(256/5)^2$ all convergence is first order, and are always within 2% of exact conservation for all the regimes considered at a resolution of $(512/5.0)^2$.

3.10.2 A Rising Drop

We also ran simulations of a drop rising through a sharp density stratification, to determine conservation properties for problems similar to our application to rising drops. The cylindrical domain used had a radius of 4 drop radii and a height of 8 drop radii. The drop was allowed to rise from a height 1.5 to 6.5 drop radii. The drop density used was 1, while the density of the lower ambient was 1.1, and the density of the upper ambient was 1.05. The pycnocline (linear density gradient) was centered at $z = 4$ drop radii, with a width of 0.1 drop radii. In addition, the drop was coated with insoluble surfactant. We used an equilibrium surface tension of $\gamma_0 = 5$, a viscosity of $\mu = 1$, and an elasticity coefficient of $\beta = 0.2$. The results, shown in table 3.7, show first order convergence in both mass and energy conservation.

Resolution	ΔM	ΔE
$(16/4.0)^2$	1.2%	10.8%
$(32/4.0)^2$	0.61%	7.53%
$(64/4.0)^2$	0.20%	3.62%
$(128/4.0)^2$	0.10%	1.61%

Table 3.7: Percent variations in interior fluid mass, M and energy budget, E, for a drop rising through a linear density stratification, in which the density decreased sharply from 1.1 times the drop density to 1.05 times the drop density. We set $\gamma_0 = 5$, $\mu = 1$, and $\beta = 0.2$.

Chapter 4

Coalescing Drops and Bubbles

4.1 The Problem of Partial Coalescence

The coalescence of droplets has been widely studied, due to applications to foams and emulsions [41], as well as raindrop formation in clouds [42] and other aerosols, including mists [43], and pollutants in the earth's atmosphere [44]. It is known to play a role in the formation of vortex rings [45], which have been studied for more than a century [46], and to impact mixing in microfluidic devices [47]. Despite the considerable interest the subject has generated, most previous work has been limited to idealized circumstances. In particular, few studies have accounted for the effects of surfactants. Using our method, which we described in Chapter 3, we provide a more realistic description of partial coalescence, in contrast to the idealized, surfactant free, one given in previous studies. Applications such as ink jet printing, micro-fluidic devices, and natural set-ups such as raindrops and ocean mist, where partial coalescence takes place can be better predicted if an understanding of the effects of surfactants is attained.

The outcome of a collision between two fluid bodies depends significantly on the impact velocity. At high impact velocity, splashing, bouncing, coalescence, temporary coalescence, and fragmentation may occur [48–50]. At low velocities, a drop may rest on a reservoir without coalescing for up to a few seconds. This phenomena was first reported by Reynolds in 1881 [51], and has subsequently been investigated in some detail [52–54]. We focus here on drops and bubbles coalescing with a reservoir at a low impact velocity. Even when the contact velocity is negligible, merging drops may exhibit a curious and counterintuitive behavior, known as partial coalescence [54], in which a drop merging with another fluid body pinches off to form a smaller daughter drop before the merging process is complete. In the presence of gravity, the daughter drops bounce on the interface, before undergoing coalescence themselves. In 2000, a sequence of up to five self-similar partial coalescence events [55] was observed. The size [56] and jump height [57] of the daughter drop between coalescence events have been carefully studied. The residence time of a drop on a reservoir has been examined [58], as well as the duration of the merging process [55]. In all those experimental studies, fluid interfaces were carefully kept surfactant-free.

The mechanism for partial coalescence was explained in 2006 by Blanchette and Bigioni [59]. The nature of coalescence, partial or total, is a consequence of a competition between surface tension at the top of the drop, which drives total merging, and at the base of the drop, which favors pinch off. In the absence of inertial forces, the surface tension at the crest of the drop dominates, and

coalescence is total. However, in inertial regimes, vigorous capillary waves generated by the rapid motion involved in the initial merging travel up to the crest of the drop, stretching it vertically, and delaying total coalescence. This allows pinch off to occur at the base. This effect is seen in figure 4.1, which shows the partial coalescence of a drop without surfactant, in an inertial regime. Because viscosity dampens capillary waves, partial coalescence will not occur in sufficiently viscous regimes. Having determined the importance of viscosity, investigators have further examined the parameter regime of partial coalescence, looking at gravity effects and the relative densities and viscosities of the drop, reservoir, and ambient fluid [60, 61].

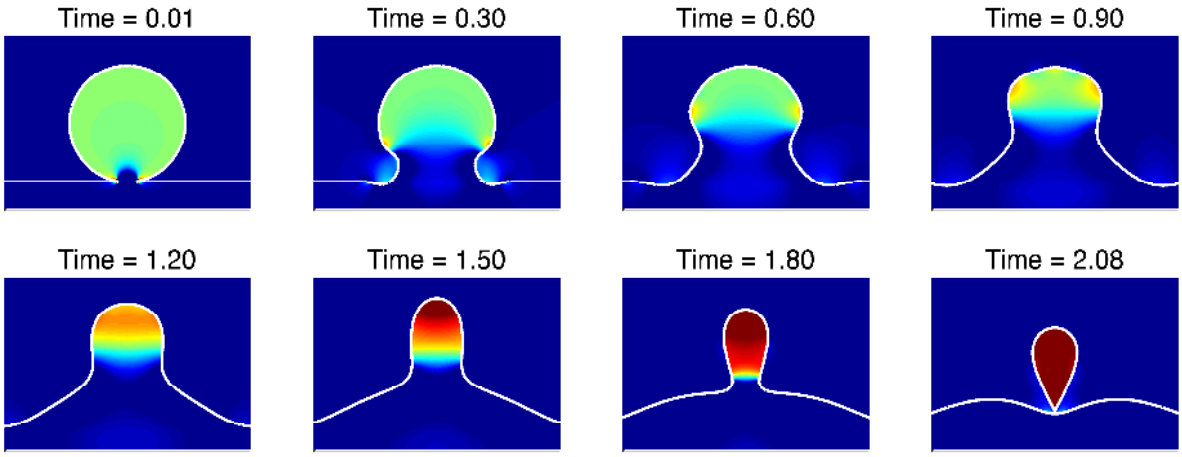

Figure 4.1: Pressure plots showing a time sequence of partial coalescence of a drop with a reservoir, in the absence of surfactant. The coloring shows the fluid pressure and the interface is shown in white. The interior and exterior fluids have identical viscosity and density; the Ohnesorge number used is $\mathrm{Oh} = 0.027$, and gravity is absent. The resolution used was $(512/5.0)^2$.

Here, we investigate the effects of the presence of surfactants on partial coalescence. In general, surfactant concentrations do not remain constant, leading to local surface tension variations. The effects on coalescence of surface tension variations due to compositional differences between the drop and the reservoir have also been studied [35, 62]. It was found that partial coalescence is favored when the drop has a higher surface tension than the reservoir, and that pinch off will not occur at all if the drop surface tension is sufficiently high relative to that of the reservoir. However, to the best of our knowledge, the effects of surfactants on partial coalescence have yet to be considered.

4.2 Setup

We consider two similar, but physically distinct setups. The first consists of a liquid drop surrounded by air, merging with a reservoir of the same liquid. The second consists of a soap bubble merging with a horizontal soap film, suspended in air. In both cases, surfactants may be present on all interfaces. We will use the term "drop" to refer to both the drop and bubble, and we will refer to both the reservoir and suspended film as a "reservoir". However, when only the soap film is intended, we will use the terms "bubble" and "film". We will use the phrases "liquid drop" and "liquid reservoir" when we wish to clarify that we are excluding the soap film.

We consider that the drop and reservoir are initially at rest. Unless otherwise specified, we begin our simulations with a horizontal reservoir and a spherical drop, with surfactant concentration

uniform on the drop and reservoir, and neglect gravity. This set up will be referred to as the base case. We begin our simulations shortly after merging, so that the drop and the reservoir are connected by a thin neck. In our model, we distinguish an exterior fluid with density and viscosity ρ_E, μ_E, from an interior fluid, having density and dynamic viscosity ρ_I, μ_I - common to both the drop and the reservoir (see figure 3.1). In the case of the soap film, the interior and exterior fluids are both air, so at room temperature and atmospheric pressure, $\mu_I = \mu_E \approx 1.81 \times 10^{-5}$Pa s and $\rho_I = \rho_E \approx 1.25\text{kg/m}^3$. For the liquid drop, the density and viscosity of the interior fluid may vary, but in general, $\rho_I \gg \rho_E$ and $\mu_I \gg \mu_E$. To account for the presence of two interfaces in a soap film, we introduce a variable N_f, representing the number of interfaces per front. In the case of the soap film, $N_f = 2$, while in the case of the liquid drop, $N_f = 1$.

For an interface of air with soapy water, the surface tension will range from $\gamma_0 \approx 7.2 \times 10^{-2}$N/m in the surfactant-free case, to $\gamma_0 \approx 3.0 \times 10^{-2}$N/m near the maximum packing concentration, which has a typical value of $\Gamma_\infty \approx 2 \times 10^{-10}\text{mol/cm}^2$ [11]. For soap films under the influence of gravity, we also add a film thickness, $h(s)$, to track the weight of the film. The film density, ρ_f, is assumed constant. If the film consists of soapy water, a typical density is $\rho_f \approx 10^3\text{kg/m}^3$, while the thickness has a typical value of $h_0 \approx 10^{-6}$m. We do not model the bursting of the film, and thus assume that the film remains unbroken.

4.3 Dimensionless Governing Equations

We use the drop radius, R_0, as a lengthscale. Because there is no natural velocity scale for the problem, we use a timescale, t_0, to be determined later:

$$\nabla_{\text{new}} = R_0 \nabla_{\text{old}} \qquad \kappa_{\text{new}} = R_0 \kappa_{\text{old}} \qquad t_{\text{new}} = t_{\text{old}}/t_0 \quad \text{and} \quad \mathbf{u}_{\text{new}} = \mathbf{u}_{\text{old}}/(R_0/t_0) \quad .$$

We scale the fluid density and viscosity by that of the interior fluid, so that $\mu_{\text{new}} = \mu_{\text{old}}/\mu_I$ and $\rho_{\text{new}} = \rho_{\text{old}}/\rho_I$. For this problem, density and viscosity depend only on the indicator function, ϕ, which is set to 1 on the interior fluid, and 0 on the exterior fluid. As such, Equations (2.5) and (2.6) simplify to the following:

$$\rho = \phi + (1-\phi)\rho_E/\rho_I = \phi + (1-\phi)\mathcal{D} \tag{4.1}$$

$$\mu = \phi + (1-\phi)\mu_E/\mu_I = \phi + (1-\phi)\mathcal{M} \tag{4.2}$$

where $\mathcal{D} = \rho_E/\rho_I$ and $\mathcal{M} = \mu_E/\mu_I$ are the respective density and viscosity ratios of the exterior to interior fluids. We scale the thickness and surface tension by representative physical values, h_0 and γ_0, so that $h_{\text{new}} = h_{\text{old}}/h_0$ and $\gamma_{\text{new}} = \gamma_{\text{old}}/N_f\gamma_0$. We have scaled the number, N_f, of interfaces per front out of the surface tension to simplify the analysis later. Applying these scales to equation (2.2), and dividing out the dimensional term $\rho_I \rho R_0/t_0^2$, we obtain the following dimensionless form of the momentum equation:

$$\begin{aligned}\frac{\partial \mathbf{u}}{\partial t} + \mathbf{u}\cdot\nabla\mathbf{u} = &-\frac{P_0 t_0^2}{R_0^2\rho_I}\frac{\nabla P}{\rho} + \frac{t_0\mu_I}{R_0^2\rho_I}\frac{1}{\rho}\nabla\cdot\left(\mu(\nabla\mathbf{u} + \nabla\mathbf{u}^T)\right) - \frac{g t_0^2\phi(\rho_I - \rho_E)}{R_0\rho\rho_I}\mathbf{k} \\ &+ \delta_s\left(\frac{\gamma_0 t_0^2}{\rho_I R_0^3}\frac{N_f}{\rho}(\gamma\kappa\mathbf{n} + \nabla_s\gamma) - \frac{t_0^2 h_0 g(\rho_f - \rho_E)}{R_0^2\rho_I\rho}h\mathbf{k}\right)\end{aligned} \tag{4.3}$$

where P_0 is a pressure scale, to be determined later. Thoroddsen and Takehara [55] have shown that inertia and surface tension are the dominant forces in partial coalescence, so we choose a capillary timescale to balance them:

$$t_0 = \sqrt{\frac{\rho_I R_0^3}{N_f\gamma_0}} \quad . \tag{4.4}$$

Substitute this timescale into Eq. (4.3) to obtain

$$\frac{\partial \mathbf{u}}{\partial t} + \mathbf{u}\cdot\nabla\mathbf{u} = -\frac{P_0 R_0}{N_f\gamma_0}\frac{\nabla P}{\rho} + \frac{\mu_I}{\sqrt{R_0\rho_I N_f\gamma_0}}\frac{1}{\rho}\nabla\cdot\left(\mu(\nabla\mathbf{u}+\nabla\mathbf{u}^T)\right) - \frac{R_0^2 g\phi(\rho_I-\rho_E)}{N_f\gamma_0\rho}\mathbf{k} + \frac{\delta_s}{\rho}\left(\gamma\kappa\mathbf{n} + \nabla_s\gamma - \frac{R_0 h_0 g(\rho_f-\rho_E)}{N_f\gamma_0}h\mathbf{k}\right) \quad . \tag{4.5}$$

Now, scale the pressure term using the surface pressure, $P_0 = N_f\gamma_0/R_0$, and introduce three dimensionless groupings:

$$\mathrm{Oh} = \frac{\mu_I}{\sqrt{R_0\rho_I N_f\gamma_0}} \qquad \text{Ohnesorge Number} \tag{4.6}$$

$$\mathrm{Bo} = \frac{R_0^2 g(\rho_I-\rho_E)}{N_f\gamma_0} \qquad \text{Fluid Bond Number} \tag{4.7}$$

$$\mathrm{Bo}_f = \frac{h_0 R_0 g(\rho_f-\rho_E)}{N_f\gamma_0} \qquad \text{Film Bond Number.} \tag{4.8}$$

With the velocity scaled by R_0/t_0, the Ohnesorge number can be seen as an inverse Reynolds number, and measures viscous forces against the dominant forces of inertia and surface tension. The Bond number, Bo, represents the buoyancy force of the interior fluid with respect to the exterior fluid. In the case of a soap film, it will be zero, since the interior and exterior fluid will both be air; while in the case of a liquid drop surrounded by gas, we will have $\mathrm{Bo} > 0$, since the liquid drop will be heavier than the surrounding gas. The film Bond number, Bo_f, is nonstandard, because it involves two different lengthscales: the bubble radius R_0, and the thickness h_0. Although the lengthscale, h_0, is small, the density ρ_f is large in comparison to that of the surrounding gas, and we expect the two to counteract. This Bond number will be nonzero only for soap films, since liquid drops are assumed to have zero thickness.

With these scales, the Navier-Stokes equations take the form

$$\nabla\cdot\mathbf{u} = 0 \tag{4.9}$$

$$\frac{\partial \mathbf{u}}{\partial t} + \mathbf{u}\cdot\nabla\mathbf{u} = -\frac{\nabla P}{\rho} + \frac{\mathrm{Oh}}{\rho}\nabla\cdot\left(\mu(\nabla\mathbf{u}+\nabla\mathbf{u}^T)\right) - \frac{\mathrm{Bo}}{\rho}c(r,z)\mathbf{k} + \frac{1}{\rho}\delta_s\mathbf{F}_s \tag{4.10}$$

where the surface force, $\mathbf{F}_s$, is given by

$$\mathbf{F}_s = \gamma\kappa\mathbf{n} + \nabla_s\gamma - \mathrm{Bo}_f h\mathbf{k} \tag{4.11}$$

The three terms on the righthand side of Eq. (4.11) are depicted in figure 3.1(b). Recall that $\gamma\kappa\mathbf{n}$ accounts for the stress jump across the interface [13], $\nabla_s\gamma$ accounts for tangential stresses due to surface tension gradients [35], and the term $-\mathrm{Bo}_f h\mathbf{k}$ accounts for film buoyancy [36].

The relationship between surface tension and surfactant concentration is given in dimensionless form by Eq. (2.14):

$$\gamma = 1 + \beta(1-\Gamma) \quad .$$

Equation (2.9), for tracking surfactant concentration on the surface, can be expressed in dimensionless form using a Péclet number for the surface:

$$\frac{\partial\Gamma}{\partial t} + \nabla_s\cdot(\Gamma\mathbf{u}) = \frac{1}{\mathrm{Pe}_\Gamma}\nabla_s^2\Gamma \quad \text{where} \quad \mathrm{Pe}_\Gamma = \frac{R_0^2}{k_\Gamma T} \quad . \tag{4.12}$$

The film thickness, h, also satisfies an advection-diffusion equation on the surface [36]:

$$\frac{\partial h}{\partial t} + \nabla_s\cdot(h\mathbf{u}) = \frac{1}{\mathrm{Pe}_h}\nabla_s^2 h \quad \text{where} \quad \mathrm{Pe}_h = \frac{R_0^2}{k_h T} \quad . \tag{4.13}$$

Sensitivity to Neck Width			
w_N	β	Oh_c	Deviation
0.05	0	0.036425 ± 0.000015	$\leq 0.25\%$
0.1	0	0.03647 ± 0.00003	NA
0.2	0	0.03647 ± 0.00003	$\leq 0.16\%$
0.2	1	0.02628 ± 0.00003	$\leq 0.96\%$
0.1	1	0.02609 ± 0.00003	NA
0.05	1	0.02616 ± 0.00003	$\leq 0.50\%$

Table 4.1: Critical Ohnesorge number against neck width, w_N, with and without surfactants ($\beta = 0, 0.1$). The deviations are percent variations measured against the corresponding critical Ohnesorge numbers with $w_N = 0.1$. In all cases, $\mathcal{D} = \mathcal{M} = 1$.

Given our timescale, t_0, the Péclet numbers tend to be quite large [63]. We retain the diffusion terms for numerical stability, but keep surface diffusion negligible: $\mathrm{Pe}_h^{-1}, \mathrm{Pe}_\Gamma^{-1} \ll \mathrm{Oh}$.

We neglect sorption effects for this study, since the timescales of coalescence are small relative to those of sorption. Given the density of air ($1.2\mathrm{kg/m}^3$) and surface tension for soap films ($3 \times 10^{-2}\mathrm{N/m}$), the capillary timescale is bounded above by $t_0 \leq 0.004\mathrm{s}$ for soap bubbles with radii no larger than 2cm. Adsorption and desorption timescales tend to be at least 1s and $10^2\mathrm{s}$, respectively [11].

Finally, we use no-slip and no penetration at the walls, but keep the walls sufficiently far away from the coalescing drop or bubble that they do not influence the coalescence process (see §4.4).

4.4 Application of the Method

Experimental [61] and numerical [59] studies have established that the Ohnesorge number of the interior fluid is a critical parameter for partial coalescence. For fixed density and viscosity ratios, $\mathcal{D}$, and $\mathcal{M}$, of the two fluids, there exists a critical Ohnesorge number, Oh_c, above which coalescence is total, and below which coalescence is partial. This is because the Ohnesorge number measures the relative importance of viscosity in the coalescence process, and thus the dampening of the capillary waves that allow pinch off to take place. We therefore identify the critical Ohnesorge number in various configurations, and compute the percent variation, defined as

$$\delta\mathrm{Oh}_c = \frac{\mathrm{Oh}_c - \overline{\mathrm{Oh}_c}}{\overline{\mathrm{Oh}_c}}$$

where $\overline{\mathrm{Oh}_c}$ is the critical Ohnesorge number associated to some chosen base case.

We initiate our simulations with the drop connected to the reservoir by a narrow neck of width w_N. All of our results were obtained using a width of $w_N = 0.1$. We tested the robustness of this choice against initial widths of $w_N = 0.05, 0.2$, and found that the critical Ohnesorge number, Oh_c, varied by less than 1%, even in the presence of surfactant (see table 4.1).

Our data was obtained within a cylindrical computational domain, with radius $L_r = 5$, height $L_z = 5$, where the drop was centered on the axis, at a height of $z_c = 2.5$. Physical situations of interest may have various boundaries, but most are likely too far away from the coalescence to have an impact. We tested our method for robustness against varying domain sizes: bringing the drop

closer to the floor, closer to the ceiling, and adjusting the radius L_r of the domain. In all cases, the critical Ohnesorge varied by less than 2%. In particular, increasing the vertical and horizontal domain size resulted in variations of Oh_c that were less than 1%, with and without surfactant, and we are therefore confident that we are accurately modeling an infinite domain.

β	L_r	L_z	z_c	$\delta\mathrm{Oh}_c$
0	5	10	5	-0.56%
0.1	5	10	5	-0.69%
0	10	5	3	-0.04%
0.1	10	5	3	-0.02%

Figure 4.2: Variations in critical Ohnesorge number due to pushing the walls further away. The base case, here, is $L_x = L_y = 5$, with $z_c = 2.5$. The resolution is 512 gridlines for every 5 units. Thus, the 5×5 domain has a total resolution of 512^2; the 5×10 domain has a resolution of 512×1024; and the 10×5 domain has a total resolution of 1024×512. Viscosity and density are uniform, and gravity is absent. z_c is the location of the center of the bubble.

We compared the results of our linear elasticity relation to the nonlinear Langmuir equation, given in dimensionless form by Eq. (2.12). Critical Ohnesorge numbers obtained with the linear relation differed from those obtained using the Langmuir equation by no more than 1.25%, so long as surfactant variations satisfied

$$\frac{\widetilde{\Gamma} - \Gamma_0}{\Gamma_\infty - \Gamma_0} \leq 0.25 \tag{4.14}$$

where $\widetilde{\Gamma}$ is the dimensional surface tension and Γ_∞ represents a maximum packing concentration of surfactants on the surface.

β	α_Γ	$\delta\mathrm{Oh}_c$
0.1175	25%	1.25%
0.1469	50%	-15.22%
0.2615	25%	-0.79%
0.3271	50%	-12.54%

Figure 4.3: Percent error in linear model against Langmuir equation (base case) in computed critical Ohnesorge number. The resolution is 512^2; viscosity and density are uniform, and gravity is absent.

In cases where surfactant is absent, critical Ohnesorge numbers of $\mathrm{Oh}_c = 0.026 \pm 0.001$ for the liquid drop ($\mathcal{D} = \mathcal{M} = 0.1$), and $\mathrm{Oh}_c = 0.031 \pm 0.001$ for $\mathcal{D} = \mathcal{M} = 1$ have been presented [59]. We replicated these results with a resolution of $(256/5.0)^2$, but found that the critical Ohnesorge number was more sensitive to resolution than previously thought. By increasing the resolution to $(512/5)^2$, we obtained critical Ohnesorge numbers of $\mathrm{Oh}_c = 0.032 \pm 0.001$ for the liquid drop and $\mathrm{Oh}_c = 0.036 \pm 0.001$ for the case $\mathcal{D} = \mathcal{M} = 1$. We obtained critical Ohnesorge numbers with a resolution of $(1024/5.0)^2$ which differed from the $(512/5.0)^2$ case by less than 1% in the presence of surfactant ($\beta = 0.08$). Without surfactant, the critical Ohnesorge number varied by less than 0.1%.

Lastly, we examined the effects of the drop's initial velocity, U_i, characterized by the Weber number, $\mathrm{We} = \rho_I U_i^2 R_0 / N_f \gamma_0$, on the coalescence outcome. We initialized the velocity of the fluid inside the drop to $-U_i \mathbf{k}$ ($-\mathrm{We}\mathbf{k}$ in non-dimensional form). For relatively small values of We, which are our focus here, no qualitative changes where observed. For a coalescing liquid drop ($\mathcal{D} = \mathcal{M} = 0.1$), we found that the critical Ohnesorge number was smaller than the base case, but only by less

Soap Bubble: $\mathcal{D} = \mathcal{M} = 1$				Liquid Drop: $\mathcal{D} = \mathcal{M} = 0.1$			
Oh	$z_{\mathrm{mch}}(\mathrm{Oh}, \beta)$			Oh	$z_{\mathrm{mch}}(\mathrm{Oh}, \beta)$		
	$\beta = 0$	$\beta = 0.1$	$\beta = 0.2$		$\beta = 0$	$\beta = 0.1$	$\beta = 0.2$
0.01	0.452	0.354	0.370	0.01	0.326	0.269	0.265
0.02	0.333	0.270	0.273	0.02	0.210	0.177	0.166
0.03	0.251	0.208	0.207	0.03	0.135	0.114	0.101

Table 4.2: Maximum crest displacement $z_{\mathrm{mch}}(\mathrm{Oh}, \beta)$, for different β and Oh. Gravity is absent and the initial distribution of surfactant is uniform.

than 4% when the Weber number was 0.1, and by less than 2% when the Weber number was 0.05. This corresponds to a drop with Bo = 0.05 falling a distance of one drop radius. For a soap film ($\mathcal{D} = \mathcal{M} = 1$), the critical Ohnesorge number was greater than the base case by less than 2%, even for a Weber number of 1.0. As such, the remainder of our results should be applicable for small Weber number.

4.5 Results

4.5.1 Surfactant Effects

To isolate the effects of surfactants, measured by the elasticity coefficient, β, we first ignore gravity and assume a uniform initial distribution of surfactant for both the drop and the reservoir. In the absence of gravity, the soap film and the liquid drop are identical, except for the density and viscosity ratios. Figure 4.4 shows a color plot of the pressure for a coalescing system in the presence of surfactant. At first, the qualitative behavior is similar to that of the surfactant-free case - in particular, the capillary waves are still present, and the drop still deforms vertically. However, pinch-off fails to occur, despite the fact that all parameters are the same as in figure 4.1, except for the presence of surfactant (here $\beta = 0.1$). The thickness of the white curve in Fig. 4.4 indicates the surfactant concentration. Early on, surfactant accumulates at the base of the drop, due to area reduction in the initial merging. The surfactant at the crest of the drop first thins out as the crest is stretched upward by capillary waves, but increases later, as the drop contracts toward the reservoir.

The results of figure 4.4 indicate that surfactants inhibit partial coalescence. In general, one would expect this to be the case, as surfactants lower surface tension, which increases the Ohnesorge number. More significantly, by causing surface forces to be unevenly distributed, surfactants alter the regime of partial coalescence. Locally increased levels of surfactant result from area reduction. For instance, the increased surfactant concentration at the base of the drop and decreased concentration at the crest, seen in figure 4.4, lowers surface tension at the base of the drop, and increases it at the crest, thereby reducing the forces driving pinch-off, relative to those driving total merging. Thus, we expect the presence of surfactant to inhibit partial coalescence even for a fixed Ohnesorge number. However, if the Marangoni forces generated are sufficiently large, the physical picture may be altered yet again. In particular, Marangoni forces tend to even out the surfactant distribution, which may negate the effects described above. Large Marangoni forces might also counter the stretching of the drop due to capillary waves, and thus restrict the vertical stretching that causes partial coalescence, leading to a potentially different balance of forces.

The influence of Marangoni forces on the vertical deformation of the drop can be measured by the maximal crest displacement of the coalescing drop or bubble. Table 4.2 shows the maximum

vertical displacement of the crest against β for selected Ohnesorge numbers. Notice that although there is a decrease in maximum crest displacement with β early on, the influence of β is much weaker than that of the Ohnesorge number, and in the case of the liquid drop, it is actually non-monotonic. As such, the effects of the Marangoni forces in inhibiting drop stretching do not have a significant influence on the coalescence dynamics for the range $0 \leq \beta \leq 0.2$ of elasticity coefficient.

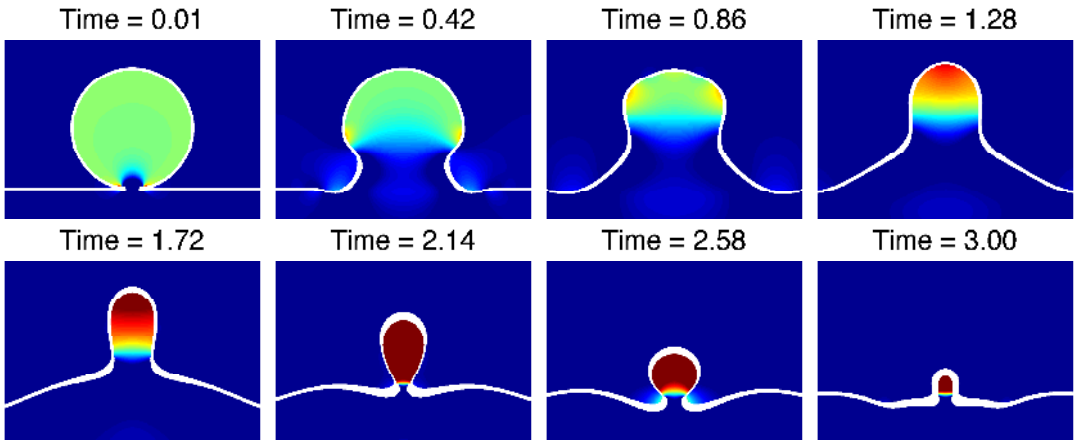

Figure 4.4: Pressure plots showing a time sequence of partial coalescence of a surfactant covered drop or bubble on a reservoir. The surfactant concentration is shown as a thickness effect. The elasticity coefficient is $\beta = 0.1$, indicating the presence of surfactant. The initial surfactant concentration is everywhere uniform. All other parameters are the same as in figure 4.1: gravity is absent, Oh $=$ 0.027, and $\mathcal{D} = \mathcal{M} = 1$.

Figure 4.5 shows critical Ohnesorge numbers, Oh_c, against β for two cases: equal density and viscosity for interior and exterior fluids ($\mathcal{D} = \mathcal{M} = 1$); and a liquid drop surrounded by a gas, coalescing with a reservoir of identical liquid ($\mathcal{D} = \mathcal{M} = 0.1$). Notice that although the density and viscosity ratios between the fluids affect the level of the critical Ohnesorge number profile, the qualitative behavior of the critical Ohnesorge number is the same for both cases. This is in agreement with previous authors [60,61], who found that density and viscosity differences between the two fluids could be accounted for by employing a modified Ohnesorge number, based on a weighted average of the densities and viscosities.

The elasticity coefficient, β, is seen to have a non-monotonic influence on the critical Ohnesorge number. Initially, there is a sharp decrease in Oh_c, but eventually the trend comes to a stop and reverses itself, resulting in a slow increase of the critical Ohnesorge number. Observations of surfactant concentration time sequences (see figures 4.6 and 4.7) support our hypothesis that the initial decrease in the critical Ohnesorge number results from the uneven distribution of surfactant along the drop profile. In particular, increased surfactant concentrations at the base of the drop, coupled with decreased surfactant concentrations at the crest, result in greater surface tension at the crest than at the base, which inhibits partial coalescence. This result is in agreement with [22], who found that increased fractional surfactant concentration on the neck of a slowly pinching drop inhibits pinch off by weakening the surface forces driving the necking.

We now seek an explanation for the non-monotonic relation between Oh_c and β. Figure 4.6 shows the time evolution of a coalescing drop with $\beta = 0$, next to plots of the surfactant concentration against arc length, measured from the crest. These plots represent the dynamics when Marangoni forces are negligible or absent altogether. As such, the figure shows the behavior of inverse interfacial area, which can be viewed as a concentration of passive, inert molecules on the surface. At the point

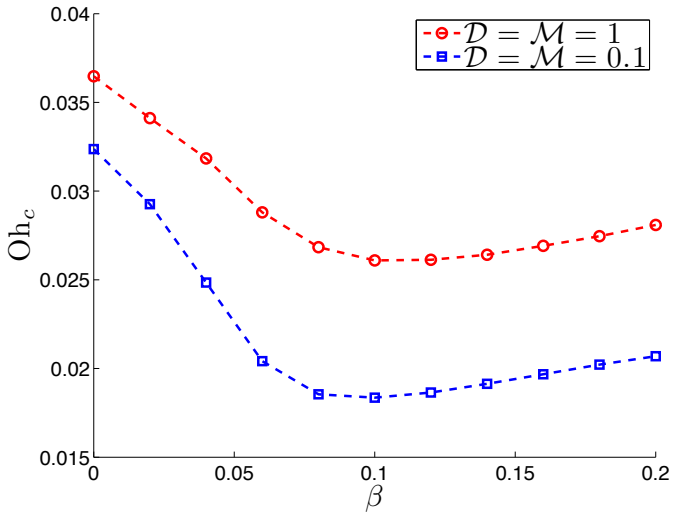

Figure 4.5: Critical Ohnesorge number as a function of the elasticity coefficient β for two cases: uniform density and viscosity, $\mathcal{D} = \mathcal{M} = 1$, representing a soap bubble; and uneven density and viscosity $\mathcal{D} = \mathcal{M} = 0.1$, approximating a liquid drop surrounded by a gas. In both cases, gravity is absent and the initial distribution of surfactant is uniform.

of initial merging (near $s = \pi$), a significant loss of area occurs, resulting in an accumulation of surface molecules in a small area, corresponding to a ring around the base of the merging drop. When the top of the drop contracts, this accumulated surfactant lies near the point of pinch-off. This increased concentration of surfactant lowers the surface forces at the base of the drop driving pinch-off. The eventual decrease in surfactant concentration around the point of pinch-off is a consequence of local area creation, as pinch-off is already underway. Continued contraction of area on the surface of the drop competes against the stretching effects of the capillary waves, resulting in an uneven surfactant distribution along the profile of the drop. Most significantly, the surfactant concentration at the crest of the drop decreases dramatically as the drop stretches under the influence of capillary waves. Eventually, this trend reverses itself, and an even greater increase of the local surfactant concentration is observed as the drop contracts during the final stage of partial coalescence.

From figure 4.7, we see that for larger values of the elasticity coefficient $\beta = 0.1, 0.2$, Marangoni forces reduce the magnitude of variations in surfactant concentrations. Most significantly, surfactant is transported by large Marangoni forces away from the accumulation created by the initial merging. This results in a significant increase in surfactant concentration at the crest of the drop during the merging process, as surfactant at the base of the drop is driven toward the crest by strong tangential flows.

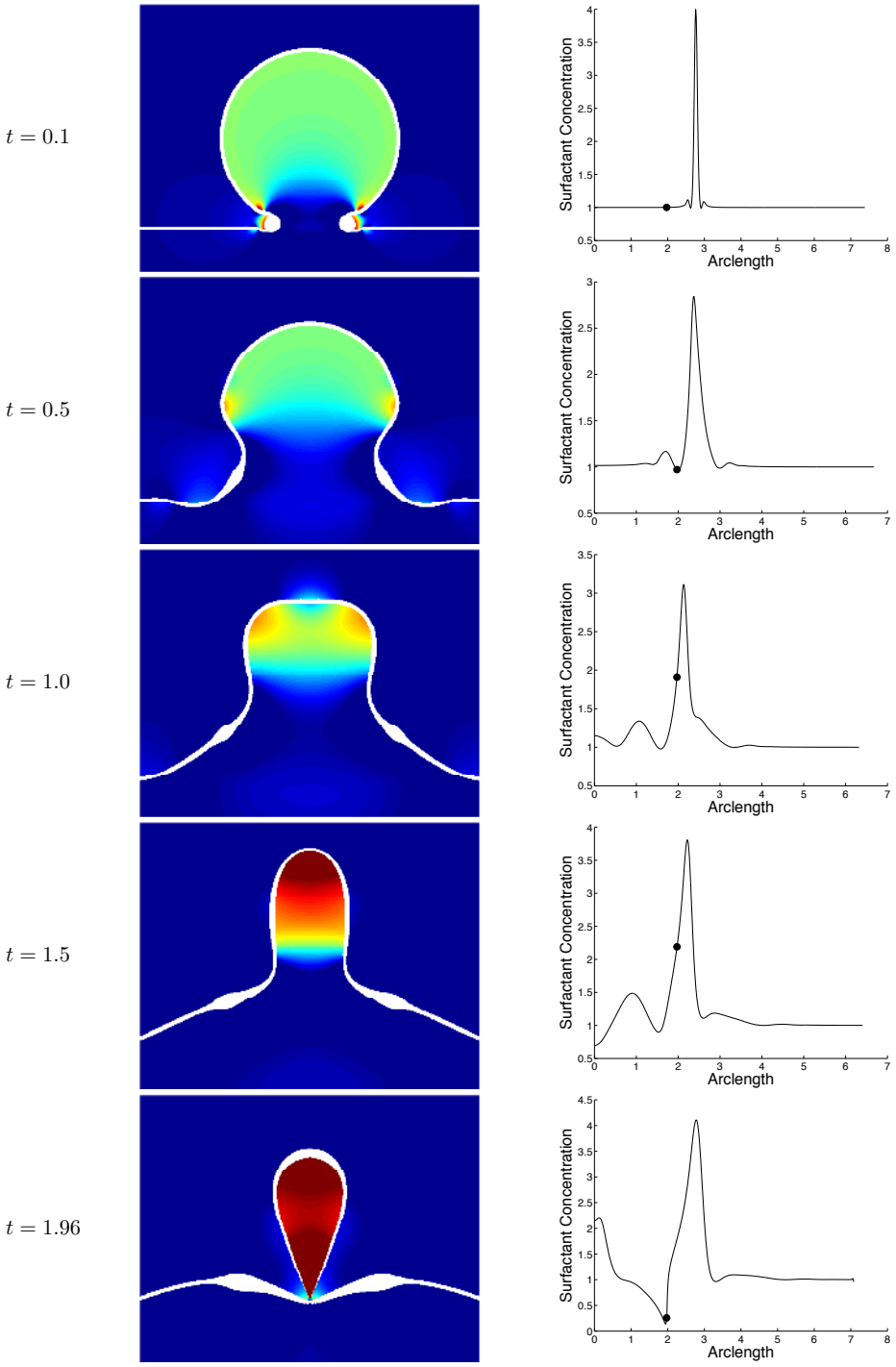

Figure 4.6: Evolution of a drop or bubble covered with inert surface molecules ($\beta = 0$). Left: Pressure color plot of coalescence; the surfactant concentration is shown as a thickness effect. Right: Surfactant concentration against arc length from the crest. The black dots show the location of eventual pinch-off. Here, Oh = 0.02, gravity is absent, and the initial surfactant distribution is uniform.

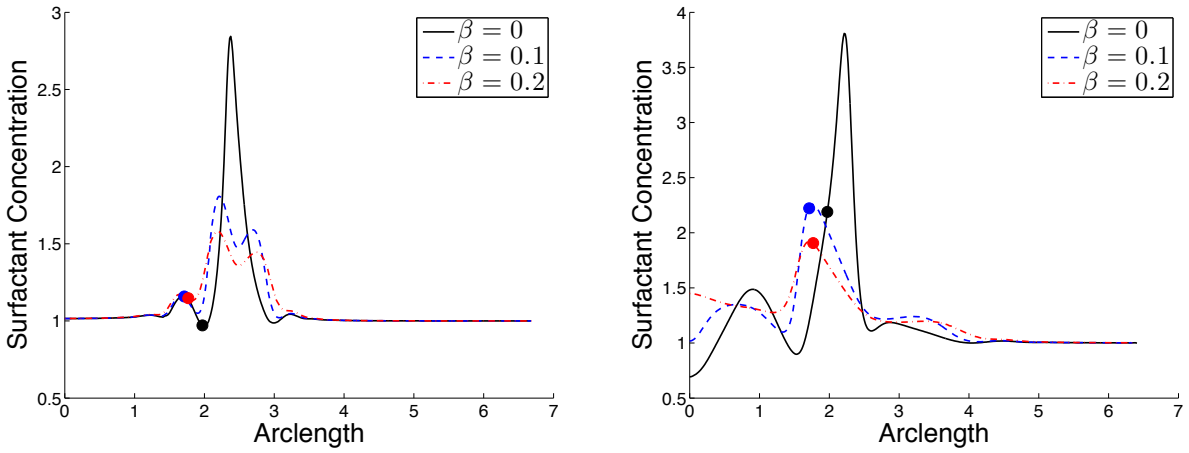

Figure 4.7: Surfactant distribution against arc length, measured from the crest, for Oh = 0.02, and three different values of β, at $t = 0.5$ (left) and $t = 1.5$ (right). The dots show the location of eventual pinch-off. Gravity is absent and the initial surfactant distribution is uniform.

A predicted relation between the critical Ohnesorge number and the surface tension profile can be obtained from a scaling argument. The coalescence dynamics depend on a competition between two surface pressures, at the base and top of the drop, respectively. The surface pressure at the base of the drop is proportional to the local surface tension, γ_b, multiplied by the total curvature, which scales as $1/R_0$. The surface pressure at the top is proportional to the product of a representative surface tension, γ_t and the total curvature at the crest, which scales as $2/R_0$. The pressure at the crest is also opposed by the effect of capillary waves, which rise to the top of the drop. Since the damping rate of the capillary waves is proportional to the Ohnesorge number [59], we can represent the wave pressure as $\gamma_0 f(\mathrm{Oh})/R_0$, where f is a dimensionless function of the Ohnesorge number that measures the wave amplitude, and γ_0/R_0 is the pressure scale of the waves. Thus, coalescence should be partial when

$$\frac{\gamma_b(\beta,t)}{R_0} > \frac{2\gamma_t(\beta,t)}{R_0} - \frac{\gamma_0}{R_0} f(\mathrm{Oh}) \tag{4.15}$$

This gives us an equation for the critical Ohnesorge number:

$$f(\mathrm{Oh}_c) = \frac{2\gamma_t(\beta,t) - \gamma_b(\beta,t)}{\gamma_0} \tag{4.16}$$

Because the critical Ohnesorge number varies by $\leq 30\%$, the wave pressure f can be approximated by a linear function. The constant term can be determined by setting $\beta = 0$, to find $f(\mathrm{Oh}_0) = 1$, where Oh_0 is the critical Ohnesorge number when $\beta = 0$. We thus arrive at a predicted critical Ohnesorge number, $\mathrm{Oh}_{\mathrm{pred}}(\beta,t)$, given by

$$\mathrm{Oh}_{\mathrm{pred}}(\beta,t) = \mathrm{Oh}_0 - aR_\gamma(\beta,t) \quad \text{where} \quad R_\gamma(\beta,t) = \frac{2\gamma_t(\beta,t) - \gamma_b(\beta,t) - \gamma_0}{\gamma_0}. \tag{4.17}$$

Here, $a > 0$ is a scaling factor that we know to be positive because the wave amplitude, measured by $f(\mathrm{Oh})$, decreases with increasing Ohnesorge number. While we do not have a way to precisely predict a, we do obtain a *qualitative* prediction: the shape of $\mathrm{Oh}_{\mathrm{pred}}$, when plotted against β, should resemble that of our computed critical Ohnesorge number profile (see figure 4.5).

To test this prediction, we look for a robust way to measure $R_\gamma(\beta)$. The local surface tensions $\gamma_b = \gamma(s_b,t,\beta)$ and $\gamma_t = \gamma(s_t,t,\beta)$ depend on the locations where they are evaluated, s_b, s_t, and

change with time, t. A natural choice for the local surface tension at the crest of the drop is at $s_t = 0$, and a natural choice for the surface tension at the base of the drop is at the location of eventual pinch-off, in cases where partial coalescence occurs. Given that pinch-off occurs at different locations for different values of β, we choose s_b to be the average of the pinch-off locations for all values of β studied. We have verified that the results obtained depend only weakly on the exact choice of s_b.

The parameter $R_\gamma(\beta; t)$ is not equally determinant in the coalescence outcome for all values of time. For very early times, we do not expect R_γ to be as important, because the dominant process is the initial merging of the drop and the reservoir, and the rapid outward horizontal motion associated to it. After too much time has elapsed, we expect that coalescence outcome is already determined. Thus, there should be a window of time during which the wave pressure plays a more critical role in determining coalescence dynamics. In figure 4.6, the two frames where $t = 1.50$ show a drop which has completed the initial merging process, but is committed to neither partial nor total coalescence - it is around this time when we expect R_γ to play a key role in determining the nature of coalescence. This roughly corresponds to the point in time t_p when the crest of the drop reaches its peak. Sampling values of Oh and β, we found that $1.42 \leq t_p \leq 1.48$ whenever $0 \leq \beta \leq 0.2$ and $0.01 \leq \text{Oh} \leq 0.03$).

Figure 4.8 shows the computed critical Ohnesorge number next to a predicted critical Ohnesorge number, computed using $t = 1.45$. We choose a multiplicative constant of $a \approx 0.072$ to match Oh_c with Oh_{pred}. Although the predictions do not match the computed values exactly, they form a similar shape, exhibiting a non-monotonic dependence on β. We have validated the robustness of this behavior against variations of s_b, the chosen location of the base, on the order of ± 0.1. We have also validated the robustness against time by averaging over the interval $1.3 \leq t \leq 1.6$. Within this range, similar agreement was found.

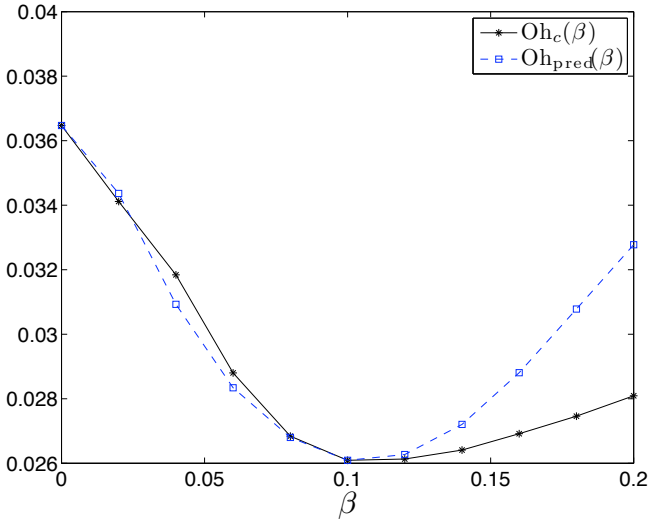

Figure 4.8: Computed critical Ohnesorge number profile against predicted (see Eq. (4.17)). R_γ is computed using $s_t = 0$, s_b approximately the point of pinch-off, $t = 1.45$, and $\text{Oh} = 0.02$. The multiplicative coefficient is $a \approx 0.072$.

The remaining difference between prediction and observation may be due to a variety of factors. The surface pressures at times outside of the interval considered may have a cumulative effect. The influence of β on the wave pressure, though relatively small, is non-zero (see table 4.2). Other factors,

including the Ohnesorge number used to calculate R_γ, also affect the results. However, despite all the simplifications made in our scaling argument, the agreement between predicted and computed Oh_c is still fairly good, indicating that our argument captures the dominant physical mechanism for the non-monotonicity of the critical Ohnesorge number.

As the non-monotonic behavior of the critical Ohnesorge number profile is due to Marangoni effects counteracting the influence of the surfactant, we expect the profile to level off for very large values of β. Additional computations with $\beta = 0.5$ have revealed critical Ohnesorge numbers of 97.3% of the surfactant-free value for bubbles, and 78.4% for liquid drops. Unfortunately, our numerical method becomes unstable for very large values of β, so it is not clear if this trend will eventually level off.

Thus, we conclude that the non-monotonic behavior is a consequence of a competition between variations in surface area, which results in surfactant distributions unfavorable to partial coalescence, and the Marangoni forces, which smooth out this behavior, and nullify the surfactant effects.

4.5.2 Effects of Variations in Initial Surfactant Distribution

In most physical systems, the initial concentration of surfactant on the drop will not equal that on the reservoir. In particular, if the surfactant concentration in the reservoir is higher than on the drop, then the surface tension at the base of the merging drop will be lowered, relative to that at the crest. Thus, greater surfactant concentrations on the reservoir should correspond to lower values of R_γ, which should inhibit partial coalescence, and vice versa.

We denote two equilibrium surface tensions: one for the reservoir, γ_{res}; and one for the drop, γ_{drop}. The uneven initial distribution of surfactant can be described by the normalized difference between the two initial surface tensions.

$$\mathcal{G} = \frac{\gamma_{\mathrm{res}} - \gamma_{\mathrm{drop}}}{\gamma_{\mathrm{drop}}} \tag{4.18}$$

Assuming the surfactant distributions on both the drop and the reservoir are at equilibrium, we use Γ_{drop} as our scaling factor, except in cases where $\Gamma_{\mathrm{drop}} = 0$, which we treat separately. The nondimensional surfactant concentration on the drop is then $\Gamma(t = 0) = 1$; while the initial concentration of surfactant on the reservoir, Γ_{res}, is described by the following relation, obtained from Eq. (2.14).

$$\mathcal{G} = \frac{\gamma_{\mathrm{res}} - \gamma_{\mathrm{drop}}}{\gamma_{\mathrm{drop}}} = \beta(1 - \Gamma_{\mathrm{res}}) \tag{4.19}$$

Assuming the initial surfactant concentration is nonnegative and initial surface tension is positive, we obtain bounds for physically meaningful values of $\mathcal{G}$: $-1 < \mathcal{G} \leq \beta$. Since $\mathcal{G}$ measures the relative surface tension difference between the reservoir and the drop, larger values of $\mathcal{G}$ will correspond to higher surface tension at the base of the drop relative to surface tension at the crest. We define the Ohnesorge number using the surface tension on the drop as a reference $\mathrm{Oh} = \mu_I/\sqrt{R_0 \rho_I N_f \gamma_{\mathrm{drop}}}$. Figure 4.9 shows plots of critical Ohnesorge numbers against β and $\mathcal{G}$. The critical Ohnesorge number increases monotonically with $\mathcal{G}$, as expected. When $\mathcal{G} > 0$, the critical Ohnesorge number as a function of β retains its non-monotonic profile. As $\mathcal{G}$ decreases below zero, the critical Ohnesorge number decreases significantly for small β, and for fixed negative values of $\mathcal{G}$, Oh_c depends linearly on β.

In their 2009 paper, Blanchette, Messio, and Bush [35] studied the effects of surface tension gradients due to differences in chemical composition between the drop and the reservoir. Because

the source of the variable surface tension derived from the chemical properties of the bulk fluid, it was insensitive to local changes in surface area. Thus, the accumulation of surfactant at the base of the drop, which causes the non-monotonic critical Ohnesorge number profile, is absent in their setup. They observed that the critical Ohnesorge number increases monotonically with $\mathcal{G}$, as do we. However, for $\mathcal{G} < 0$, they observed a sheer drop off in the critical Ohnesorge number, so that pinch off doesn't occur at all, when $\mathcal{G} \leq -0.05$. This differs from our observations for surface tension gradients due to surfactants, in which the critical Ohnesorge number gradually decreases as $\mathcal{G}$ decreases, but does not approach zero in the parameter range studied (see figure 4.9).

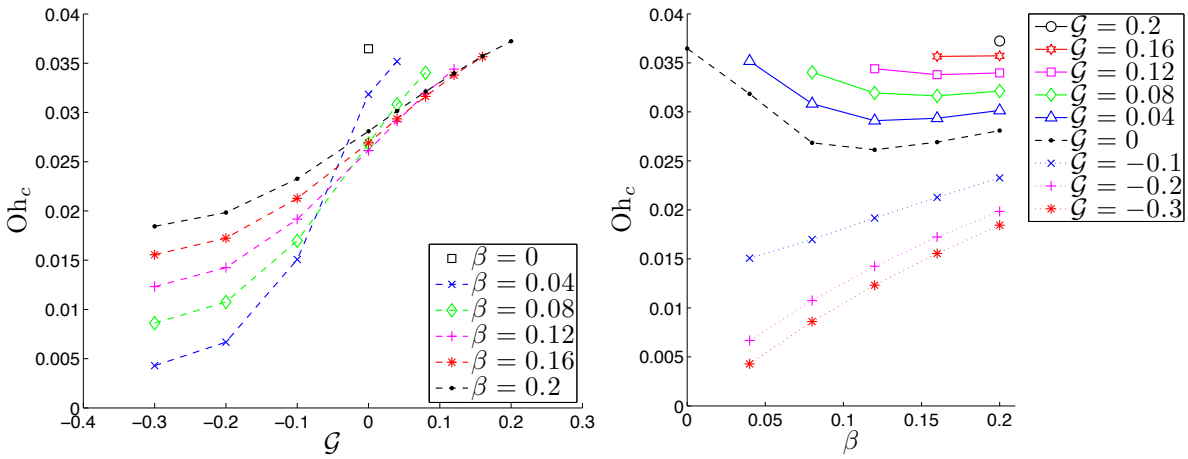

Figure 4.9: Left: critical Ohnesorge number as a function of $\mathcal{G}$ for differing values of β. Right: Critical Ohnesorge number as a function of the elasticity coefficient for various values of the normalized surface tension difference, $\mathcal{G}$. We use $\mathcal{D} = \mathcal{M} = 1$, and gravity is absent in both cases.

The case of the surfactant-free drop is of interest because it is likely to occur when a drop is formed from a bulk fluid which is surfactant-free. Because the drop is surfactant-free, the accumulation of surfactant at the base of the drop will be more limited, due to the fact that surfactant only enters the system from the reservoir, while pinch-off occurs well above the point of initial merging (usually between $0.3\pi R_0$ ad $0.5\pi R_0$). To study the case of the surfactant-free drop, we set $\Gamma_0 = \Gamma_{\text{res}}$, while retaining γ_{drop} as our surface tension scale. Then Eq. (2.14), combined with the assumption $\Gamma_{\text{drop}} = 0$, yields that $\mathcal{G} = -\frac{\beta}{1+\beta}$. In contrast, $\mathcal{G} = \beta$, for the surfactant-free reservoir.

Figure 4.10 shows critical Ohnesorge numbers against β, for a surfactant-free drop and a surfactant-free reservoir. The critical Ohnesorge number profile for equal surfactant concentrations on the drop and the reservoir is shown for reference. Due to our definition of the Ohnesorge number, all three cases are identical when $\beta = 0$, being scaled by the surface tension of a clean, surfactant-free fluid. For $\beta > 0$, the critical Ohnesorge numbers for the surfactant-free reservoir and the case $\mathcal{G} = 0$ are scaled by the surface tension of a contaminated fluid. In the case of the surfactant-free reservoir, this change in scale results in an increase in the surface tension on the reservoir relative to that on the drop, a distribution which favors partial coalescence. As a consequence, the critical Ohnesorge number profile in this case is shifted upward from the base case $\mathcal{G} = 0$.

In the case of the surfactant-free drop, when β is small, the critical Ohnesorge number decreases only slowly with β, because the effects of the surfactant accumulation at the base of the drop have little impact on the merging process. As a consequence, the critical Ohnesorge numbers are higher in this case than when $\mathcal{G} = 0$, where the surfactant accumulation results in a more rapid decrease in critical Ohnesorge number. For $0.14 \leq \beta \leq 0.15$ the critical Ohnesorge number profile

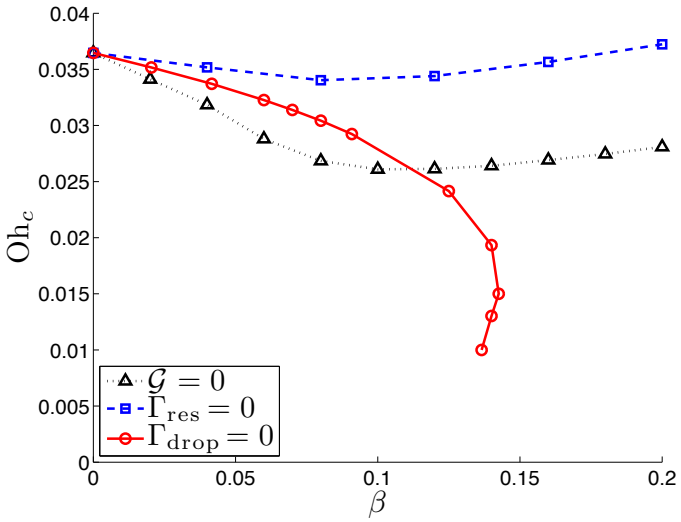

Figure 4.10: The critical Ohnesorge number as a function of the elasticity coefficient, β, for three cases: a surfactant-free drop, ($\mathcal{G} = -\frac{\beta}{1+\beta}$) in red open circles; a surfactant-free reservoir ($\mathcal{G} = \beta$), in blue "+" signs; and equal surfactant for both the drop and the reservoir ($\mathcal{G} = 0$), in black triangles. We scale the Ohnesorge number by the surface tension on the drop, $\gamma_{\rm drop}$, in all cases, and we set $\mathcal{D} = \mathcal{M} = 1$. Gravity is absent.

undergoes a sheer drop, and even a slight inversion, in agreement with [35]. Because the surfactant is concentrated nearly exclusively below the point of pinch off, area reduction effects are minimized, and the configuration closely resembles that of a drop merging with a reservoir of different surface tension arising from differences in chemical composition, rather than surfactant contamination. We observed that for small Ohnesorge numbers and larger values of β, the vertical deformation of the merging drop was quite large, allowing plenty of time for pinch off to occur at the base of the drop. Nevertheless, pinch off failed to occur, as the surface tension at the base of the drop relative to the crest was too weak. We expect that the critical Ohnesorge number goes to zero, and that pinch off does not occur at all when $\beta > 0.15$. However, with large values of β and small Ohnesorge numbers, motion of the surfactant along the surface becomes prohibitively difficult to resolve numerically.

4.5.3 Gravity Effects

In the presence of gravity, soap films and liquid drops must be treated separately. Liquid drops are influenced by buoyancy forces arising from the difference in density between the liquid and the surrounding gas, which is measured by the Bond number, Bo, defined in Eq. (4.7). Soap films are influenced by the buoyancy of the film itself, which is much heavier than the surrounding gas. This effect is measured by a nonstandard Bond number, Bo_f, given in Eq. (4.8).

The influence of gravity takes two forms. First, gravitational forces alter the initial conditions of the coalescence process by deforming the drop and the reservoir, and redistributing the surfactant. Second, gravity influences the system directly, during the coalescence process. We begin by examining the direct effects of gravity, modifying the base case with nonzero Bond numbers $\mathrm{Bo}, \mathrm{Bo}_f$. In this case, we expect gravity to weakly inhibit pinch off, because the pull of gravity adds to the forces driving total coalescence.

We have computed several critical Ohnesorge numbers for the case of the liquid drop and found that the fluid Bond number, Bo, weakly inhibits partial coalescence (see figure 4.11). Specifically, gravity effects decrease the critical Ohnesorge number by a very small amount. This decrease is never more than 2% of the base value, $\mathrm{Oh}_c(\beta = 0, \mathrm{Bo} = 0)$. This is in agreement with [60], who found that gravity weakly inhibits partial coalescence in the absence of surfactant. In the case of a liquid drop, gravity has little effect in the presence of surfactant, as well. This, too, is unsurprising, since gravity does not directly impact the distribution of surfactant on the liquid surface. Indeed, by examining the time evolution of the surfactant distribution against arc length from the crest, we have observed it to be nearly identical with and without gravity, for the duration of the coalescence process.

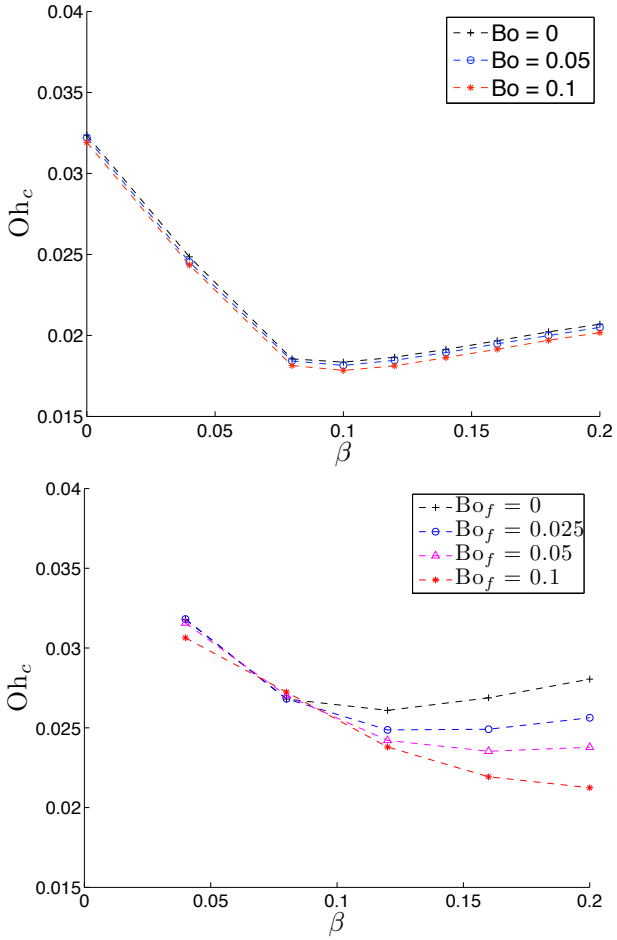

Figure 4.11: Critical Ohnesorge numbers, as functions of β in the presence of gravity for liquid drops $\mathcal{D} = \mathcal{M} = 0.1$ (top), and soap films $\mathcal{D} = \mathcal{M} = 1$ (bottom), with different Bond numbers. The merging process begins with a spherical drop on a horizontal reservoir, with surfactant distributed uniformly and equal for both the drop and the reservoir ($\mathcal{G} = 0$).

Figure 4.11 also shows that gravity has a much larger effect for soap films, one that increases with the elasticity coefficient. In particular, the film Bond number, Bo_f, has a very small effect when β is small, but reduces the critical Ohnesorge number significantly for larger values of β, beginning at about $\beta = 0.1$. The most significant physical difference between the case of the soap bubble and the liquid drop is that gravity acts on the film itself, and thus on the surfactant. As such, we expect

gravity to pull the surfactant downward during the coalescence process, draining surfactant from the bubble and modifying the surface tension locally.

Figure 4.12 shows plots of the surfactant concentration (left) and surface tension (right) on a merging film against the arc length measured from the crest. Each plot contains two curves, one without gravity ($\mathrm{Bo}_f = 0$), and one with gravity ($\mathrm{Bo}_f = 0.05$). In all cases, surfactant drainage due to gravity is evident. The surfactant level is lower on the top and side of the drop, and increased away from the drop, on the reservoir, indicating an accumulation due to gravity. From the plots on the right, we can see that the resulting decrease in surface tension is significantly more pronounced for larger values of β. Notice, in particular, that the difference in surface tension at the crest ($s = 0$) is noticeably larger than the difference near the point of eventual pinch off, for larger values of β. This drainage explains the decrease in critical Ohnesorge number in the presence of gravity.

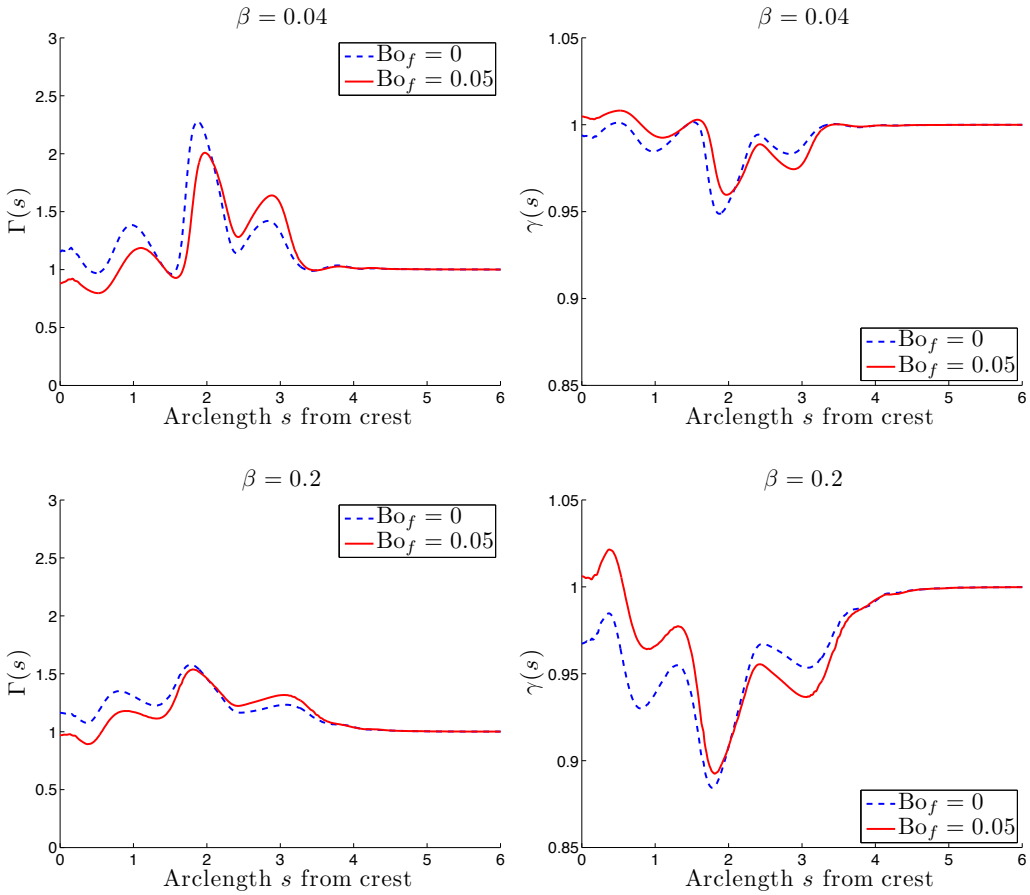

Figure 4.12: Surfactant concentration, $\Gamma(s)$, (left) and surface tension, $\gamma(s)$, (right) against arc length from the crest for a merging soap film, with and without gravity, at $t = 0.98$. In all cases, $\mathrm{Oh} = 0.01$, and the merging process begins with a spherical bubble on a horizontal film, with surfactant distributed uniformly on both the bubble and the film ($\mathcal{G} = 0$).

When a drop sits on a reservoir in the presence of gravity, both the drop and the reservoir deform before the merging process begins. Furthermore, this initial deformation redistributes surfactant. To model these effects, we performed initial computations in which a spherical drop or bubble was

Soap Bubble: $\mathcal{D} = \mathcal{M} = 1$			
Parameter	$\beta = 0.04$	$\beta = 0.12$	$\beta = 0.2$
R_z/R_r	0.9136	0.9031	0.9034
δz	0.2190	0.2376	0.2395
Γ_{top}	0.4615	0.6662	0.7679
Γ_{bot}	0.6928	0.8639	0.9258

Liquid Drop: $\mathcal{D} = \mathcal{M} = 0.1$			
Parameter	$\beta = 0.04$	$\beta = 0.12$	$\beta = 0.2$
R_z/R_r	0.9383	0.9402	0.9408
δz	0.1394	0.1354	0.1339
Γ_{top}	1.0372	1.0038	0.9984
Γ_{bot}	0.5763	0.8380	0.9056

Table 4.3: Parameters measuring maximum deformations due to gravity (see figure 4.13). The systems described are (left) a soap bubble and suspended horizontal film, with $\text{Bo}_f = 0.05$; and (right) a liquid drop and reservoir, with $\text{Bo} = 0.05$.

placed at rest a distance of 0.1 drop radii above a horizontal reservoir, and allowed to deform under the influence of gravity.

We selected a few parameters to measure the state of the system when merging begins, after the system has deformed under the influence of gravity (see figure 4.13). The shape deformation of the drop can be measured by the aspect ratio $R_z(t)/R_r(t)$; where $R_z(t)$ and $R_r(t)$ are the vertical and horizontal radii of the drop. The depression of the reservoir can be measured by the downward displacement, $\delta z(t)$, of the front along the axis during the deformation process. We measure the surfactant redistribution by recording $\Gamma_{\text{top}}(t)$, the surfactant concentration at the top of the drop at time t, and $\Gamma_{\text{bot}}(t)$, the average of the surfactant concentration at the base of the drop and at the center of the reservoir.

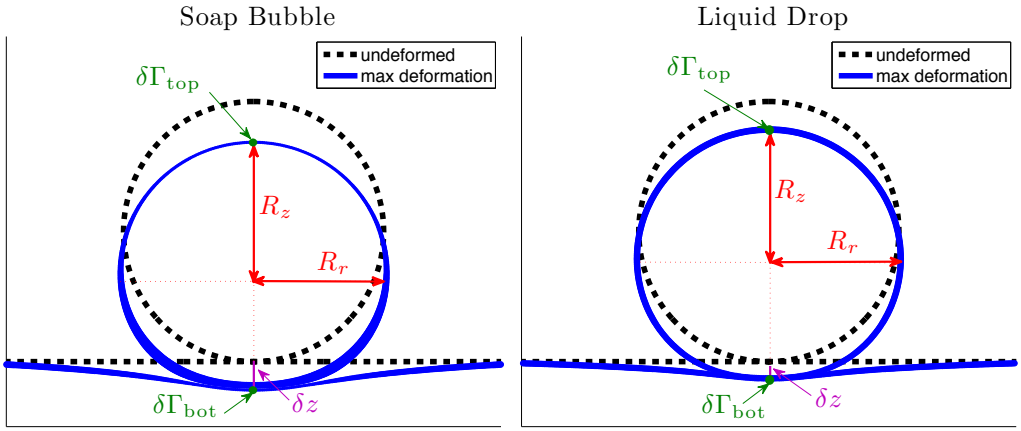

Figure 4.13: A bubble on a film (left) and a drop on a reservoir (right) deformed under the influence of gravity. The surfactant redistribution by gravity is shown as a thickness effect. For the film, $\text{Bo}_f = 0.05$; and for the liquid drop, $\text{Bo} = 0.05$. In both cases $\beta = 0.04$. Measurements of deformation are also shown.

After performing the initial computations until the deformation was maximal, we reset the velocity to zero, connected the deformed drop and reservoir with a narrow neck, of width $w_N = 0.1$, and allowed merging to proceed. Figure 4.13 shows the deformed configurations and deformation parameters for both cases. Their maximal values are given in table 4.3.

Figure 4.15 shows critical Ohnesorge numbers for the soap film and liquid drop against β for six cases. Note that the scale for figure 4.15 is smaller than the scale for figure 4.5, to focus on

the differences between the various cases. Case 1 is the base case, with initial surfactant uniformly distributed, and no interface deformations or gravity - this data is also found in figure 4.5. Case 2 is the undeformed case with gravity. Some of the data associated to case 2 is also found in figure 4.11.

To isolate the deformation effects, we have modified the setup of the base case using data for each effect taken from the initial computation under gravity, and allowing coalescence to proceed without gravity. The deformation effects are shown in table 4.3 and figure 4.13, and include reservoir depression, measured by δz, drop deformation, measured by R_z/R_r, and surfactant redistribution, measured by $\delta\Gamma$. These effects are included in cases (3,4,5), respectively.

In case 3, we used a deformed reservoir, which we joined with a spherical drop and covered with uniformly distributed surfactant. In figure 4.15, we see that the effects of reservoir deformation are negligible for the soap bubble, but significantly inhibit partial coalescence for liquid drops. In this case the liquid drop and the soap bubble differ in only two respects: the ratios $\mathcal{D}, \mathcal{M}$ of density and viscosity, which are unity for the film, and 0.1 for the liquid; and the degree of initial deformation, which is significantly greater for the soap bubble. Additional tests have revealed that the impact of the deformation parameter δz on the critical Ohnesorge number is non-monotonic, indicating that for very large deformations, as with the soap film, the effects on partial coalescence are nullified.

The data in case 4 was obtained by using markers from a deformed drop, as described in table 4.3, line 1, which we connected with an undeformed reservoir and coated with uniformly distributed surfactant. Figure 4.15 reveals that drop deformation favors partial coalescence for both the liquid drop and the soap bubble. This is to be expected, since the deformation of the bubble or drop adds to the surface energy of the system, which will propel the drop upward, delaying total coalescence. The observed effect is significantly smaller for liquid drops, which is consistent with the deformation of the drop being smaller than that of the bubble.

Critical Ohnesorge numbers resulting from surfactant redistribution (case 5), obtained by supplying markers on an undeformed drop and reservoir with redistributed surfactant concentrations, are also shown in figure 4.15. This redistribution tends to favor partial coalescence for the liquid drop and inhibits it for the soap film. This effect can be explained by examining the redistributed surfactant profile, shown in figure 4.14. For both the soap film and the liquid drop, air vacates the channel between the drop and the reservoir, resulting in a decreased surfactant concentration near the base of the merging drop. This explains the increased critical Ohnesorge number associated to the liquid drop. For the soap film, however, this effect is counteracted by the drainage of surfactant from the top of the bubble, toward the base, also visible in figure 4.14. This results in lowered surface tension at the base of the drop during the merging process, and hence a decreased critical Ohnesorge number. These effects, however, are relatively weak, and vanish in the presence of larger Marangoni forces ($\beta = 0.12, 0.2$).

Lastly, all effects are taken into account (case 6), for a physically realistic picture. Figure 4.15 shows that for the soap film, the direct influence of gravity during the coalescence process is dominant, because it inhibits partial coalescence by draining surfactant from the coalescing film. For the liquid drop, partial coalescence is inhibited by the reservoir deformation. In both cases, the drop/bubble deformation favors partial coalescence significantly, by propelling the drop upward during the coalescence process. However, these effects are not additive, and the effect of the drop and bubble deformation doesn't seem to play a significant role in the presence of the other factors.

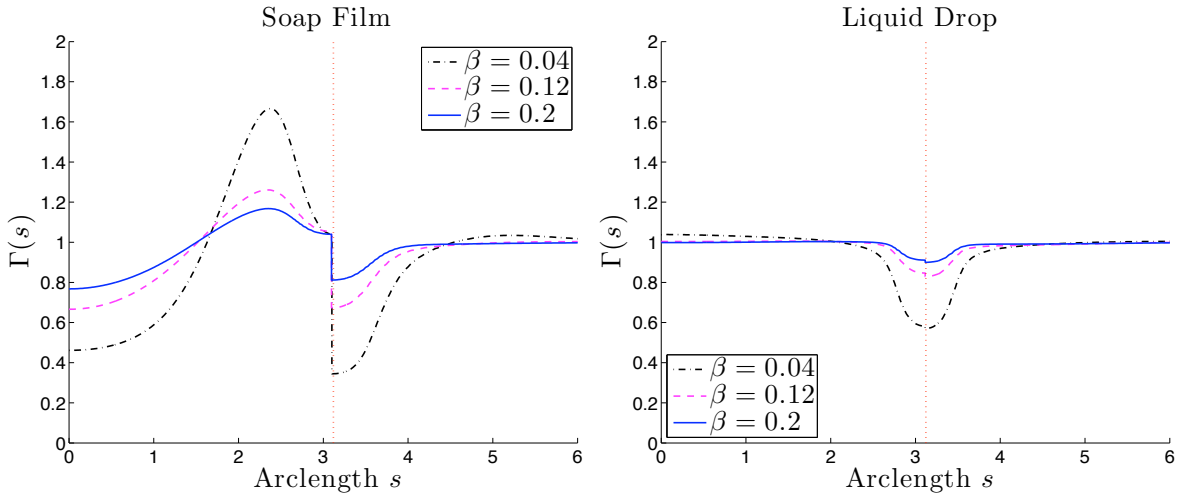

Figure 4.14: Surfactant profile redistributed by gravity at the time of maximum deformation for a soap film (left) and a liquid drop (right) The vertical line shows the point where merging begins - so that the portion of the plot to the left of the vertical line describes the drop, and the portion of the plot to the right describes the reservoir.

4.5.4 Daughter Drops and Coalescence Cascade

When a merging drop pinches off and ejects a daughter drop, the new drop will have a smaller radius, as well as a different surfactant concentration. After initial pinch off, the daughter drop will bounce on the reservoir and eventually coalesce. This leads to a coalescence cascade, observed by Charles and Mason in 1960 [54] and Thoroddsen and Takehara in 2000 [55].

Figure 4.16 shows the dependence of the radius of the daughter drop on the Ohnesorge number and the elasticity coefficient. The radius of the daughter drop decreases monotonically with the Ohnesorge number, while its dependence on the elasticity coefficient has a non-monotonic profile similar to that of the critical Ohnesorge number. The new surfactant concentration, surface tension, and radius of the daughter drop will result in a changed Ohnesorge number, elasticity coefficient, and normalized surfactant difference $\mathcal{G}$ between the reservoir and the drop. We subscript quantities associated to the daughter drop with a D: $R_D, \gamma_D, \Gamma_D, \mathrm{Oh}_D, \beta_D, \mathcal{G}_D$. The new Ohnesorge number is given by

$$\mathrm{Oh}_D = \frac{\mu_I}{\sqrt{\rho_I \gamma_D N_f R_D}} \quad . \tag{4.20}$$

In general, the radius of the daughter drop is bounded as $0.35R_0 \leq R_D \leq 0.6R_0$. If we assume constant surface tension, then the Ohnesorge number will increase with every iteration. From the lefthand plot in figure 4.16, it is clear that this increased Ohnesorge number will further decrease the radius of the daughter drop in the next partial coalescence event.

The surfactant concentration on the daughter drop can be computed based on the surfactant profile at the moment of pinch off. Previous studies [58] have shown that the time it takes for the new merging process to begin is long enough that the surfactant distribution on the drop and reservoir will have reached equilibrium. Because we assume the reservoir to be much larger than the coalescing drop, its surfactant concentration and surface tension will have returned to their original values by the time merging with the daughter drop begins. Having determined that initial surfactant redistribution due to gravity has a negligible effect on partial coalescence, we can assume that the

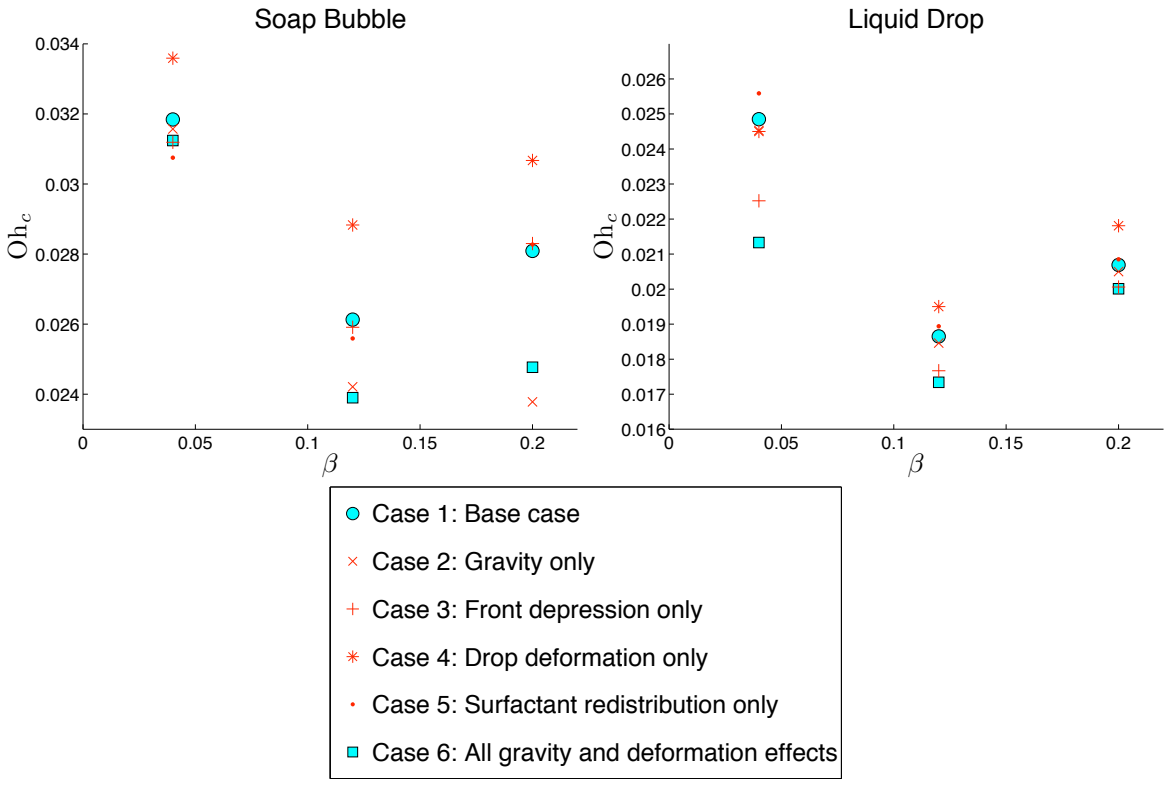

Figure 4.15: Critical Ohnesorge numbers for a soap film, $\mathcal{D} = \mathcal{M} = 1$ (left); and a liquid drop, $\mathcal{D} = \mathcal{M} = 0.1$ (right), against selected values of β, for six cases. The first case is the base case, involving no deformation or gravity effects, and duplicates data from figure 4.5. The second case includes only gravity, without deformation, duplicating some data from figure 4.11. In case 3, only the reservoir is deformed ($\delta z \neq 0$). In case 4, only the drop is deformed ($R_z/R_r \neq 1$). In case 5, only the surfactant is redistributed ($\delta\Gamma \neq 0$). The last case includes all effects. In cases 2 and 6 the Bond number is 0.05 - gravity is absent in the other cases. Note that the scale here is smaller than the scale in figure 4.5.

surfactant concentration and surface tension on the daughter drop will be uniformly distributed when merging begins. Furthermore, the new surfactant concentration and surface tension satisfy the relation

$$\gamma_D/\gamma_0 = 1 - \beta\,(\Gamma_D/\Gamma_0 - 1) \tag{4.21}$$

obtained by applying Eq. (2.14) to the system at the moment of pinch off. Applying Eq. (4.21) to the definitions of the parameters β and $\mathcal{G}$, obtain the following relations:

$$\beta_D + 1 = \frac{\beta + 1}{\gamma_D} \quad , \quad \mathcal{G}_D + 1 = \frac{\mathcal{G} + 1}{\gamma_D} \tag{4.22}$$

Figure 4.17 shows R_D, γ_D, β_D, and $\mathcal{G}_D$ as functions of $\mathcal{G}$ when Oh $= 0.01$, for selected values of β. The values of β_D and $\mathcal{G}_D$ were computed using Equations (4.22). In all cases, R_D displays a positive linear dependence on $\mathcal{G}$, while γ_D displays an inverse dependence, which appears to level off at $\gamma_D \approx \gamma_0$. In nearly all cases, $\gamma_D \leq \gamma_0$, indicating that the daughter drop tends to have a higher surfactant concentration than the parent drop, so equations (4.22) imply that $\mathcal{G}_D$ and

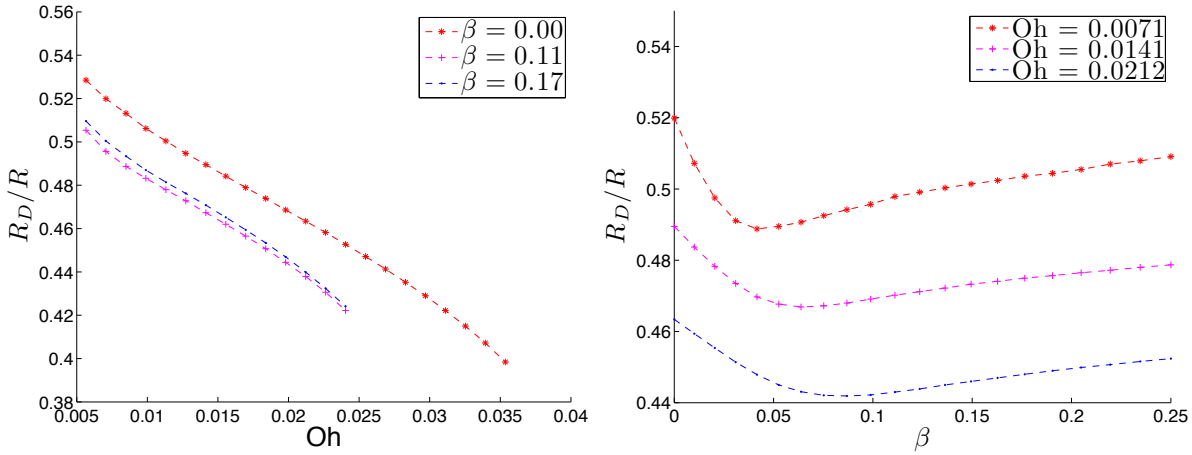

Figure 4.16: Radius of the daughter daughter drop as a function (left) of the Ohnesorge number Oh for three values of the elasticity coefficient, β; and (right) as a function of β for three Ohnesorge numbers. In both plots $\mathcal{D} = \mathcal{M} = 1$, gravity is absent, and the initial surfactant distribution is uniform.

β_D will generally increase in a cascade of partial coalescence events. This can be explained as a consequence of the loss of area which occurs on the drop during the coalescence process. In cases where the surfactant concentration on the reservoir is much greater than that on the daughter drop, the surfactant concentration on the daughter drop will remain essentially unchanged.

If $\mathcal{G} > 0$ initially, the amount of surfactant on the drop will change little during a cascade of partial coalescence events - increasing only slightly. As a consequence, the elasticity coefficient and the surfactant concentration will increase only slowly throughout the cascade. However, if $\mathcal{G}$ is much less than 0 initially, β_D will be very large - on the order of 1, and $\mathcal{G}_D$ will be a large positive. This corresponds to a situation in which the reservoir has large concentrations of surfactant, and the ejected drop has much larger concentrations. In this case, our assumption of low surfactant concentration variations may no longer hold.

By applying Equations (4.20) and (4.22), interpolating on existing data, and using some linear extrapolation for very small Ohnesorge numbers, it is possible to track the properties of the daughter drop or bubble for a coalescence cascade. Table 4.4 shows a hypothetical cascade of 10 coalescence events, beginning with a soap bubble with radius 2cm, $\mathcal{G} = 0$, and $\beta = 0.04$. The final bubble of radius 22μm does not undergo partial coalescence, because the Ohnesorge number is supercritical. The radius of the daughter bubble decreases by a factor of roughly 1/2 each time; while the Ohnesorge number increases by a factor of roughly $\sqrt{2}$. With each event, the daughter bubble becomes more contaminated, resulting in a slow increase in β_D, $\mathcal{G}_D$, and Γ_D, while γ_D decreases. This cascade is significantly longer than the one observed by Thoroddsen *et al.* [55], which involved 5 events. This due to two reasons: the initial radius of the soap bubble is much larger than the maximum radius of a liquid drop; and the critical Ohnesorge number is larger. Having said that, we expect that such a cascade would likely be difficult to obtain experimentally because the film may burst, and because the basic assumption of our model that $h_0 \ll R_0$ breaks down for soap bubbles with radii on the order of 10μm to 100μm [64].

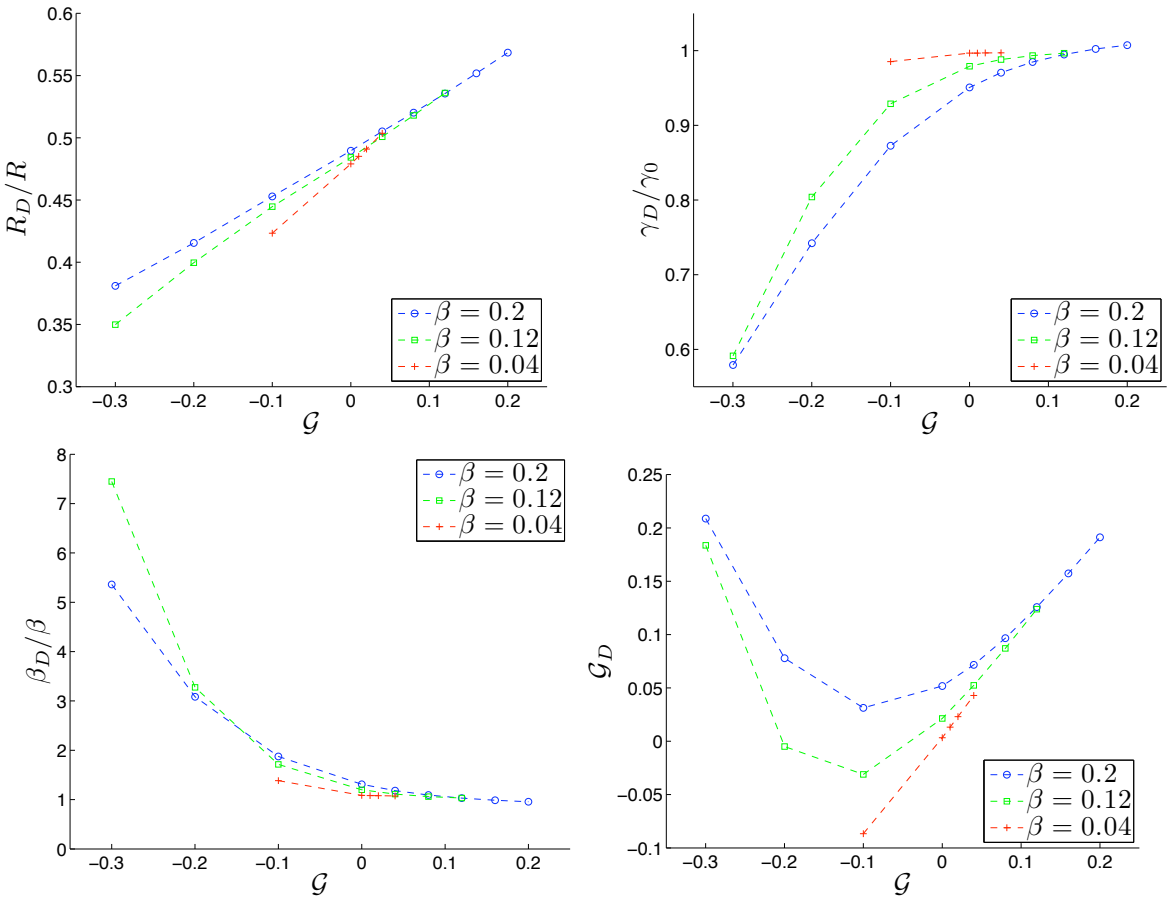

Figure 4.17: Top left: Radius of the daughter drop as a function of $\mathcal{G}$. Top right: Average surface tension on the daughter drop. Bottom Left: Elasticity coefficient of the daughter drop. Bottom Right: Surfactant concentration on the daughter drop. Three cases are shown: $\beta = 0.2$, $\beta = 0.12$, $\beta = 0.04$. In all cases, $\mathrm{Oh} = 0.01$, $\mathcal{D} = \mathcal{M} = 1$, and gravity is absent.

4.6 Conclusion

We have studied surfactant effects in the partial coalescence of drops and bubbles. Our study indicates that the presence of surfactant can lower the critical Ohnesorge number for partial coalescence by more than 30%, but that this effect reverses itself when surfactant concentration or potency is large. Furthermore, by studying different initial conditions, different density and viscosity ratios, as well as gravity effects and daughter drops, we have obtained a more complete description of the partial coalescence regime.

Because surfactant is present in most natural settings where partial coalescence occurs, our findings can be applied to better understand partial coalescence in nature. Furthermore, they can be applied to experimental work on partial coalescence where surfactants are present as impurities and are difficult to remove. Our results demonstrate, in agreement with previous experimental observations, that partial coalescence is limited to a more narrow regime in the presence of surfactants. Even more significantly, a clean drop merging with a surfactant-laden interface will always coalesce com-

Soap Bubble Coalescence Cascade: $\mathcal{D} = \mathcal{M} = 1$						
N	R_D	Oh_D	β_D	$\mathcal{G}_D$	Γ_D/Γ_0	γ_D/γ_0
0	2cm	7.3×10^{-4}	0.040	0	1	1
1	1cm	1.0×10^{-3}	0.044	0.0033	1.0828	0.9967
2	5.2mm	1.5×10^{-3}	0.047	0.0070	1.1748	0.9930
3	2.6mm	2.0×10^{-3}	0.052	0.0112	1.2768	0.9889
4	1.3mm	2.9×10^{-3}	0.057	0.0158	1.3896	0.9844
5	0.69mm	4.0×10^{-3}	0.062	0.0210	1.5134	0.9795
6	0.35mm	5.6×10^{-3}	0.068	0.0266	1.6479	0.9741
7	0.18mm	7.9×10^{-3}	0.074	0.0327	1.7920	0.9683
8	91μm	0.011	0.081	0.0392	1.9436	0.9623
9	45μm	0.016	0.088	0.0460	2.0994	0.9560
10	22μm	0.023	0.093	0.0507	2.2056	0.9518

Table 4.4: A theoretical cascade of coalescence events for a soap film, based on the data in figure 4.17. The index N represents the number of partial coalescence events which have already occurred. Gravity is neglected, as $\mathrm{Bo}_f \leq 0.06$ in all cases.

pletely if the surfactant effects on the reservoir are sufficiently strong. In addition, because drops undergoing partial coalescence with contaminated reservoirs produce daughter drops which have generally higher surfactant concentrations, our findings suggest a possible means of incrementally increasing surfactant concentration on small drops.

We have simulated, for the first time, the partial coalescence of soap bubbles - an effect which is readily observed experimentally, and which offers advantages over drops for laboratory study, due to the relatively large length and time scales involved. In fact, partial coalescence of soap bubbles may be easily realized in science demonstrations and students may reproduce it themselves. Our results indicate that partial coalesce of soap bubbles is a robust phenomena provided the surfactant concentration of the bubble and of the film is similar.

Chapter 5

Rising Drops

5.1 Introduction to Rising Drops

In the past century, a considerable amount of work has been done studying the motion of drops, bubbles and solid spheres rising or settling in stratified and uniform ambients (see below). Solid objects are usually assumed to be settling under the influence of buoyancy, while bubbles are generally assumed to be rising. Drops are sometimes modeled as rising, and sometimes as settling. We assume the drops are lighter than the surrounding fluid, and thus focus on rising drops. However, the two cases, rising and settling, are symmetric, and any observations of rising drops apply in a symmetric fashion to settling drops.

In the inertia free case, the speed of buoyancy driven solid spheres [2], and clean drops and bubbles [3,4] is known theoretically. In addition to inertia, complicating factors include temperature stratification, density stratification, chemical gradients in the ambient that can cause surface tension changes, and the presence of surfactants.

In 1947, Frumkin and Levich [65] (see also [66,67]) provided the theoretical framework for understanding surfactant effects on drop speed. When a surfactant-laden drop rises in a uniform ambient, the surfactant is convected toward the rear of the drop, where it accumulates. As a consequence, surface tension decreases as one travels from the top of the drop to the bottom. The resulting Marangoni stresses oppose the motion of the drop, thus decreasing the speed of the rising drop. Their work was subsequently confirmed by experimentalists, who observed velocity retardation for contaminated drops and bubbles [68–70]. In particular, Horton, et al [70] observed field lines in rising drops using tracers, and found that the flow detached from the drop surface toward the bottom of the drop, indicating stagnation there. Once a drop becomes sufficiently contaminated, the entire surface becomes stagnant, and the drop behaves like a solid particle. In this regime, called uniform retardation, the speed of the moving drop will remain constant when the contamination is increased.

Later, more detailed experimental studies have examined the steady-state speed of moving drops against the degree of surfactant contamination [71], drop shape [72], and desorption rate [73]. In some cases, the speed of rising gas bubbles was observed to be independent of the bulk surfactant concentration over a broad range of contamination [74].

Numerous studies have calculated the steady-state velocity of a buoyancy driven drop or bubble in the presence of surfactants. Broadly speaking, these studies have focused on two regimes. In the first regime, surface convection is much faster than sorption and bulk diffusion, so that the surfactant may be treated as insoluble. In the second case, sorption and bulk diffusion are of the same order as convection. In the insoluble limit, when surface diffusion is negligible, there exists a region on the trailing end of the drop, called a stagnant cap, over which the surface is rendered immobile [75–77]. In this limit, for the case of Stokes' flow, an exact, closed form solution has been obtained for the linear [9] and nonlinear [78] surfactant relation.

A number of asymptotic and numerical studies have tracked the velocity of buoyancy driven drops and bubbles in the limit of low Reynolds number. Several authors [79–81] have accounted for sorption from the bulk using boundary layer analysis valid for low bulk diffusion. Holbrook and Levan published a two part study of the steady-state velocity of a buoyancy driven drop in a surfactant bath, treating the stagnant cap limit and the limit of uniform retardation asymptotically [7] and treating the intermediate regime numerically [8]. This was generalized to the full Frumkin surfactant relation by Chen and Stebe [12]. Wang, et al [82] studied the effects of the bulk Péclet number on surfactant distribution for a variety of bulk concentrations. More recent studies have examined the effects of a finite Reynolds number with [83–85] and without [86,87] deformation, and described the wake that forms behind the drop.

Nearly all studies of surfactant effects on moving drops and bubbles have focused on steady-state motion in a uniform ambient, although a few [88,89] have examined transient motion in a uniform ambient. Studies of motion in a stratified ambient have generally involved either clean drops and bubbles or solid, spherical balls. Extensive work [90–95] has been done studying the passage of drops and solid spheres passing through a layer between two immiscible fluids. In 1999, the first study [96] of drops passing through a density stratification observed increased drag due to fluid entrainment. In sufficiently sharp stratifications, falling drops were observed to reverse direction, temporarily levitating before passing into the lower layer [97]. In the Stokes limit, the velocity of a drop passing through a sharp stratification has been described theoretically [98,99]. For weakly stratified media, such as are found in nature, entrainment effects on the drag have been carefully quantified for solid spheres [100] and drops [101]. In this setup, drop deformation, oscillation, and the flow field have also been examined [101]. The transient motion of solid spheres settling in a linear stratification has also been studied [102]. Another substantial body of research concerns the plumes generated by bodies passing through a stratification (see for example, [103–105]). Research has also been done concerning the oscillations of neutrally buoyant bodies [106,107].

Recent studies have begun to examine interactions between pairs [108] and swarms [109,110] of particles settling in stratifications. Other recent studies [111,112] have examined porous bodies settling in stratification, due to their value in modeling marine snow. One recent study [113] accounted for Marangoni effects due to differences in chemical composition between two layers of miscible fluid. However, to the best of our knowledge, no studies have examined surfactant effects on drops rising in stratified media.

In the 2010 Deepwater Horizon oil spill, millions of gallons of crude oil leaked from the ocean floor and rose to the surface. In an effort to break down the oil, dispersants, including surfactants, were sprayed on the affected areas. A good understanding of the dynamics of oil drops rising in the ocean should account for surfactant effects and density changes (pycnoclines) in the ocean.

Here, we present a numerical study of surfactant effects on the speed and entrainment of rising drops, as applicable to oil drops in the ocean. We examine a regime in which inertia is non-negligible, but the drop remains approximately spherical. The surfactant is insoluble in some cases and soluble in others. We generally keep diffusion as small as possible. In §5.2 we present the setup of our

simulations and equations governing the system. Thereafter, we present our results for three setups: a surfactant-laden drop rising in an unstratified ambient (§5.3), a surfactant-laden drop rising in a linear density stratification (§5.4), and a clean drop entering a layer of dissolved surfactant (§5.5).

5.2 Setup and Governing Equations

The system we consider is axially symmetric. A surfactant-laden drop is rising under the influence of buoyancy in a cylindrical container. We apply no-slip and no-penetration at the boundaries, but keep the walls far away enough not to influence the dynamics of the rising drop. The surface of the drop moves with the fluid,

$$\frac{d\mathbf{x}_s}{dt} = \mathbf{u}\Big|_s \quad . \tag{5.1}$$

We write the equations of fluid motion in dimensionless form, using the drop radius, R_0, as a length-scale. For a velocity scale, we choose the Hadamard-Rabzynski speed [3,4] of a clean drop or bubble rising in creeping flow, assuming for simplicity that the drop and the ambient have the same viscosity, μ:

$$U_{\mathrm{HR}} = \frac{4g(\rho_a - \rho_d)R_0^2}{15\mu} \quad . \tag{5.2}$$

Here, ρ_d is the density of the drop and ρ_a is the density of the ambient fluid.

Both the drop and the ambient obey the incompressible Navier-Stokes, given below in dimensionless form:

$$\nabla \cdot \mathbf{u} = 0 \tag{5.3}$$

$$\rho\frac{\partial \mathbf{u}}{\partial t} + \rho\mathbf{u}\cdot\nabla\mathbf{u} = -\nabla P + \mathrm{Re}^{-1}\nabla^2\mathbf{u} + \frac{15}{4\mathrm{Re}}\Delta\rho\mathbf{k} + \mathrm{We}^{-1}\delta_s(\gamma\kappa\mathbf{n} + \nabla_s\gamma) \quad . \tag{5.4}$$

The delta function in Eq. (5.4) is nonzero only on the interface. Two dimensionless groupings appear in Eq. (5.4), measuring viscosity and surface tension against the inertia of the falling drop:

$$\mathrm{Re} = \frac{\rho_d R_0 U_{\mathrm{HR}}}{\mu} \qquad \text{Reynolds number} \tag{5.5}$$

$$\mathrm{We} = \frac{\rho_d R_0 U_{\mathrm{HR}}^2}{\gamma_0} \qquad \text{Weber number} \quad . \tag{5.6}$$

In this context, the Weber number allows for shape deformation of the drop, and is kept small (see table 5.1) so that the drop remains approximately spherical. In our simulations, the drop aspect ratio varied by less than 2% of the drop radius. The gravity term depends on a normalized density difference:

$$\Delta\rho = \frac{\rho_a - \rho_d\rho}{\rho_a - \rho_d} = \frac{\mathcal{D} - \rho}{\mathcal{D} - 1} \quad \text{where} \quad \mathcal{D} = \frac{\rho_a}{\rho_d} \tag{5.7}$$

and ρ is the fluid density.

We consider three distinct physical setups (see figure 5.1). In the first, a drop coated with insoluble surfactant rises in a uniform ambient. In the second, a drop coated with insoluble surfactant enters a density stratification that varies linearly as a function of vertical displacement, z. Finally, we consider a clean drop rising into a fluid layer containing dissolved surfactant. In the first and third setups, the density of the ambient fluid is fixed at ρ_a. In the second setup, the density obeys an advection-diffusion equation which we write in dimensionless form using a Péclet number:

$$\frac{\partial\rho}{\partial t} + \mathbf{u}\cdot\nabla\rho = \mathrm{Pe}^{-1}\nabla^2\rho \quad \text{where} \quad \mathrm{Pe} = \frac{U_{\mathrm{HR}}R_0}{k_\rho} \quad . \tag{5.8}$$

In the above Péclet number, k_ρ is a density diffusion coefficient.

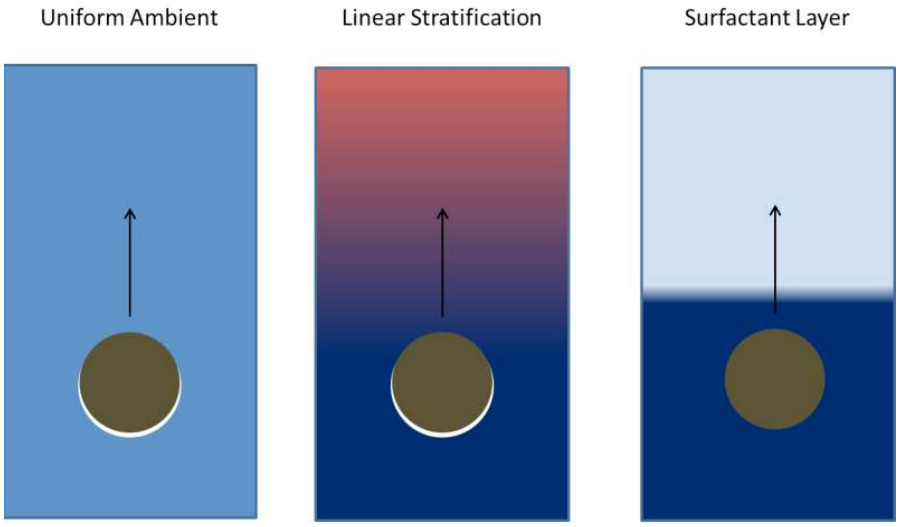

Figure 5.1: The three setups we consider: a surfactant-laden drop rising in a stratified ambient (left), a surfactant-laden drop rising in a linear stratification (center), and a clean drop rising into a layer of dissolved surfactant (right).

As in chapter 4, the advection-diffusion equations that govern the surface (Γ) and bulk (Λ) surfactant concentrations can be nondimensionalized using Péclet numbers, except that here, we account for sorption:

$$\frac{\partial \Gamma}{\partial t} + \nabla_s \cdot (\Gamma \mathbf{u}) = \nabla_s \cdot \left(\frac{1}{\mathrm{Pe}_\Gamma} \nabla_s \Gamma \right) + J(\Gamma, \Lambda|_s) \quad \text{where} \quad \mathrm{Pe}_\Gamma = \frac{U_{\mathrm{HR}} R_0}{k_\Gamma} \tag{5.9}$$

and

$$\frac{\partial \Lambda}{\partial t} + \mathbf{u} \cdot \nabla \Lambda = \nabla \cdot \left(\frac{1}{\mathrm{Pe}_\Lambda} \nabla \Lambda \right) - \delta_s J(\Gamma, \Lambda|_s) \quad \text{where} \quad \mathrm{Pe}_\Lambda = \frac{U_{\mathrm{HR}} R_0}{k_\Lambda} \quad . \tag{5.10}$$

Recall that k_Γ and k_Λ are surface and bulk diffusion coefficients, respectively, and $\Lambda|_s$ is the bulk concentration evaluated on the drop surface. In Eq. (5.10), the bulk surfactant concentration is scaled by its equilibrium value, Λ_0, far away from the drop. The surfactant exchange term can be written in dimensionless form as follows:

$$J(\Gamma, \Lambda|_s) = \mathrm{Bi} \left(\Lambda|_s \left(1 + \mathrm{Ad} - \mathrm{Ad}\Gamma \right) - \Gamma \right) \quad . \tag{5.11}$$

In equation (5.11), two dimensionless groupings appear. The Biot Number is given by

$$\mathrm{Bi} = \frac{R_0 k_{\mathrm{de}}}{U_{\mathrm{HR}}} \tag{5.12}$$

and the adsorption number is given by

$$\mathrm{Ad} = \frac{k_{\mathrm{ad}} \Lambda_0}{k_{\mathrm{de}} \Gamma_\infty} \quad . \tag{5.13}$$

The Biot number measures the desorption rate against the process speed, defined by U_{HR}/R_0, and the Adsorption number measures the rate of adsorptive to desorptive processes. Because Ad is proportional to the equilibrium bulk concentration, it can be thought of as a dimensionless bulk concentration.

In deriving equation (5.11) from equation (2.10), we applied the Langmuir isotherm, which relates the maximum packing concentration to the equilibrium surface concentration

$$\frac{\Gamma_0}{\Gamma_\infty} = \frac{\mathrm{Ad}}{1+\mathrm{Ad}} \quad . \tag{5.14}$$

We also use the linear elasticity relation (2.14):

$$\gamma = 1 + \beta(1-\Gamma) \quad .$$

So far, we have introduced several dimensionless numbers, and we will be encountering more once we examine specific setups. For convenience, they are summarized in table 5.1, along with their definitions and ranges used for each setup we consider.

Parameter	Definition	Range		
		§5.3	§5.4	§5.5
Re	$U_{\mathrm{HR}} R_0 \rho_d / \mu$	$1, 10$	$1, 20$	$1, 20$
We	$U_{\mathrm{HR}}^2 R_0 \rho_d / \gamma$	0.05-0.2	0.05-0.2	0.05-0.2
β	$-\partial\gamma/\partial\Gamma$	0-0.2	0.01-0.2	0.01-0.2
Mg	$\gamma\beta/\mu U_{\mathrm{HR}}$	0-2	$0, 2$	2
$\mathcal{D}$	ρ_a/ρ_d	1.1	1.1	1.1
Pe	$U_{\mathrm{HR}} R_0 / k_\rho$		10^4	
Pe_Λ	$U_{\mathrm{HR}} R_0 / k_\rho$			10^4
Pe_Γ	$U_{\mathrm{HR}} R_0 / k_\Gamma$	$10, 100$	100	100
S	$-(R_0/\rho_d)\partial\widetilde{\rho}/\partial\widetilde{z}$	0	5×10^{-4}-5×10^{-3}	0
Ad	$k_{\mathrm{ad}}\Lambda_0 / k_{\mathrm{de}}\Gamma_\infty$	0	0	$0.1, 1$
Bi	$R_0 k_{\mathrm{de}} / U_{\mathrm{HR}}$	0	0	0.05-10

Table 5.1: Definition and range of parameters in our simulations.

5.3 A Drop Rising in an Unstratified Ambient

We begin by studying a drop covered with an insoluble surfactant moving a uniform medium. We have conducted simulations for Reynolds numbers of $\mathrm{Re} = 1, 10$ and surface Péclet numbers of $\mathrm{Pe}_\Gamma = 10, 100$ and compared our results to an existing theoretical solution.

In the absence of sorption, and when $\mathrm{Pe}_\Gamma \gg 1$, equation (5.9) implies $\Gamma \mathbf{u}_s = \mathbf{0}$ for a steadily rising drop [75]. Thus, only two regions are possible on the drop surface: a clean surface with a free-slip condition ($\Gamma = 0$), and a stagnant surface with a no-slip condition ($\mathbf{u}_s = \mathbf{0}$). Physically, surfactant is convected to the back of the drop where it forms a stagnant cap. The transition from a clean drop to the spherical cap takes place at some fixed angle, θ_c, traditionally measured from the bottom axis (see figure 5.2).

A simple scaling argument shows that the surfactant effects can be measured by the Marangoni number: $\mathrm{Mg} = \gamma_0\beta/\mu U_{\mathrm{HR}}$. On the surface of the drop, viscous stresses drive the surfactant toward the base of the drop, and are opposed by viscous stresses which seek to bring the surfactant into equilibrium. Balancing the two yields

$$\frac{\text{Marangoni stress}}{\text{viscous stress}} \sim \frac{\Delta\gamma/R_0}{\mu U_{\mathrm{HR}}/R_0} \sim \frac{\gamma_0\beta}{\mu U_{\mathrm{HR}}} = \mathrm{Mg} \quad .$$

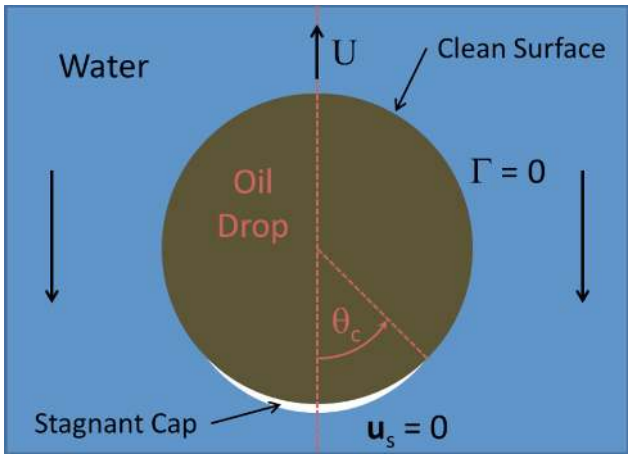

Figure 5.2: A surfactant-laden drop rising in a uniform ambient, with negligible surface diffusion. The surfactant appears in white as a cap on the bottom of the drop, which transitions to a clean surface at a cap angle, θ_c.

The Marangoni number appears in the dimensionless representation of the tangential stress condition at the interface:

$$\mathbf{n} \cdot [\nabla \mathbf{u} + \nabla \mathbf{u}^T] \cdot \mathbf{t} = -\mathrm{Mg} \frac{\partial \Gamma}{\partial s} \quad . \tag{5.15}$$

Here, the brackets represent a jump across the interface. When $\mathrm{Mg} \ll 1$, we expect Marangoni effects to be negligible, so that the drop behaves like a clean drop. When $\mathrm{Mg} \gg 1$, we expect Marangoni effects to dominate viscous effects, forcing the surface velocity of the fluid to zero, so that the drop behaves like a solid sphere. All together, we expect that the system will transition from that of a clean drop to that of a solid sphere as the Marangoni number increases.

Sadhal and Johnson [9] obtained exact solutions for the flow field, the surfactant distribution, and the drag coefficient as functions of the cap angle. Using conservation of surfactant mass, we've derived[1] a relationship between the cap angle and the Marangoni number:

$$\mathrm{Mg} = \frac{2\theta_c - 4\theta_c \cos\theta_c - \sin 2\theta_c + 4\sin\theta_c}{4\pi C_D(\theta_c)} \tag{5.16}$$

where

$$C_D(\theta_c) = 1 + \frac{\mu_a}{2\pi(2\mu_a + 3\mu_d)} \left(2\theta_c + \sin\theta_c - \sin 2\theta_c - \frac{1}{3}\sin 3\theta_c \right) \tag{5.17}$$

is a drag coefficient that depends on the respective dynamic viscosities μ_a and μ_d of the ambient and drop. Equation (5.16) can be inverted numerically to obtain the surfactant distribution and steady-state speed as functions of the Marangoni number.

Figure 5.3 shows the computed and theoretical surfactant distributions of a steadily rising drop plotted against the angle measured from the bottom of the drop. As expected, surface diffusion (inverse Péclet number) smooths out the surfactant distribution. Otherwise, the agreement between the theoretical and computational surfactant profiles is excellent.

Figure 5.4 shows theoretical and computational steady-state speeds of a drop rising in an unstratified ambient, measured as departures from the surfactant free case ($\mathrm{Mg} = 0$). They are plotted

[1] See Appendix A.2

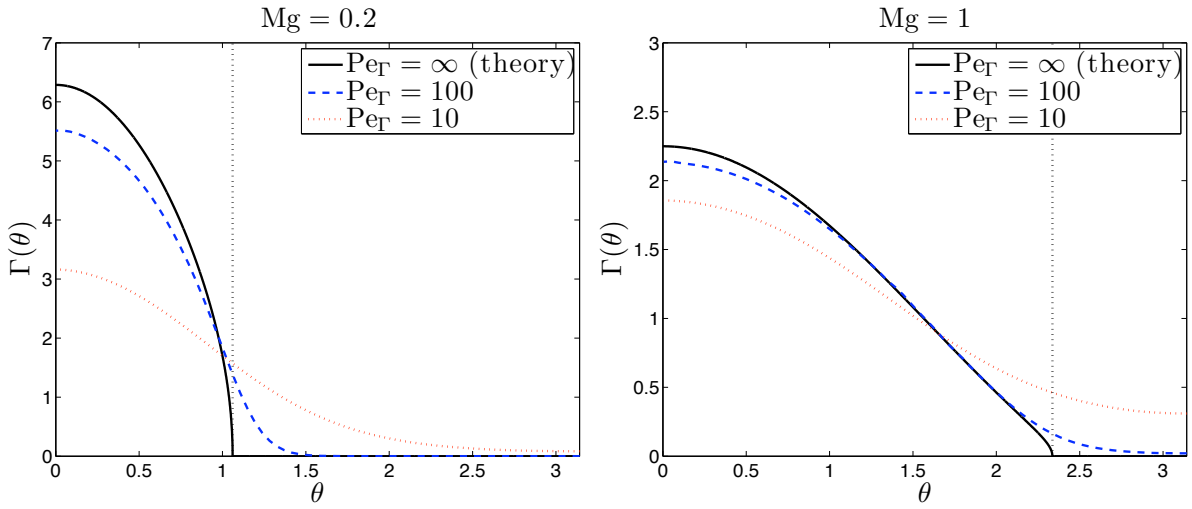

Figure 5.3: Surfactant distribution against angle from the bottom of the drop, for different Péclet numbers and Marangoni numbers. In the theoretical case (solid black) the Reynolds number is given by $\mathrm{Re} = 0$, while in the computational cases (dashed blue and dotted red), $\mathrm{Re} = 1$. The cap angle, θ_c, is shown as a vertical black dotted line.

against the Marangoni number, Mg, for varying Reynolds and Péclet numbers. We see that surfactant effects are inhibited at larger Reynolds numbers. This can be explained by considering the drag on the drop. Surfactant on the drop surface increases drag by partially immobilizing the surface, thus creating a no-slip boundary condition there for the ambient fluid. Increased viscosity favors increased drag by causing a larger volume of exterior fluid to be affected by the drop motion. If the Reynolds number were to become very large, a boundary layer of decreasing width would form around the region region of stagnation, the width of which would measure the amount of fluid being affected by the no-slip condition there. Thus, for smaller Reynolds numbers, such as we consider, it is to be expected that the effect of the stagnant cap on the drop speed decreases with Reynolds number. McLaughlin [84] presents evidence that this trend reverses for larger Reynolds numbers ($\mathrm{Re} > 100$), due to the formation of large wakes. We plotted streamlines for our simulations, and no wake was observed for $\mathrm{Re} \leq 10$ and $\mathrm{Mg} \leq 2$.

On the other hand, surface diffusion, measured by Pe_Γ^{-1}, counters the effect of the Marangoni number, so that the transition from a clean drop to a stagnant surface is much slower. This is to be expected, since surface diffusion smoothes out the surfactant distribution, as seen in figure 5.3. For a smoother distribution, the surface tension gradient, $\partial\gamma/\partial\theta$, will be decreased, resulting in an equivalent decrease in tangential stress. Since it is the tangential stress that relates the surface tension to the rising speed, it is to be expected that a lower Péclet number will result in increased speeds. In the absence of surface diffusion, the tangential stress increases with the Marangoni number, so that the effect of surface diffusion is to counteract the effects of the Marangoni number.

5.4 Entrainment Effects in a Linear Density Stratification

The terminal speed of a rising drop is proportional to the density difference between the drop and the ambient - hence the speed of a drop rising in a density stratification can be expected to decrease

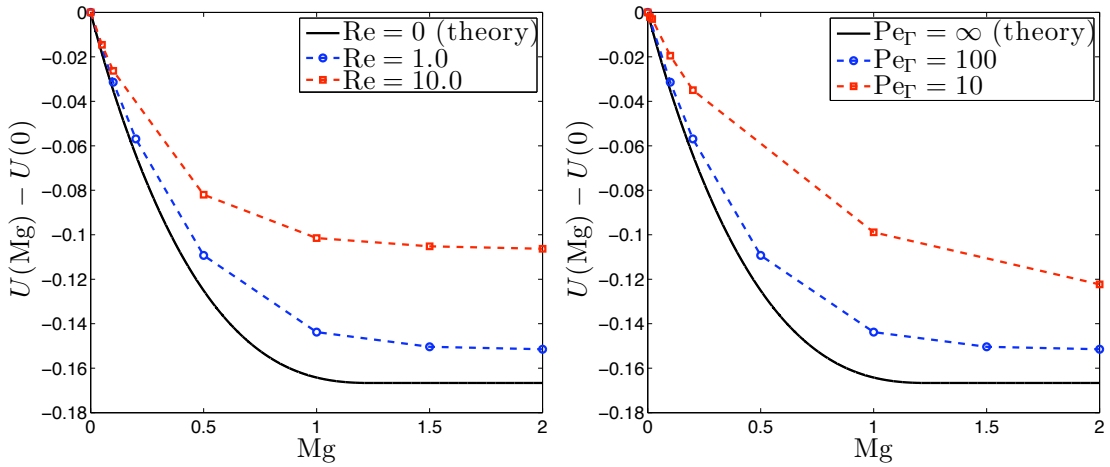

Figure 5.4: Steady-state speed of surfactant-laden drops against Marangoni number, Mg, in a uniform ambient, for differing Reynolds numbers (left) and surface Péclet numbers (right). For the computed results on the left, $\mathrm{Pe}_\Gamma = 100$; for the computed results on the right, $\mathrm{Re} = 1$. In the theoretical case (solid black) the Reynolds number is given by $\mathrm{Re} = 0$ and the Péclet number on the surface is given by $\mathrm{Pe}_\Gamma = \infty$.

with the gradient of the density, given in dimensionless form as

$$S = -\frac{\partial \rho}{\partial z} = -\frac{R_0}{\rho_d}\frac{\partial \widetilde{\rho}}{\partial \widetilde{z}}$$

where the tildes represent dimensional variables. This effect is amplified by the process of entrainment, in which the drop carries heavier fluid with it as it rises into the lighter layer, further decreasing the drop speed [96]. If the transition is sufficiently sharp, the direction of motion may even reverse, and the drop may "bounce" on the layer [97].

The setup we consider involves a drop rising to terminal velocity in a uniform ambient with dimensionless density $\rho = \mathcal{D}$, before entering a linear density stratification, beginning at $z = z_0$, and described by

$$\rho(z) = \mathcal{D} - S(z - z_0) \tag{5.18}$$

when $t = 0$ and $z \geq z_0$. Here the drop never reaches its neutral buoyancy level. We consider several cases, including different Reynolds numbers ($\mathrm{Re} = 1, 20$), Marangoni numbers ($\mathrm{Mg} = 0, 2$), and density gradients ($5 \times 10^{-4} \leq S \leq 5 \times 10^{-3}$). All Péclet numbers were kept as large as numerically feasible ($\mathrm{Pe}_\Gamma = 100$ and $\mathrm{Pe} = 10^4$).

Velocity profiles of the rising drops are shown in figure 5.5. The velocity profiles were smoothed using a gaussian function, to eliminate small scale noise. In all cases, sharper stratifications favor decelerations of the rising drop, so that when $S = 5 \times 10^{-3}$, the drop rapidly decelerates. For a smaller Reynolds number, the drop undergoes a quicker and more dramatic shift in speed. In all cases, the drop transitions to a state of steady deceleration.

To better quantify the transitional period, we computed the derivative dU/dz of the drop speed, shown in figure 5.6. In all cases, dU/dz is near 0 when the drop enters the stratification, and undergoes decaying oscillations after, relaxing toward a fixed negative value. The magnitude of these oscillations increases with S and decreases with the Reynolds number. To better understand how long it takes the drop to transition to a steady deceleration, we examined the inflection points

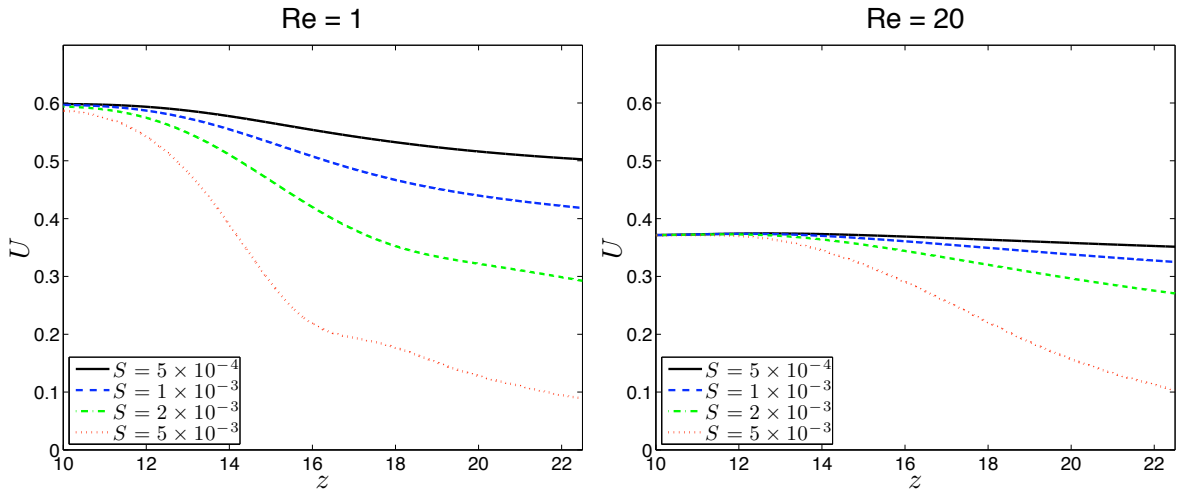

Figure 5.5: The speed U of a drop rising in a linear density stratification, plotted against the vertical position coordinate, z, for different stratifications, and Reynolds numbers of Re = 1 (left) and Re = 20 (right). In all cases, Mg = 2. The linear stratification begins at $z = 10$ and continues throughout.

given by the first local minimum of dU/dz after entering the stratification and measured the vertical displacement, Δz, at which they occur. We found that Δz depends only weakly on the density gradient, S, and the Marangoni number, Mg. However, it depends strongly on the Reynolds number: for Re = 1, $\Delta z \approx 4.8 \pm 0.6$ and for Re = 20, $\Delta z \approx 8 \pm 0.5$. This can be explained by the fact that when Re is larger, the increased inertia delays the transition.

The effects of entrainment can be quantified by comparing our results to an entrainment free case. By running simulations with the ambient density kept constant in time but varying with height, we were able to obtain velocity profiles of rising drops in the absence of entrainment. Figure 5.7 shows velocity profiles with and without entrainment. In the absence of entrainment, the drop quickly assumes a steady deceleration on entering the stratification, which it maintains throughout. With entrainment, the drop undergoes a transitional decrease in velocity before reaching a steady deceleration that is nearly identical to the entrainment-free case. This results in a net velocity lag

$$\Delta U = U_{\text{without entrainment}} - U_{\text{with entrainment}}$$

that is approximately constant once the transient phase is complete. In each case, we computed ΔU by averaging the velocity over an interval $[z_1, z_2]$, with and without entrainment, during the phase where both drops are undergoing steady deceleration, and taking the difference.

In figure 5.8, the velocity lag, ΔU, is plotted against the density gradient, S. The relation is approximately linear for small S. The slopes, b, of the lines $\Delta U = bS$ in figure 5.8 are presented in table 5.2. This relation fails for larger S, and the dependence of ΔU on S becomes sub-linear. The drop and the fluid it entrains act together as a rising body with a mean density. Hence, it is expected that the velocity lag is proportional to the density gradient, until the stratification becomes sufficiently sharp, in which case the drop begins to entrain less fluid. We also find that the velocity lag is greater for larger Marangoni number and smaller Reynolds number. In both cases, this is to be expected because the drop entrains more fluid.

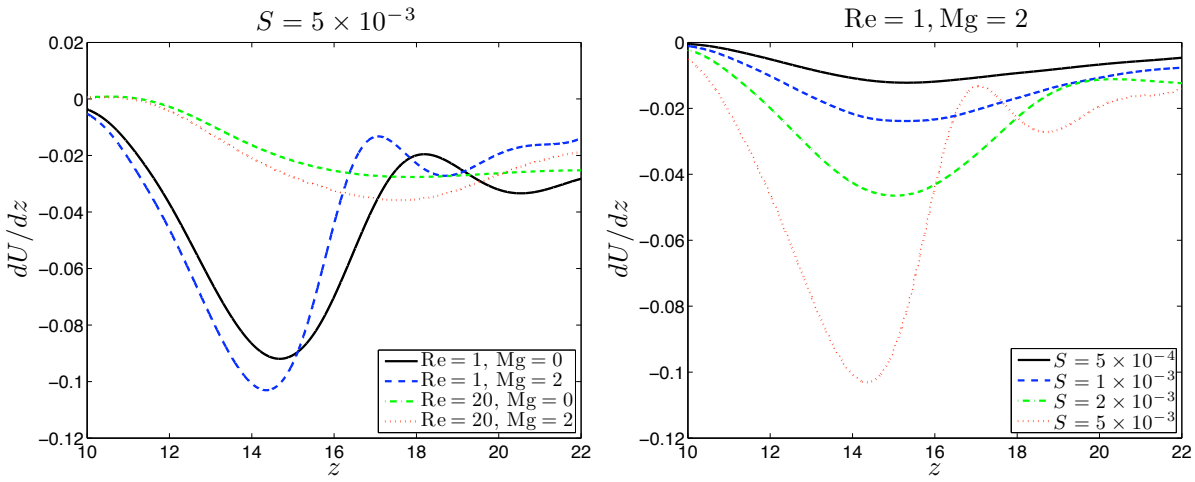

Figure 5.6: The derivative, dU/dz, of the speed of a drop rising in a linear density stratification against position. A side-by-side comparison of velocity derivatives for different Reynolds numbers and Marangoni numbers is shown (left), along with a side-by-side plot of velocity derivatives for different density stratifications (right). The stratification begins at $z = 10$ and continues throughout.

This data allows us to calculate the buoyancy of entrained fluid. After transitional effects have died out, the velocity of the drop at a given height z is determined by a force balance between drag and buoyancy:

$$\mu R_0 \widetilde{U} F(\mathrm{Re}, \mathrm{Mg}) = g V_d \rho_d (\rho(z) - 1) + g V_e \rho_d (\rho(z) - \rho_e(z)) \tag{5.19}$$

where $\widetilde{U} = U U_{\mathrm{HR}}$ is the drop speed, F is a dimensionless function of the Reynolds and Marangoni numbers, V_d and V_e are the respective volumes of the drop and the entrained fluid, $\rho(z) = \mathcal{D} - 1 - S(z - z_0)$ by Eq. (5.18), and ρ_e is the dimensionless density of the entrained fluid. The lefthand side of Eq. (5.19) accounts for the drag force, while the righthand side accounts for the buoyancy - the first term accounting for the drop buoyancy and the second term accounting for the buoyancy of the entrained fluid. We expect that for sufficiently small S, V_e depends on the Reynolds and Marangoni numbers, but not on the vertical displacement or the density gradient.

When the stratification is fixed as a function of height, the second term on the righthand side of Eq. (5.19) vanishes. Solve, to obtain

$$U_f(z) = \frac{g V_d \rho_d}{\mu R_0 F U_{\mathrm{HR}}} \rho(z) = \frac{g V_d \rho_d}{\mu R_0 F U_{\mathrm{HR}}} (\mathcal{D} - 1 - S(z - z_0)) \quad . \tag{5.20}$$

Thus, the slopes of the velocity profiles, $U_f(z) = U_0 - aSz$ (see the dotted lines in figure 5.7), when density is fixed as a function of height, are given by aS, where $a = g V_d \rho_d / \mu R_0 F U_{\mathrm{HR}}$ depends only on the Reynolds and Marangoni numbers.

To proceed further, we assume a functional form for $\rho_e(z)$. In steady deceleration, we postulate that the density of the entrained fluid equals that of the stratified ambient a fixed distance, Δz, below the drop center of mass: $\rho_e(z) = \rho(z - \Delta z)$. Applying Eq. (5.18), we find that $\rho(z) - \rho_e(z) = -S\Delta z$. Thus, buoyancy of the entrained fluid is given relative to the drop weight by

$$\frac{\text{Entrained Buoyancy}}{\text{Drop Weight}} = \frac{g V_e \rho_d (\rho(z) - \rho_e(z))}{g V_d \rho_d} = -S \Delta z \frac{V_e}{V_d} \quad . \tag{5.21}$$

The negative sign indicates that the buoyancy of the entrained fluid drags the drop downward.

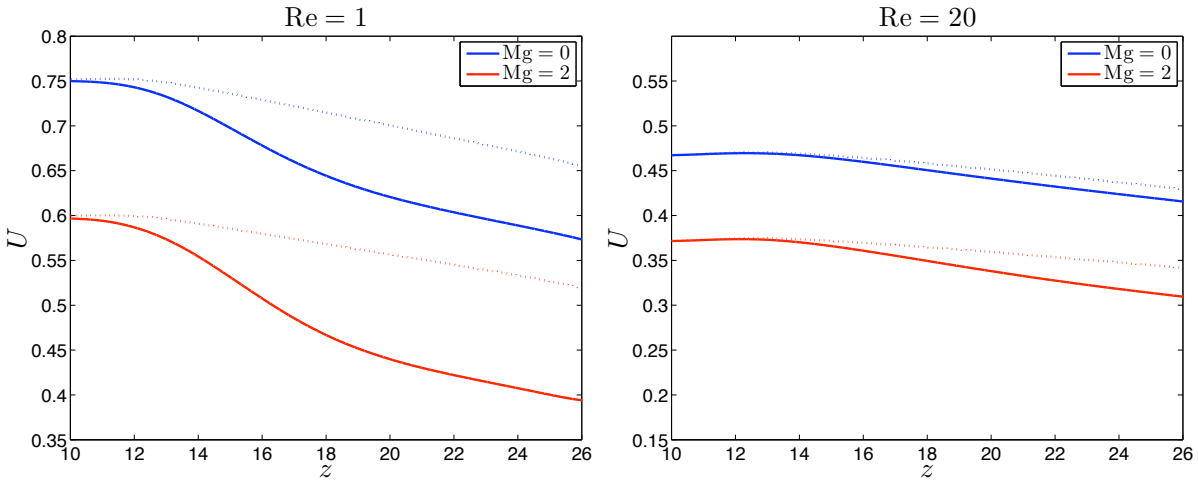

Figure 5.7: The speed U of a drop rising in a linear density stratification, plotted against the vertical position coordinate, z, with entrainment (solid line), and without entrainment (dashed line). Each figure shows two Marangoni numbers: $\mathrm{Mg} = 0, 2$. In both cases, $S = 10^{-3}$.

To compute the factor $\Delta z V_e/V_d$, we form the velocity lag. This can be done by solving Eq. (5.19) for the velocity, $U(z)$, of the rising drop, and subtracting the from velocity, $U_f(z)$, given in Eq. (5.20). Obtain

$$\Delta U = U_f(z) - U(z) = -\frac{gV_e}{\mu U_{\mathrm{HR}} R_0 F}(\rho(z) - \rho_e(z)) = \frac{SgV_e\rho_d\Delta z}{\mu U_{\mathrm{HR}} R_0 F} = a\Big(\Delta z \frac{V_e}{V_d}\Big)S$$

Since $\Delta U = bS$, where the values of b are given in table 5.2, we conclude that $\Delta z V_e/V_d = b/a$. The factor $\Delta z V_e/V_d$ is also given in table 5.2.

Re	Mg	b	$\Delta z V_e/V_d$
1	0	748	11.23 ± 0.07
1	2	1130	21.8 ± 1.9
20	0	140	3.55 ± 0.03
20	2	318	9.78 ± 0.25

Table 5.2: The factor $\Delta z V_e/V_d$, in the entrained buoyancy (see (5.21)). As seen in figure 5.8, the linear relation $\Delta U = bS$ holds for S sufficiently small, and breaks down thereafter. The slopes, b, of the lines in figure 5.8 are also given.

5.5 A Clean Drop Entering a Surfactant Layer

The next setup we consider involves a clean drop rising into a bath of soluble surfactant. We begin our simulation when the drop is at rest and allow it to accelerate to a steady rising speed before entering a layer of soluble surfactant dissolved in the ambient. The layer begins at a height of $z = 10$ in the cylindrical domain, and sharply transitions between a clean bulk ($\Lambda = 0$) and a saturated bulk ($\Lambda = 1$), over the course of 0.1 drop radii. The transition is linear, and takes place over the range $9.95 \le z \le 10.05$. The intended application is the case of an oil drop rising to the surface of

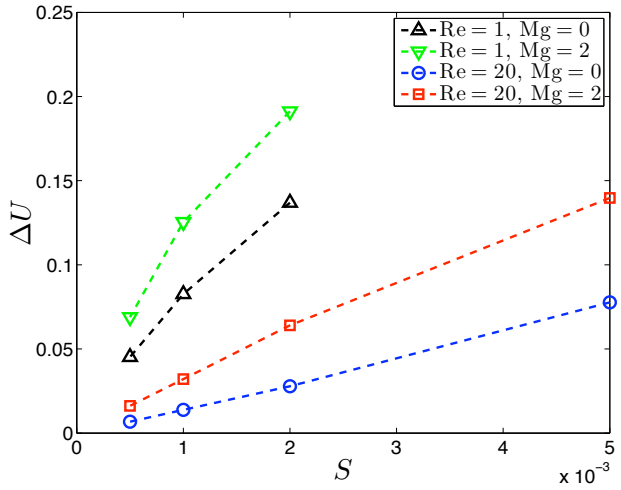

Figure 5.8: The lag, ΔU, in the speed of a rising drop caused by entrainment effects, against the dimensionless density gradient of the fluid.

the ocean, encountering a layer of surfactants that have been sprayed on the water (as in the 2010 BP oil spill). Diffusion is kept small: $\mathrm{Pe}_\Lambda = 10^4$, $\mathrm{Pe}_\Gamma = 100$. For simplicity, we fix the Marangoni number at $\mathrm{Mg} = 2$.

Figure 5.9 shows smoothed plots of the speed of the rising drop after it enters the surfactant bath. In all cases, the drop accelerates after entering the bath and subsequently decelerates to a steady ascent, with a lower velocity than before. This can be explained by the surface tension gradient on the drop, shown in figure 5.10. The top of the drop enters the bath first, adsorbing surfactant. The surfactant thus lowers the surface tension at the top of the drop relative to that of the bottom, resulting in a surface tension gradient that "sucks" the drop into the layer. Afterward, convection carries the surfactant toward the bottom of the drop, producing a gradient in the opposite direction that inhibits the rising of the drop - thus resulting in a decreased steady-state speed.

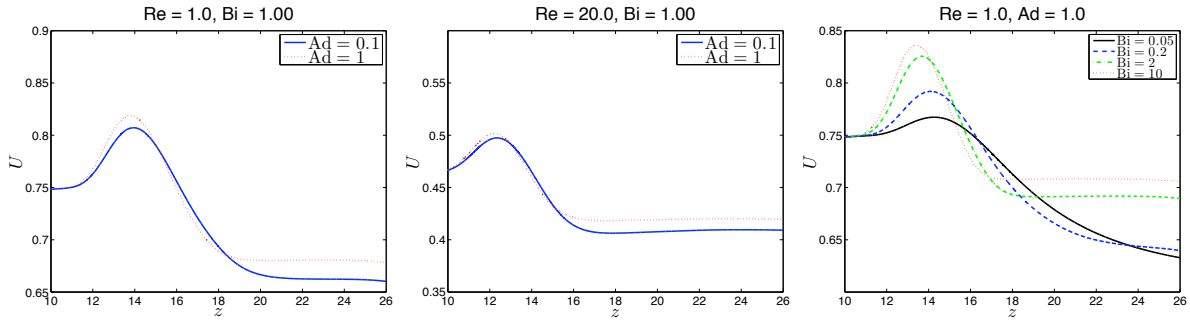

Figure 5.9: The speed U of a drop entering a layer of soluble surfactant, whose concentration sharply transitions from $\Lambda = 0$ to $\Lambda = 1$ over the interval $9.95 \leq z \leq 10.05$. The speed of the rising drop is plotted against the vertical position coordinate, z, for different Adsorption numbers, with Reynolds numbers of $\mathrm{Re} = 1$ left) and $\mathrm{Re} = 20$ (center). Side by side plots of multiple Biot numbers are also shown (right).

A larger Biot number accelerates the initial adsorption process and produces a sharper surface tension gradient, which results in more suction. The terminal speed also increases with an increased Biot number, because the sorption process tends to even out the surfactant concentration - higher concentrations of surfactant desorb faster, while lower concentrations adsorb faster. This results in weaker surface tension gradients opposing the the drop motion.

In all cases, we predict that the vertical component of the surface tension gradient is the primary factor determining changes in the velocity profile of the drop. This hypothesis can be tested by forming a predicted velocity profile, based on the surface tension gradient:

$$U_{\text{pred}} = U\big|_{z=10} + a\overline{\nabla\gamma \cdot \mathbf{k}} \tag{5.22}$$

where $a > 0$ is a calibration parameter and $\overline{\nabla\gamma \cdot \mathbf{k}}$ is the average vertical component of the surface tension gradient on the drop, given by

$$\overline{\nabla\gamma \cdot \mathbf{k}} = \frac{1}{\pi}\int_0^\pi \frac{d\gamma}{ds}\sin\varphi ds \approx \frac{1}{n}\sum_{k=1}^{n-2}\frac{\gamma_{k+1}-\gamma_{k+1}}{s_{k+1}-s_{k+1}}\sin\varphi_k \quad .$$

The rightmost expression shows our method of computing $\overline{\nabla\gamma \cdot \mathbf{k}}$ from the numerical data. n is the number of markers, indexed by k, and φ_k is the vertical angle of the k^{th} marker measured from the drop center. The above summation does not include the endpoints because when $k = 0, n-1$, $\varphi = 0, \pi$, so $\sin\varphi = 0$. Figure 5.11 shows predicted verses computed velocities for given Adsorption and Biot numbers. Our prediction is highly accurate for a Reynolds number of Re = 1, and less accurate when Re = 20. The most noticeable difference takes the form of a lag, or a delay in velocity changes, which can be explained by inertial effects. In addition, the predicted velocity is shifted vertically from the actual velocity. We suspect that the vertical shift is due to the fact that the drop hasn't quite reached terminal velocity by the time it enters the stratification. The results are similar for different Biot and Adsorption numbers.

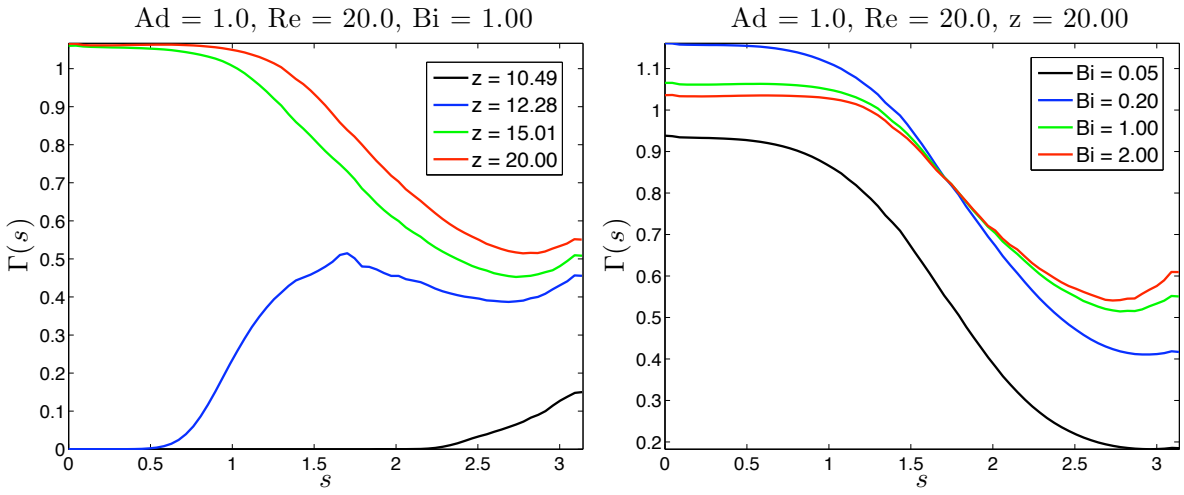

Figure 5.10: Surfactant profiles on the drop at a Reynolds number of Re = 20, an adsorption number of Ad = 1, at various heights when Bi = 1 (left), and for various Biot numbers when the drop is at height $z = 20$ (right).

The terminal velocity, U_∞, normalized by the steady-state velocity of a clean drop, is shown in figure 5.12 as a function of the Biot number. The results are given for a Reynolds number of Re = 1

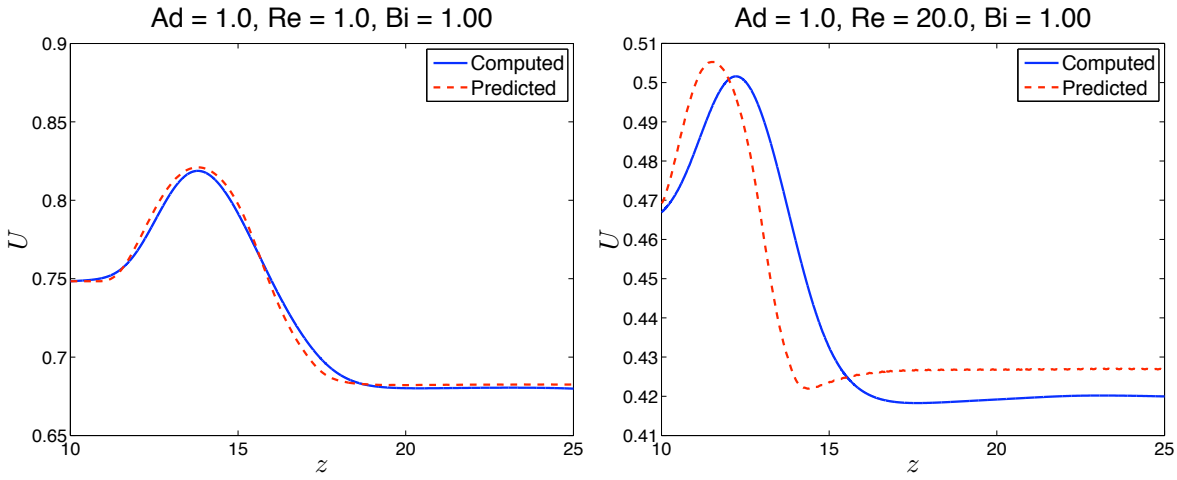

Figure 5.11: Computed velocity verses a prediction based on surface tension gradients (see Eq. (5.22)), for Reynolds numbers of Re = 1 (left) and Re = 20 (right). In both plots Ad = Bi = 1.

and are similar for a Reynolds number of Re = 20. Although we ran simulations for Biot numbers as low as 0.02, figure 5.12 only includes the Biot numbers for which terminal velocity was reached within our computational domain. As Bi $\longrightarrow \infty$, we expect we expect U_∞ to approach the speed of a clean drop, and as Bi $\longrightarrow 0$, we expect U_∞ to approach the speed of a drop contaminated by insoluble surfactant (see figure 5.4). When normalized by U_{clean}, this is approximately 0.8. This gives rise to a paradox, because when Bi = 0, the drop will always be clean, because it never absorbs surfactant. This paradox is resolved by recognizing that the time it takes to transition to steady-state goes to ∞ as the Biot number approaches 0. These results are similar to previous results for creeping flow [12].

The transient effects include two key elements: the suction experienced by the drop on entering the surfactant layer, and the time it takes to transition to steady state. The suction effects can be measured by the maximum velocity obtained. Figure 5.13 shows this maximum velocity plotted against the Biot number, shown on a logarithmic scale. The velocity in figure 5.13 is normalized by the steady-state speed of a clean drop. The results are given for a Reynolds number of Re = 20, and are similar for a Reynolds number of Re = 1. As Bi $\longrightarrow 0$, we expect $U_{\max}$ to approach 1, the terminal speed of a clean drop. As Bi $\longrightarrow \infty$, we expect the terminal speed to approach a maximal finite value, determined by a balance of convection and diffusion.

The duration of the transition to equilibrium can be measured by the displacement, z_{trans}, at which the drop has approximately reached its equilibrium speed. In figure 5.14 these transitional displacements are plotted against the Biot number. z_{trans} was chosen to be the displacement at which the drop comes within 1% if its equilibrium velocity. Note that z_{trans} is defined relative to the surfactant layer, so that $z_{\text{trans}} = 0$ when $z = 10$. The results are given for a Reynolds number of Re = 20, and are similar for a Reynolds number of Re = 1. We expect that $z_{\text{trans}} \longrightarrow \infty$ as Bi $\longrightarrow 0$. On the other hand, as Bi $\longrightarrow \infty$, z_{trans} approaches a positive minimum in which the transition to equilibrium is determined entirely by convection. We note that the results were somewhat resolution sensitive - increasing the resolution resulted in a 2% shift in the terminal velocities, but the overall trends should remain the same.

Altogether, we have found that a drop rising at steady state into a layer of soluble surfactant undergoes changes in velocity based on the surfactant gradient on the surface. As the drop first

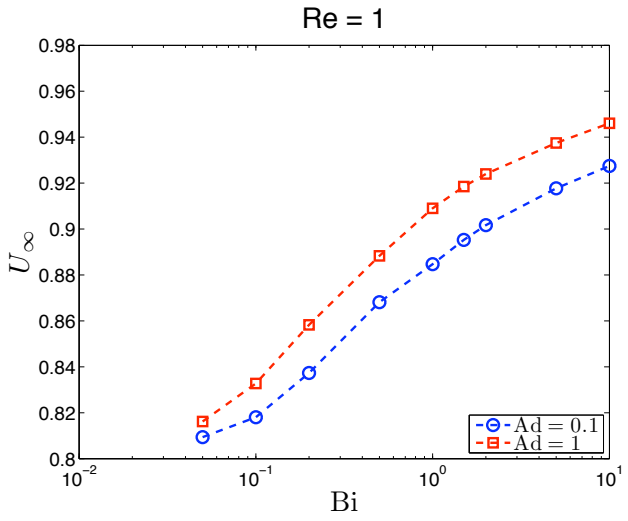

Figure 5.12: Steady-state velocity verses Biot number, for different adsorption numbers. The velocity is normalized by the steady-state velocity of a clean drop for the same Reynolds number. As Bi $\to \infty$, we expect the normalized velocity to go to 1 (the velocity of a clean drop). As Bi $\to 0$, we expect the normalized velocity to go to about 0.8 (the velocity of a drop contaminated by insoluble surfactant).

enters the layer, surfactant adsorbs onto the top of the drop, resulting in a surface tension gradient that is increasing toward the base of the drop, and which sucks the drop into the layer. Once the surfactant is convected toward the bottom of the drop, the surface tension gradient reverses itself, resulting in a drag that slows the speed of the rising drop.

We have described the effects of the Biot number on this process. In particular, a larger Biot number results in sharper gradients during the suction phase, and milder gradients later on, so that the velocity of the rising drop is increased in both cases. In addition, we have described the length of the transition to steady-state by measuring the displacement at which the drop speed has an inflection point - a larger Biot number leading to a faster transition.

5.6 Conclusion

In summary, we have combined, for the first time, two related fields of study: surfactant effects on drop speed, and rising through a stratification. For drops rising in an unstratified medium, coated in insoluble surfactant, we have obtained results that are consistent with, and expand upon existing work [9]. In particular, we have explored the effects of surface diffusion, and a relatively small but nonzero Reynolds number on drop speed - bridging the gap between the theory for creeping flow [9] and existing work for intermediate Reynolds number [84, 86]. Surfactant effects were slightly weaker in the presence of inertia, due to the fact that less fluid is entrained as a consequence of the no-slip condition on the stagnant cap. The surface Péclet number was found to counter surfactant effects, measured by the Marangoni number, by spreading the surfactant across the interface.

When the drop entered a linear density gradient, we observed a transition to steady deceleration that depended mainly on the Reynolds number - the higher the Reynolds number, the longer the transition. After this transitional period, the drop reached a steady deceleration, which was similar

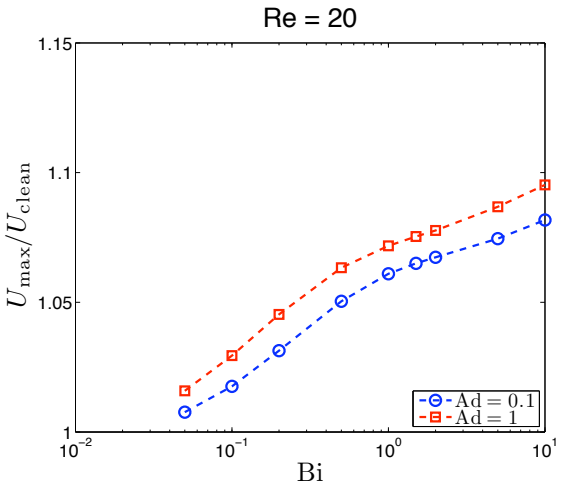

Figure 5.13: Maximum velocity attained verses Biot number, for Re = 20 and different adsorption numbers. The results for Re = 1 were similar. The velocity is normalized by the steady-state velocity of a clean drop for the same Reynolds number. As Bi $\to$ 0, we expect the normalized velocity to go to 1.

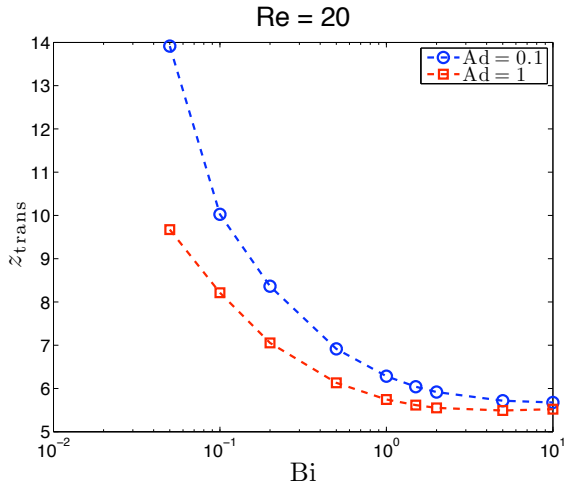

Figure 5.14: Displacement at which the drop comes within 1% of its terminal speed verses verses Biot number, for Re = 20 and for different adsorption numbers. The results for Re = 1 were similar. z_c is measured from the start of the surfactant layer, and therefore is offset by 10 drop radii from the vertical position coordinate, z. We expect z_{trans} to go to infinity as Bi $\to$ 0. As Bi becomes large, z_{trans} reaches a positive minimum.

with and without entrainment, except that for the existence of a roughly uniform velocity lag. This lag was observed to increase linearly with the density gradient, and also depended on the Reynolds and Marangoni numbers. This work could be extended by more carefully quantifying the effect of the Reynolds and Marangoni numbers on the entrained buoyancy (table 5.2).

Finally, we observed for the first time what happens to a clean drop upon entering a surfactant layer. On first entering the layer, the drop underwent an acceleration as it was sucked into the layer, because of the upward surface tension gradient created by the uneven surfactant adsorption. Afterward, it underwent a transition toward steady-state. We found that our results for steady-state velocity are in good agreement with existing results for creeping flow [12]. In all of this, we quantified the effects of the Biot number, which accelerates sorption the process, resulting in greater sorption on entering the layer, and an increased rising speed at steady-state. Due to the large number of parameters at play, we mostly ignored the effects of the Marangoni number and the adsorption number for this portion of the study, holding both of these dimensionless parameters constant.

Chapter 6

Extension to Electric Fields

The coalescence and breakup of charged drops in the presence of an electric field plays a key role in cloud formation. In addition, electric fields are frequently used for de-emulsification, particularly of water in crude oil [114], and for droplet manipulation in microfluidic devices, including droplet fusion and breakup [115, 116], droplet transportation [117], and electroporesis in cells [118]. Electric fields also have applications to dewetting, as drops under the influence of an applied field have been known to leap from a solid surface.

G.I. Taylor [119] demonstrated that drops elongate and eventually break apart in the presence of an electric field. Since then, a number of studies have observed surprising behavior in droplets under the influence of an electric field, including partial coalescence [120–124] and non-coalescence, even after contact [125]. In applications to de-emulsification, these behaviors are generally undesirable - especially electrically induced partial coalescence.

In this chapter, we present adaptations of our method to track electric charges and compute an electric field on our computational domain.

6.1 Governing Equations

6.1.1 Dimensional Equations

The applications we intend involve lengthscales on the order of a millimeter or less, in which magnetic fields can be neglected [126]. In this case, electric fields can be incorporated into the incompressible Navier-Stokes using the Maxwell stress tensor, given by [126]:

$$\mathbb{T}^e = \varepsilon \mathbf{E}\mathbf{E} - \frac{1}{2}\varepsilon \mathbf{E}\cdot\mathbf{E}\boldsymbol{\delta} \tag{6.1}$$

where $\mathbf{E}$ is the electric field, $\boldsymbol{\delta}$ is the identity tensor, and ε is the dielectric constant. Then the equations of fluid motion are

$$\nabla\cdot\mathbf{u} = 0 \tag{6.2}$$

$$\rho\frac{\partial \mathbf{u}}{\partial t} + \rho\mathbf{u}\cdot\nabla\mathbf{u} = -\nabla P + \nabla\cdot(\mathbb{T}+\mathbb{T}^e) - g(\rho-\rho_a)\mathbf{k} + \delta_s(\gamma\kappa\mathbf{n} + \nabla_s\gamma) \quad . \tag{6.3}$$

As in Eq. (2.2), the viscous stress tensor, $\mathbb{T}$, is given by

$$\mathbb{T} = \mu(\nabla \mathbf{u} + \nabla \mathbf{u}^T) \quad . \tag{6.4}$$

It is instructive to examine the pressure jump across the interface. Integrating the normal component of Eq. (6.3) across the interface in a normal direction, over an interval Δn (here, n is the local coordinate normal to the interface), and taking the limit as $\Delta n \longrightarrow 0$, we arrive at the form

$$\|P\| = \gamma\kappa + 2\|\mu\| \left.\frac{\partial u_n}{\partial n}\right|_s + \frac{1}{2}\left\|\varepsilon(E_n^2 - E_s^2)\right\| \quad . \tag{6.5}$$

The lefthand side of equation (6.5) comes from the pressure gradient in the Navier-Stokes. On the righthand side, the first term comes from the surface force, and represents a Laplace pressure. The second term on the right comes from the viscous stress tensor, in the case when the viscosity is discontinuous across the interface. The third term comes from the Maxwell stress tensor in the case when the electric field is discontinuous across the interface. For a stable spherical drop, the pressure jump across the interface will balance the stresses on the righthand side. In the presence of a surface charge, q, the tangential portion of the Maxwell tensor also has a discontinuity across the interface. Altogether,

$$\|\mathbb{T}^e \cdot \mathbf{n}\| = \frac{1}{2}\left\|\varepsilon(E_n^2 - E_s^2)\right\| \mathbf{n} + q\mathbf{E}_s \quad . \tag{6.6}$$

In the absence of Magnetic forces, Maxwell's equations reduce to the following:

$$\nabla \cdot (\varepsilon \mathbf{E}) = \rho^e \quad , \tag{6.7}$$

$$\nabla \times \mathbf{E} = \mathbf{0} \quad . \tag{6.8}$$

Here, ρ^e is the volumetric charge density. The jump in the electric field across the interface can be written in terms of the charge per unit area, q:

$$\|\varepsilon \mathbf{E}\| \cdot \mathbf{n} = q \quad . \tag{6.9}$$

Because $\mathbf{E}$ is irrotational, it can be written as the gradient of an electric potential, φ: $\mathbf{E} = \nabla\varphi$. Incorporating the surface charge into Eq. (6.7) using a delta function, we obtain the following relation, valid on the entire domain:

$$\nabla \cdot (\varepsilon \nabla \varphi) = \rho^e + \delta_s q \quad . \tag{6.10}$$

Recall that δ_s is a delta function that is nonzero only on the interface.

In general, accounting for the electric charge requires tracking species of ions dissolved in the fluid and adsorbed onto the interface. A single ionic compound involves three species of ions: positive, negative, and neutral. For example, sodium-chloride (table salt), consists of positive sodium (Na^+) ions, negative chloride Cl^- ions, and neutral NaCl molecules. For the moment, we use the Taylor-Melcher approximation [126], tracking net charge using an advection-diffusion equation with electrical forcing:

$$\frac{\partial \rho^e}{\partial t} + \mathbf{u} \cdot \nabla \rho^e = \nabla \cdot (-\sigma \mathbf{E} + k_e \nabla \rho^e) \quad . \tag{6.11}$$

The Taylor-Melcher model relies on the assumption of electro-neutrality, according to which the total number of charges is large in comparison to the net charge at any given location. Of course, this assumption breaks down on sufficiently small lengthscales. The range of problems to which this model is applicable is controversial, especially for multiphase flow [120, 126, 127]. In Eq. (6.11), σ is the electrical conductance of the material and k_e is a diffusion coefficient. Integrating Eq. (6.11) across the interface and adding a surface diffusion term, we obtain

$$\frac{\partial q}{\partial t} + \mathbf{u} \cdot \nabla_s q + \mathbf{u} \cdot \mathbf{n}(\mathbf{n} \cdot \nabla q) = \|-\sigma \mathbf{E} + k_e \nabla \rho^e\| \cdot \mathbf{n} + \nabla_s \cdot (k_q \nabla_s q) \tag{6.12}$$

where k_q is a diffusion coefficient on the surface. The surface diffusion term in Eq. (6.12) is usually neglected because the surface diffusion is assumed to be small, but we include it here for numerical stability.

For most applications, we will set the voltage to zero on the boundary. We account for an applied electric field separately, by adding the applied field, $E_0\mathbf{k}$, to the electric field in the Maxwell tensor (6.1) and the charge tracking equations (6.11) and (6.12), but not the charge equation (6.10). We assume the charge is zero on the walls, and symmetric at the axis.

6.1.2 Dimensionless Equations

We nondimensionalize our governing equations using a very simple and very general scheme. Let L be a length-scale and U be a velocity scale (this is equivalent to using a timescale $t_0 = L/U$). Redefine our parameters:

$$\mathbf{u}_{\text{new}} = \mathbf{u}_{\text{old}}/U, \quad t_{\text{new}} = U t_{\text{old}}/L, \quad \nabla_{\text{new}} = L\nabla_{\text{old}}, \quad (\delta_s)_{\text{new}} = L(\delta_s)_{\text{old}}, \quad \kappa_{\text{new}} = L\kappa_{\text{old}} \quad .$$

We also choose generic scales $\rho_0, \gamma_0, \mu_0, E_0$ for the density, surface tension, viscosity, and electric field:

$$\rho_{\text{new}} = \rho_{\text{old}}/\rho_0, \quad (\rho_a)_{\text{new}} = (\rho_a)_{\text{old}}/\rho_0, \quad \gamma_{\text{new}} = \gamma_{\text{old}}/\gamma_0, \quad \mu_{\text{new}} = \mu_{\text{old}}/\mu_0, \quad \mathbf{E}_{\text{new}} = \mathbf{E}_{\text{old}}/E_0 \quad .$$

Naturally, we choose ε_0, the permittivity of free space, to scale our dielectric coefficient, so that $\varepsilon_{\text{new}} = \varepsilon_{\text{old}}/\varepsilon_0$. For simplicity, we scale our momentum equation by dividing out the inertia: $\rho_0 U^2/L$. Scale the pressure by the inertial pressure: $P_0 = \rho_0 U^2$. Then the equations of fluid motion become

$$\nabla \cdot \mathbf{u} = 0 \tag{6.13}$$

$$\frac{\partial \mathbf{u}}{\partial t} + \rho \mathbf{u} \cdot \nabla \mathbf{u} = -\nabla P + \nabla \cdot \left(\mathrm{Re}^{-1}\mathbb{T} + N_{ei}\mathbb{T}^e\right) - \mathrm{Ri}(\rho - \rho_a)\mathbf{k} + \mathrm{We}^{-1}\delta_s(\gamma\kappa\mathbf{n} + \nabla\gamma) \quad . \tag{6.14}$$

Here, we have the familiar Reynolds number and Weber number, as well as the Richardson number

$$\mathrm{Ri} = \frac{gL}{U^2} \tag{6.15}$$

and the electro-inertial number

$$N_{ei} = \frac{\rho_0 U^2}{\varepsilon_0 E_0^2} \quad . \tag{6.16}$$

We scale the surface charge as $q_{\text{new}} = q_{\text{old}}/\varepsilon_0 E_0$ so that equation (6.9) is unchanged:

$$\|\varepsilon \mathbf{E}\| \cdot \mathbf{n} = q \quad . \tag{6.17}$$

If we put $\varphi_{\text{new}} = \varphi_{\text{old}}/LE_0$ and $\rho^e_{\text{new}} = \rho^e_{\text{old}}/\rho^e_0$, where $\rho^e_0 = \varepsilon_0 E_0/L$ then equation (6.10) is unchanged:

$$\nabla \cdot (\varepsilon \nabla \varphi) = \rho^e + \delta_s q \quad . \tag{6.18}$$

We nondimensionalize the conductivity by putting $\sigma_{\text{new}} = \sigma_{\text{old}}/e\omega_0\rho^e_0$, where ω_0 is a standard drift velocity. When tracking individual ion species, it is necessary to account for the drift velocity of each ion species. However, in the Ohmic regime that we consider here, we instead use an effective drift velocity for the charge. Then our charge tracking equations become

$$\text{Re}_\text{e}\left(\frac{\partial \rho^e}{\partial t} + \mathbf{u}\cdot\nabla\rho^e\right) = \nabla\cdot\left(-\sigma\mathbf{E} + \text{Io}^{-1}\nabla\rho^e\right) \tag{6.19}$$

$$\text{Re}_\text{e}\left(\frac{\partial q}{\partial t} + \mathbf{u}\cdot\nabla_s q + \mathbf{u}\cdot\mathbf{n}(\mathbf{n}\cdot\nabla q)\right) = \left\|-\sigma\mathbf{E} + \text{Io}^{-1}\nabla\rho^e\right\|\cdot\mathbf{n} + \nabla_s\cdot(\text{Io}_s^{-1}\nabla_s q) \quad . \tag{6.20}$$

Three dimensionless numbers appear in equations (6.19) and (6.20):

$$\text{Io} = \frac{e\omega_0 E_0 L}{k_e} \qquad \text{(Ionic Drift Number)} \tag{6.21}$$

$$\text{Io}_s = \frac{e\omega_0 E_0 L^2}{k_q} \qquad \text{(Ionic Drift Number on the surface)} \tag{6.22}$$

$$\text{Re}_\text{e} = \frac{U}{e\omega_0 E_0} \qquad \text{(Electric Reynolds Number)} \quad . \tag{6.23}$$

6.2 Numerical Method

In the application of our method, we envision the following setup: two fluids are separated by an interface; one is a conductor, the other is not. The conducting fluid most likely to occur in the applications we consider is water - particularly with dissolved ionic substances, such as salts. Other conducting fluids include liquid metals, astrophysical systems, and plasma. Non-conducting fluids include air and oil. Quantities associated to the conducting fluid are subscripted with c, while quantities associated to the non-conducting fluid are subscripted with x. We assume the conductivity of the non-conducting fluid is zero, and denote the conductivity of the conducting fluid by σ. A charge, with density ρ^e, resides within the bulk of the conductor, and a charge, with density q, resides on the interface. We assume that the normal, $\mathbf{n}$, to the interface points away from the conducting fluid.

6.2.1 Charge Equation

Recall that the pressure, P, is computed at cell centers, as an array whose elements are denoted $P_{i,j}$, and the surfactant concentration is computed at the markers. In particular, the surfactant concentration at the k^{th} marker is written Γ_k. Similarly, we store the bulk charge distribution, ρ^e, at cell centers (denoted with $\rho^e_{i,j}$) and the surface charge distribution, q, at markers on the interface (denoted with q_k). We can combine the two types of charge into a single charge distribution on the MAC grid by averaging q over the grid cell. This process makes use of machinery we have already developed for numerical integration:

$$\rho^{\text{tot}}_{i,j} = \rho^e_{i,j} + \frac{1}{\Delta A}\iint_{\text{cell}} \delta_s q dA = \rho^e_{i,j} + \frac{1}{\Delta A}\int_{s_1}^{s_2} q ds$$

where s_1, s_2 are the arc-lengths where the front intersects the cell. Thus, having computed the right-hand side of the Poisson equation (6.18), we can solve the equation using the same iterative method we used to invert the pressure equation, and obtain the electric potential, φ. Taking the gradient of φ, we obtain the components, E_r and E_z, of the electric field. Because φ is not differentiable at the interface, we use one-sided derivatives to compute the components of the electric field near the interface.

6.2.2 Electric Forcing Terms

Notice that equations (6.13) and (6.14) are simply the Navier-Stokes (2.1)-(2.2) with added electrical forcing, and equations (6.11) and (6.12) are the same as our standard equations (2.8)-(2.9) for tracking scalar fields in the bulk and on the surface, respectively - except with added terms based on the electrical force. Having computed the electric field, $\mathbf{E}$, all of these equations can be solved simply by adding forcing terms to our existing method. We therefore focus here on describing our numerical treatment of the electric field.

In an axisymmetric setup, the electric field can be written as $\mathbf{E} = E_r\mathbf{e}_r + E_z\mathbf{e}_z$. Significantly, the azimuthal coordinate is zero: $E_\theta = 0$. Then the Maxwell stress tensor can be written as follows:

$$\mathbb{T}^e = \varepsilon \begin{pmatrix} E_r^2 & 0 & E_rE_z \\ 0 & 0 & 0 \\ E_zE_r & 0 & E_z^2 \end{pmatrix} - \frac{1}{2}\varepsilon(E_r^2 + E_z^2)\boldsymbol{\delta} = \frac{1}{2}\varepsilon \begin{pmatrix} E_r^2 - E_z^2 & 0 & 2E_rE_z \\ 0 & -E_r^2 - E_z^2 & 0 \\ 2E_zE_r & 0 & E_z^2 - E_r^2 \end{pmatrix} \quad .$$

Now, the components, E_r and E_z, of the electric field are stored on the vertical and horizontal walls of the cells, respectively, along with the components of the velocity field (see figure 3.2). However, the diagonal components of the stress tensor are stored at cell centers, along with the pressure. As such, after computing the squares, E_r^2, E_z^2 of the electric field components, we take the average across each cell center. The off-diagonal components of the stress tensor reside on the lower lefthand corners of the cells, so we average the components E_r, E_z before multiplying them. After computing $\mathbb{T}^e$ from $\mathbf{E}$, we may simply add it to $\mathbb{T}$ before taking the tensor divergence.

The electrical term in the bulk charge tracking equation can be efficiently computed by replacing it with a charge term. In particular, if we have a constant conductivity, σ, on the conductor, and zero conductivity on the non-conducting fluid, we have

$$\nabla \cdot (\sigma\mathbf{E}) = \frac{\sigma}{\varepsilon_c}\nabla \cdot (\varepsilon_c\mathbf{E}) = \frac{\sigma}{\varepsilon_c}\rho^e$$

on the interior fluid. Since $\rho^e = 0$ on the exterior fluid, this relation is actually valid everywhere. Altogether, we convert equation (6.19) to the form:

$$\mathrm{Re_e}\left(\frac{\partial\rho^e}{\partial t} + \mathbf{u}\cdot\nabla\rho^e\right) = -\frac{\sigma}{\varepsilon_c}\rho^e + \mathrm{Io}^{-1}\nabla^2\rho^e \tag{6.24}$$

On the other hand, we keep equation (6.20) for surface charge unchanged. We rewrite using the assumption of zero charge and conductivity on the nonconducting fluid:

$$\mathrm{Re_e}\left(\frac{\partial q}{\partial t} + \mathbf{u}\cdot\nabla_s q + \mathbf{u}\cdot\mathbf{n}(\mathbf{n}\cdot\nabla q)\right) = \left(-\sigma\frac{\partial\varphi}{\partial n} + \mathrm{Io}^{-1}\frac{\partial\rho_e}{\partial n}\right)\Big|_c + \nabla_s\cdot(\mathrm{Io}_s^{-1}\nabla_s q) \quad . \tag{6.25}$$

Here, the subscript c implies evaluation on the conducting side of the interface. Computing the derivatives, $\partial\varphi/\partial n$ and $\partial\rho^e/\partial n$, requires care, since neither quantity is differentiable at the interface

- and ρ^e is actually discontinuous. Let us focus on the derivative of ρ^e, as φ is handled similarly. Expand the derivative using the chain rule:

$$\frac{\partial \rho^e}{\partial n} = \frac{\partial \rho^e}{\partial r}\frac{dn}{ds} + \frac{\partial \rho^e}{\partial z}\frac{dn}{ds} = -\frac{\partial \rho^e}{\partial r}\frac{dz}{ds} + \frac{\partial \rho^e}{\partial z}\frac{dr}{ds} \quad .$$

The leftmost expression above comes from the geometric relation between the tangent $\mathbf{t} = (r'(s), z'(s))$ and and normal $\mathbf{n} = (-z'(s), r'(s))$ vectors at the interface. Since our method already computes dr/ds and dz/ds, all that remains is to compute the derivatives $\partial\varphi/\partial r$ and $\partial\varphi/\partial z$. For this, we use one-sided linear extrapolation, similar to what we did for the components of the electric field.

6.3 Validation

We validate our method by testing it against a simple case that admits an exact solution. Consider a charged drop of radius R_0 in an isotropic fluid (no gravity), insulated from external electic forces by a spherical insulator of radus R_1 concentric with the drop. Because of symmetry and incompressibility, the fluid remains at rest, even though the charge will not. Assuming magnetic effects can be neglected, the electric field can be written as the gradient of a potential, φ, which satisfies a Poisson equation, derived from Maxwell's charge equation:

$$\nabla^2\varphi = \nabla \cdot \mathbf{E} = \frac{\rho^e}{\varepsilon} \tag{6.26}$$

We assume the charge outside the drop is negligible, ion mobility is negligible, and conductivity is uniform and constant. Then the charge in the drop interior moves according to the equation

$$\frac{\partial \rho^e}{\partial t} = -\sigma\nabla \cdot \mathbf{E} = \sigma\nabla^2\varphi = -\frac{\sigma}{\varepsilon_d}\rho^e \tag{6.27}$$

where ε_d is the permittivity of the drop. For simplicity, we assume a uniform initial condition on the charge: $\rho^e(R, t = 0) = \rho_0^e$. Then Eq. (6.27) is easily solved, obtaining

$$\rho^e(R, t) = \rho_0^e e^{-\sigma t/\varepsilon_d} \tag{6.28}$$

Now we compute the surface charge, $q(t)$, as a function of time given no initial charge $q(0) = q_0$. The governing equation for the surface charge is obtained from conservation of total charge, Q:

$$\frac{4}{3}\pi\rho_0^e R_0^3 + 4\pi R_0^2 q_0 = Q = 4\pi R_0^2 q(t) + \frac{4}{3}\pi\rho_0^e R_0^3 e^{-\sigma t/\varepsilon_d} \tag{6.29}$$

The expression on the left represents the total charge at time $t = 0$, while the expression on the right represents the total charge at time $t \geq 0$. The two integral expressions represent the total bulk charge in the interior of the drop. Solve for the surface charge to get

$$q(t) = q_0 + \frac{1}{3}\rho_0^e R_0(1 - e^{-\sigma t/\varepsilon_d}) \tag{6.30}$$

By symmetry, the voltage is a function only of time and the distance, R, to the center of the drop: $\varphi = \varphi(R, t)$. Thus, the Poisson equation (6.26) becomes:

$$\frac{1}{R^2}\frac{\partial}{\partial R}\left(R^2\frac{\partial\varphi}{\partial R}\right) = \frac{\rho^e}{\varepsilon} = \frac{1}{\varepsilon}\rho_0^e e^{-\sigma t/\varepsilon} \quad . \tag{6.31}$$

Integrate Eq. (6.31) with $\rho^e = \rho_0^e$, $\varepsilon = \varepsilon_d$ inside the drop and $\rho^e = 0$, $\varepsilon = \varepsilon_x$ outside the drop. Get

$$\varphi(R,t) = \begin{cases} \frac{1}{6\varepsilon}\rho_0^e e^{-\sigma t/\varepsilon} R^2 - f_1(t)/R + f_2(t) & \text{for} \quad R < R_0 \\ -g_1(t)/R + g_2(t) & \text{for} \quad R_0 < R < R_1 \end{cases}$$

where $f_1(t), f_2(t), g_1(t), g_2(t)$ are constants (in R) of integration. Assuming the solution is bounded at the origin, we can set $f_1(t) = 0$. Imposing $\varphi = 0$ at R_1, get $g_1(t) = R_1 g_2(t)$. Next, we impose the jump condition on the electric field

$$q(t) = \|\varepsilon \mathbf{E}\| \cdot \mathbf{n} = \varepsilon_x \frac{\partial \varphi}{\partial R}\bigg|_{R_0^+} - \varepsilon_d \frac{\partial \varphi}{\partial R}\bigg|_{R_0^-}$$

to obtain $g_2(t) = q_0 R_0^2/\varepsilon_x R_1 + \rho_0^e R_0^3/3\varepsilon_x R_1$. Lastly, we impose continuity at the interface, to find $f_1(t)$.

$$\left(\frac{1}{6\varepsilon_d}\rho_0^e e^{-\sigma t/\varepsilon} R_0^2 + f_2(t)\right) = \frac{R_0^2}{\varepsilon_x}\left(q_0 + \frac{1}{3}R_0\rho_0^e\right)\left(\frac{1}{R_1} - \frac{1}{R_0}\right)$$

Altogether,

$$\begin{aligned} \varphi(R,t) &= \frac{1}{6\varepsilon_d}\rho_0^e(R^2 - R_0^2)e^{-\sigma t/\varepsilon_d} + \frac{R_0^2}{\varepsilon_x}\left(q_0 + \frac{1}{3}R_0\rho_0^e\right)\left(\frac{1}{R_1} - \frac{1}{R_0}\right) \quad \text{for} \quad R < R_0 \\ \varphi(R,t) &= \frac{R_0^2}{\varepsilon_x}\left(q_0 + \frac{1}{3}R_0\rho_0^e\right)\left(\frac{1}{R_1} - \frac{1}{R}\right) \quad \text{for} \quad R_0 < R < R_1 \end{aligned} \tag{6.32}$$

A major drawback of this test is that our method works on a cylindrical, rather than spherical domain. As such, errors in the voltage will accumulate toward the boundary R_1. However, if we make our cylindrical domain large, these errors should be small. In particular, they will scale as R_0/R_1.

We ran simulations of charge decay on a domain with radius $R_1 = 16$ and height 32. Figure 6.1 shows our computed voltage, visible as a potential pit. Figure 6.2 shows computed verses theoretical values of the bulk charge on the drop over time - the agreement is quite good.

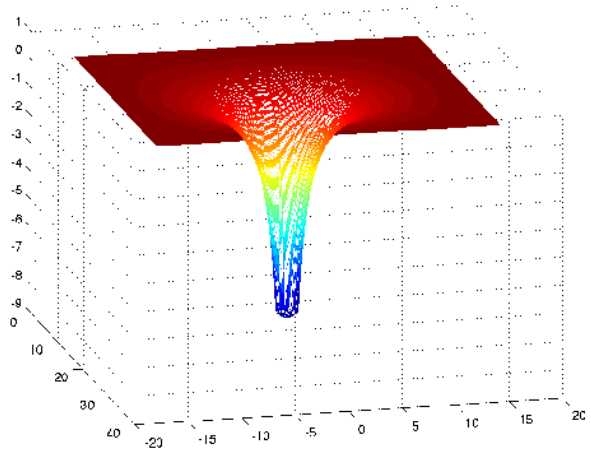

Figure 6.1: The computed voltage on a charged spherical drop, containing a uniform surface charge of $q = 0.62$ and a uniform bulk charge of $\rho^e = 1.23$.

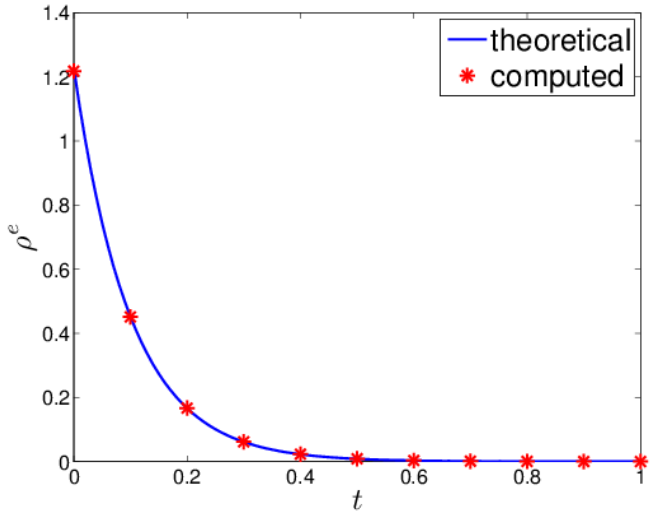

Figure 6.2: Compute vs theoretical charge decay on a drop from an initial value of $\rho^e = 1.23$. The conductance is $\sigma = 10$ and the dielectric coefficient is $\varepsilon_d = 1$. The theoretical value is given by Eq. (6.28).

Thus far, we have developed a method for computing electric charge in multiphase flow, residing both in the fluid bulk, and on the fluid interface. We have proposed a simple test problem to validate our method by comparing our results to an exact solution, and we have begun validating our code by computing the decay of bulk charge, relaxing on a stationary spherical drop. In the future, we intend to further validate our method by computing charge buildup on the surface, for a stationary drop, and measuring the potential and electric field against an exact solution. Finally, we intend to validate our dynamic code by modeling the deformation of a charged drop under the influence of an applied electric field.

Chapter 7

Conclusion

We have developed, implemented, and validated a numerical method to track surfactants on fluid interfaces and in the bulk, and sorption between the two phases. Our method uses finite differences, computes volume of fluid, and tracks the moving front using markers that are advected with the fluid in a Lagrangian fashion. Even without adaptive meshing, our method obtains good accuracy at the interface, and conserves surfactant exactly in the insoluble case. With sorption, surfactant conservation remains very good. We have also adapted our method to track electric charge in the fluid bulk and on the interface, and account for exchanges between the two.

We have applied our method to account for surfactant effects in two existing physical problems: partial coalescence of drops and bubbles, and rising in a stratified medium. Our study of coalescing drops revealed a non-monotonic dependence on surfactant effects, which we explained using a scaling argument comparing surface pressures at the top and base of the drop. We also studied gravity effects and various initial conditions, including gravity deformation, surfactant redistributon due to gravity, and uneven initial surfactant concentrations on the drop and the reservoir. In the case of a clean drop, we found that partial coalescence cannot take place at all when surfactant effects on the reservoir are sufficiently strong. Lastly, we considered the radius of the daughter drop resulting from partial coalescence, and even presented a theoretical coalescence cascade.

Our results for soap films have already been confirmed experimentally, in a study that was possible because of our work [128]. In particular, they observed partial coalescence of soap bubbles, including a cascade of three coalescence events, in a setup matching ours, and measured the radii of the daughter bubbles - the range they found matched ours. They also observed things that our setup didn't allow for - such as the trapping of the bubble in the film, and a partial coalescence event that involves aborted trapping. As a consequence, their work opens new questions, concerning when trapping occurs, and when trapping results in partial coalescence. Another question we did not consider, but which came up in their experiments, was the thickening of the film in the coalescence process, which inhibits coalescence cascades, because thicker films favored trapping [128].

In our study of rising drops, we considered three physical setups, likely to be encountered by oil drops rising in the ocean. Firstly, we studied surfactant-laden drops rising in a uniform ambient. Our results agreed with, and extended, existing results [9]. In our second setup, we considered surfactant laden drops rising in a uniform ambient, and quantified the buoyancy of the entrained fluid. In our third setup, we examined clean drops entering a surfactant layer. Due to Marangoni effects, the drops were sucked into the layer, and then slowed down, after entering, transitioning to

a steady-state settling speed. We were able to describe the resulting variations in drop speed based on the surfactant profile on the surface of the drop.

As with all numerical methods, our method has some fundamental limitations, which cannot be overcome without shifting to a completely different approach. Our approach works well for a middle range of Reynolds numbers, roughly $1 \leq \mathrm{Re} \leq 200$. Below $\mathrm{Re} = 1$, stability considerations force the timestep toward zero, due to the fact that we use explicit timestepping. Above $\mathrm{Re} = 200$, the spatial resolution requirements become prohibitive. Another fundamental limit concerns topological changes, which our method does not handle automatically. By artificially redefining the marker fronts, we can cause drops to merge or pinch off with one another or with other fluid bodies - but potentially incur significant errors when doing so. For problems involving major topological changes to the interface, level set methods may be preferable.

However, some of the limitations currently present in the method are not fundamental, in that they can be overcome by extension of the method. For instance, although our method does not handle complex geometries as a matter of course, like finite element methods, it can be adapted to track moving solid objects using a penalty method [129], which would open a wide range of applications to fluid-structure interactions. Given that other methods for accounting for fluid-structure interactions exist [130], the main advantage of adapting our method to track solid structures would be our capacity to track them simultaneously with fluid interfaces. This would open up applications in which a solid structure interacts with multiphase flow, such as when a solid particle passes through an interface between two immiscible fluids.

In the future, our method could be coupled with adaptive meshing, to obtain excellent accuracy at the front. With adaptive meshing, our method could be applied to problems where additional accuracy at the front is needed. In addition, simple topological changes, such as the merging and pinch off of a drop with a liquid reservoir could be modeled accurately with adaptive meshing. The implementation of a method for adaptive meshing would not be easy, as it would involve communication between multiple grids, and would involve a considerable time commitment on the part of a researcher. Fortunately, the code that we have used to implement our method is highly modular, which will make adaptive meshing considerably easier.

The adaptive meshing could be applied in stages - each stage unlocking new applications. The first stage would start with only two grids, a coarse grid covering a large domain and a fine grid, fixed in space, covering a smaller subset of that domain. This stage could be used to study coalescence more carefully. In particular, for our coalescence paper, we had to begin our simulations after merging had begun and stop them just before pinch-off. A non-adaptive layer of meshes would allow for a more accurate accounting of the pinching and initial merging process. The next stage would be to implement multiple levels of meshing, still fixed in space. Due to our usage of a linear multigrid for inverting the Poisson equation, we would need grid resolution to double each time. Lastly, the grid could be made adaptive, to move with the front, and detect when increased resolution is needed, based on sharp changes in the pressure and flow field.

All of our work has been done on an axially symmetric domain. However, our method can be easily adapted to 2D (planar) problems, by going through the existing code and modifying a number of differential operators, numerical integration schemes, etc. The only real difficulty would be making sure to keep track of every place where the method needs to be modified. A 2D version of our method would be useful for a number of applications, such as gravity currents, or vertical lengthwise cross sections of flowing streams, in which the third dimension can be approximated as uniform.

Our method can also be adapted to fully 3D simulations. Once the method is adapted to planar domains, extending the Eulerian Navier-Stokes solver to a fully 3D domain would be straightforward. However, extending the Lagrangian front tracker would be more difficult. A simple approach would involve an array of markers, between which we interpolate using bicubic splines. However, the topological limitations on the moving front would much more restrictive in 3D. In particular, tracking a single drop in three dimensions would require sewing it together at a seam, and would likely be unfeasible for our front tracking method. However, even with those topological limitations, a 2D marker front would open up new applications. For instance, a 3D version of our method could be used to study 2D turbulence by accounting for the motion of a 2D soap film in 3D space.

Another difficulty associated with a fully 3D version of our method would be the run time of the simulations. Even with the 2D axially symmetric simulations we have applied, we've had to run our code for nearly a month, in some cases, just to complete a single simulation. Thus, for a 3D application, it would most likely be worthwhile to parallelize the method to achieve manageable run times. Parallelization, in turn, would benefit our method in two dimensions as well, making it possible to run multiple successive simulations in a much shorter time. However, making the method parallel would be no easy task, and would require a heavy time investment from future investigators. Fortunately, much of the work involved in adaptive meshing would be applicable to parallelization - in particular, having multiple grids, which must communicate.

One limitation of our study of rising drops and partial coalescence is that we used a linear surfactant relation, which is not applicable in some situations. One possible future application of our method would be to generalize our study using the nonlinear relation, including, perhaps, molecular interactions, as represented in the Frumkin equation. A direct implementation of the Frumkin relation would be straightforward, but would introduce two additional parameters to our system [12]. Because we have already explored the influence of a number of parameters, including the Reynolds number, the Marangoni number, the surface Péclet number, and the Biot number, future investigators could build on our work by focusing on other parameters, such as the adsorption number, the bulk Péclet number, and those parameters introduced by a nonlinear surfactant relation.

Another avenue of research to which our method could be applied is the dynamics of soap films. By tracking the thickness of a soap film, one could predict when it will burst. Since our method already tracks film thickness, applying it to this problem would require no additional modifications to the implementation. However, because the bursting of soap films depends not merely on thickness, but on microscale processes at play on the film, itself, our method would only be able to partially account for the bursting process. As such, any study of film bursting would need to couple our method with other methods - perhaps experiment, or Molecular dynamics simulations, or both. While our method could provide information about film thickness as a function of behavior the macroscopic system, other methods could determine the likelihood of the film bursting, for a given film thickness, and other macroscopic properties of the system.

Our method could also be used to study the trapping of soap bubbles on soap films - a phenomenon that results when one interface merges, and the other does not, so that a bubble is formed on a suspended film [128]. In this case, we would need to track the individual interfaces of the soap film separately. Our setup would involve three interfaces: the interior interface of the bubble, the lower interface of the soap film, and the exterior interface of the bubble and top interface of the suspended film (which we will have begun to merge by the start of the simulation). We are confident that our method can do this, because we have already modeled two adjacent interfaces in our coalescence study - when we modeled deformation effects, caused by a drop settling on a reservoir. Accounting for three interfaces in a small space would require additional modification of the method, but it would be straightforward to implement.

Adapting the method to track electric charge opens a number of avenues for new research. One possible application involves the coalescence of charged droplets, such as occurs in thunder clouds. Charged drops are also known to undergo partial coalescence, under the influence of an applied electric field [121], and our method could be used to investigate the effects of the electric field on the process of partial coalescence. As with our previous study of partial coalescence, it would be necessary to focus on the motion after merging has begun, and before pinch-off has occurred - but this should allow for a complete understanding of the coalescence process.

The deformation of nanoscale droplets by electric fields provides an interesting regime where MD simulations [131] can perhaps overlap with continuum models. It would be fascinating to determine at what point each approach ceases to be valid, and for what regime either approach is applicable.

Alternately, our method may be employed to study electrowetting, including the ability of charged drops to jump from a solid substrate. Our method is already being employed by researchers at MIT so study electric field effects on the contact angle, without actually modeling the electric field. At present, they are artificially adjusting the contact angle, and tracking the subsequent motion of the drop. This research could be extended by tracking the electric field directly, with our augmented method.

Appendix A

Appendices

A.1 Computation of the Viscous Term

Putting the form (3.1) for the deviatoric stress tensor into the radial divergence equations (3.2) and (3.3), we arrive at

$$\nabla \cdot \mathbb{T} \cdot \mathbf{e}_r = \frac{2\mu}{r}\frac{\partial}{\partial r}\left(r\frac{\partial u}{\partial r}\right) + \mu\frac{\partial}{\partial z}\left(\frac{\partial u}{\partial z} + \frac{\partial v}{\partial r}\right) - 2\mu\frac{u}{r^2} \tag{A.1}$$

$$\nabla \cdot \mathbb{T} \cdot \mathbf{e}_z = \frac{\mu}{r}\frac{\partial}{\partial r}\left(r\Big(\frac{\partial u}{\partial z} + \frac{\partial v}{\partial r}\Big)\right) + 2\mu\frac{\partial^2 v}{\partial z^2} \quad . \tag{A.2}$$

We can simplify using the assumption of zero divergence Differentiate the continuity equation to get

$$\frac{\partial}{\partial r}\nabla \cdot \mathbf{u} = \frac{\partial}{\partial r}\left(\frac{1}{r}\frac{\partial}{\partial r}(ru)\right) + \frac{\partial^2 v}{\partial r \partial z} = \frac{1}{r}\frac{\partial u}{\partial r} - \frac{u}{r^2} + \frac{\partial^2 u}{\partial r^2} + \frac{\partial^2 v}{\partial r \partial z} = 0 \tag{A.3}$$

$$\frac{\partial}{\partial z}\nabla \cdot \mathbf{u} = \frac{\partial}{\partial z}\left(\frac{1}{r}\frac{\partial}{\partial r}(ru)\right) + \frac{\partial^2 v}{\partial z^2} = \frac{1}{r}\frac{\partial u}{\partial z} + \frac{\partial^2 u}{\partial r \partial z} + \frac{\partial^2 v}{\partial z^2} = 0 \quad . \tag{A.4}$$

Expanding the derivatives in Equations (A.1) and (A.2), and substituting Equations (A.3) and (A.4), we arrive at

$$\nabla \cdot \mathbb{T} \cdot \mathbf{e}_r = \frac{\mu}{r}\frac{\partial u}{\partial r} + \mu\frac{\partial^2 u}{\partial r^2} + \mu\frac{\partial^2 u}{\partial z^2} - \mu\frac{u}{r^2} \tag{A.5}$$

$$\nabla \cdot \mathbb{T} \cdot \mathbf{e}_z = \frac{\mu}{r}\frac{\partial v}{\partial r} + \mu\frac{\partial^2 v}{\partial r^2} + \mu\frac{\partial^2 v}{\partial z^2} \tag{A.6}$$

which is equivalent to equation (3.4).

A.2 Surfactant Mass Conservation in the Cap Angle Problem

We derive relation (5.16) using the solution of Sadhal and Johnson [9] to the spherical cap problem in creeping flow. Having obtained the flow field around and inside the rising drop, Sadhal and Johnson

computed the speed of the rising drop as:

$$U_{\mathrm{SJ}} = \frac{U_{\mathrm{HR}}}{C_D(\theta_c)} \tag{A.7}$$

where U_{HR} is the familiar Hadamard-Rybczynski speed of a clean drop, given in Eq. (1.2), and $C_D(\theta)$ is a drag coefficient, given in Eq. (5.17). They also obtained a closed form expression for the tangential stress at the interface:

$$\frac{\partial \widetilde{\gamma}}{\partial \theta} = \mu_a U_{\mathrm{SJ}} h(\theta, \theta_c) \tag{A.8}$$

where $\widetilde{\gamma}$ is the dimensional surface tension on the stagnant cap, μ_a is the viscosity of the ambient fluid, and

$$\begin{aligned} h(\theta,\theta_c) = \frac{2}{\pi}\tan\Big(\frac{\theta}{2}\Big)\Bigg(\frac{3}{2}(1+\cos\theta)\Bigg(\arcsin\Big(\frac{\cos\theta-\cos\theta_c}{1+\cos\theta}\Big)^{1/2} \\ + \frac{(\cos\theta-\cos\theta_c)^{1/2}(1+\cos\theta_c)^{1/2}}{1+\cos\theta}\Bigg) + \frac{(1+\cos\theta_c)^{3/2}}{(\cos\theta-\cos\theta_c)^{1/2}}\Bigg) \quad . \end{aligned} \tag{A.9}$$

Using the linear surfactant relation (2.14), we find that the surfactant concentration on the stagnant cap satisfies

$$\frac{\partial}{\partial\theta}\left(\frac{\Gamma}{\Gamma_0}\right) = -\frac{1}{\mathrm{Mg}}\frac{h(\theta,\theta_c)}{C_D(\theta_c)} \tag{A.10}$$

Assuming $\theta_c < \pi$, we can use the condition $\Gamma(\theta=\theta_c)=0$. Then the above expression integrates to

$$\frac{\Gamma(\theta)}{\Gamma_0} = -\frac{1}{\mathrm{Mg}}\frac{H(\theta,\theta_c)}{C_D(\theta_c)} \quad \text{where} \quad H(\theta,\theta_c) = \int_{\theta_c}^{\theta} H(\psi,\theta_c)d\psi \tag{A.11}$$

The function h can be integrated analytically over the interface by making the substitutions

$$\eta_c = 1+\cos\theta_c \quad \text{and} \quad \eta = 1+\cos\psi \quad \text{so} \quad d\eta = -\sin\psi d\psi$$

and applying the trig identity

$$\tan\Big(\frac{\psi}{2}\Big) = \frac{\sin\psi}{1+\cos\psi}$$

to get

$$\tan\Big(\frac{\psi}{2}\Big)d\psi = -\frac{d\eta}{\eta} \quad .$$

Obtain

$$\begin{aligned} H(\theta,\theta_c) &= -\frac{2}{\pi}\int_{1+\cos\theta_c}^{1+\cos\theta}\left(\frac{3}{2}\arcsin\left(\frac{\eta-\eta_c}{\eta}\right)^{1/2} + \frac{3}{2}\frac{\sqrt{\eta_c(\eta-\eta_c)}}{\eta} + \frac{\eta_c^{3/2}}{\eta\sqrt{\eta-\eta_c}}\right)d\eta \\ &= -\frac{2}{\pi}\left(\Big(\frac{3}{2}\eta-\eta_c\Big)\arcsin\left(\frac{\eta-\eta_c}{\eta}\right)^{1/2} + \frac{3}{2}\sqrt{\eta_c(\eta-\eta_c)}\right)\Bigg|_{1+\cos\theta_c}^{1+\cos\theta} \quad . \end{aligned}$$

When $\theta=\theta_c$, the rightmost expression is zero, so we obtain the closed form expression for H:

$$H(\theta,\theta_c) = \int_{\theta_c}^{\theta} h(\psi,\theta_c)d\psi = -\frac{2}{\pi}\left(\Big(\frac{3}{2}\eta-\eta_c\Big)\arcsin\left(\frac{\eta-\eta_c}{\eta}\right)^{1/2} + \frac{3}{2}\sqrt{\eta_c(\eta-\eta_c)}\right) \quad . \tag{A.12}$$

This gives us a closed form expression for the surfactant concentration profile on the cap angle. The total surfactant mass, $M_\Gamma(\theta_c)$, on the drop can be obtained from an area integral over the stagnant cap.

$$M_\Gamma(\theta_c) = -\frac{2\pi R_0^2\Gamma_0}{\mathrm{Mg}C_D(\theta_c)}\int_0^{\theta_c} H(\theta,\theta_c)\sin\theta d\theta = 4\pi R_0^2\Gamma_0 \quad . \tag{A.13}$$

The rightmost expression is the surfactant mass when the surface concentration is uniformly distributed. The expression (A.12) we found for H can be analytically integrated:

$$\begin{aligned}
\int_0^{\theta_c} H(\theta,\theta_c)\sin\theta d\theta &= \frac{2}{\pi}\int_2^{\eta_c}\left(\left(\frac{3}{2}\eta-\eta_c\right)\arcsin\left(\frac{\eta-\eta_c}{\eta}\right)^{1/2}+\frac{3}{2}\sqrt{\eta_c(\eta-\eta_c)}\right)d\eta \\
&= \frac{2}{\pi}\left(\frac{3}{2}\left(\frac{1}{2}\eta^2\arcsin\left(\frac{\eta-\eta_c}{\eta}\right)^{1/2}-\frac{1}{6}(\eta+2\eta_c)\sqrt{\eta_c(\eta-\eta_c)}\right)\right. \\
&\quad \left.-\eta_c\left(\eta\arcsin\left(\frac{\eta-\eta_c}{\eta}\right)^{1/2}-\sqrt{\eta_c(\eta-\eta_c)}\right)+\frac{3}{2}\left(\frac{2}{3}\eta_c^{1/2}(\eta-\eta_c)^{3/2}\right)\right)\Bigg|_2^{\eta_c} \\
&= -\frac{2}{\pi}\left(\frac{3}{2}\left(\theta_c-\frac{1}{6}(4+2\cos\theta_c)\sin\theta_c\right)-(1+\cos\theta_c)(\theta_c-\sin\theta_c)+(1-\cos\theta_c)\sin\theta_c\right) \\
&= -\frac{2}{\pi}\left(2\theta_c+4\sin\theta_c-\sin 2\theta_c-4\theta_c\cos\theta_c\right)
\end{aligned}$$

Substituting this into Eq. (A.13) and simplifying, obtain Eq. (5.16):

$$\mathrm{Mg} = \frac{2\theta_c-4\theta_c\cos\theta_c-\sin 2\theta_c+4\sin\theta_c}{4\pi C_D(\theta_c)} \quad . \tag{A.14}$$

Bibliography

[1] T.L. Heath. *The Works of Archimedes*. Cambridge University Press, 1897.

[2] G.G. Stokes. *Mathematical and Physical Papers, Vol. III*. Cambridge University Press, 1901.

[3] J.S. Hadamard. Mouvement permanent lent d'une sphere liquide et visqueuse dans un liquide visqueux. *C.R. Acad. Sci.*, 152:1735, 1911.

[4] Rybczynski. Uber die fortschreitende bewegung einer flussigen kugel in einem zahen medium. *Bull. Acad. Sci. Cracovie*, A:40–46, 1911.

[5] Kevin McKeigue Shi-Yow Lin and Charles Maldarelli. Diffusion-limited interpretation of the induction period in the relaxation in surface tension due to the adsorption of straight chain, small polar group surfactants: theory and experiment. *Langmuir*, 7:10551066, 1991.

[6] *Langmuir*, 30:1281212818, 2014.

[7] John A. Holbrook and M. Douglas Levan. Retardation of droplet motion by surfactant. part 1. theoretical development and asymptotic solutions. *Chemical Engineering Communications*, 20(3-4):191–207, 1983.

[8] John A. Holbrook and M. Douglas Levan. Retardation of droplet motion by surfactant. part 2. numerical solutions for exterior diffusion, surface diffusion, and adsorption kinetics. *Chemical Engineering Communications*, 20(5-6):273–290, 1983.

[9] S. S. Sadhal and Robert E. Johnson. Stokes flow past bubbles and drops partially coated with thin films. part 1. stagnant cap of surfactant film exact solution. *Journal of Fluid Mechanics*, 126:237–250, 1 1983.

[10] H.A. Stone and L.G. Leal. The effects of surfactants on drop deformation and breakup. *J. Fluid Mech.*, 220:161–186, 1990.

[11] C.D. Eggleton and K.J. Stebe. An adsorption-desorption-controled surfactant on a deforming droplet. *J. Colloid and Interface Sci.*, 208:68–80, 1998.

[12] Jinnan Chen and Kathleen J. Stebe. Marangoni retardation of the terminal velocity of a settling droplet: The role of surfactant physico-chemistry. *Journal of Colloid and Interface Science*, 178(1):144 – 155, 1996.

[13] B. Lafaurie, C. Nardone, R. Scardovelli, S. Zaleski, and G. Zanetti. Modelling merging and fragmentation in multiphase flows with surfer. *J. Comp. Phys.*, 113(1):134–147, 1994.

[14] M. Sussman, P. Smereka, and S. Osher. A level set approach for computing solutions to incompressible 2-phase flow. *J. Comp. Phys.*, 114:146159, 1994.

[15] S. Popinet and S. Zaleski. A front tracking algorithm for the accurate representation of surface tension. *Int. J. Numer. Meth. Fluids*, 30:775–793, 1999.

[16] J.A. Sethian. *Fast marching methods and level sets methods for propagating interfaces.* Cambridge Univ. Press, Cambridge, U.K., 1999.

[17] M. Sussman, A.S. Almgren, J.B. Bell, P. Colella, L.H. Howell, and M.L. Welcome. An adaptive level set approach for incompressible two-phase flows. *J. Comp. Phys.*, 148:81124, 1999.

[18] G. Tryggvason, B. Bunner, A. Esmaeeli, D. Juric, N. Al-Rawahi, W. Tauber, S. Nas J. Han, and Y.J. Jan. A front-tracking method for the computations of multiphase flow. *J. Comput. Phys.*, 169(2):708 – 759, 2001.

[19] P.K. Notz and O.A. Basaran. Dynamics of drop formation in an electric field. *J. Colloid Interface Sci.*, 213:218237, 1999.

[20] C.W. Hirt and B.D. Nichols. Volume of fluid (vof) method for the dynamics of free boundaries. *J. Comput. Phys.*, 39(1):201 – 225, 1981.

[21] M. Muradoglu and G. Tryggvason. A front-tracking method for computation of interfacial flows with soluble surfactants. *J. Comput. Phys.*, 227(4):2238 – 2262, 2008.

[22] Nivedita R. Gupta Fang Jin and Kathleen J. Stebe. The detachment of a viscous drop in a viscous solution in the presence of a soluble surfactant. *Phys. Fluids*, 18(022103), 2006.

[23] M.C. Lai, Y.H. Tseng, and H. Huang. An immersed boundary method for interfacial flows with insoluble surfactant. *J. Comput. Phys.*, 227(15):7279 – 7293, 2008.

[24] Y. Kim and M.C. Lai. Simulating the dynamics of inextensible vesicles by the penalty immersed boundary method. *J. Comput. Phys.*, 229(12):4840 – 4853, 2010.

[25] M.R. Booty and M. Siegel. A hybrid numerical method for interfacial fluid flow with soluble surfactant. *J. Comput. Phys.*, 229(10):3864 – 3883, 2010.

[26] S. Khatri and A.K. Tornberg. A numerical method for two phase flows with insoluble surfactants. *Comput. Fluids*, 49(1):150 – 165, 2011.

[27] Shilpa Khatri and Anna-Karin Tornberg. An embedded boundary method for soluble surfactants with interface tracking for two-phase flows. *Journal of Computational Physics*, 256(0):768 – 790, 2014.

[28] S. Ganesan and L. Tobiska. Arbitrary lagrangianeulerian finite-element method for computation of two-phase flows with soluble surfactants. *J. Comput. Phys.*, 231(9):3685 – 3702, 2012.

[29] J.J. Xu, Y. Yang, and J. Lowengrub. A level-set continuum method for two-phase flows with insoluble surfactant. *J. Comput. Phys.*, 231(17):5897 – 5909, 2012.

[30] K.E. Teigen, P. Song, J. Lowengrub, and A. Voigt. A diffuse-interface method for two-phase flows with soluble surfactants. *J. Comput. Phys.*, 230(2):375 – 393, 2011.

[31] S. Adami, X.Y. Hu, and N.A. Adams. A conservative {SPH} method for surfactant dynamics. *J. Comput. Phys.*, 229(5):1909 – 1926, 2010.

[32] H. Fujioka. A continuum model of interfacial surfactant transport for particle methods. *J. Comput. Phys.*, 234(0):280 – 294, 2013.

[33] H. Liu and Y. Zhang. Phase-field modeling droplet dynamics with soluble surfactants. *J. Comput. Phys.*, 229(24):9166 – 9187, 2010.

[34] D.L. Brown, R. Cortez, and M.L. Minion. Accurate projection methods for the incompressible Navier-Stokes equations. *J. Comp. Phys.*, 168:464–499, 2001.

[35] F. Blanchette, L. Messio, and J.W.M. Bush. The influence of surface tension gradients on drop coalescence. *Phys. Fluids*, 21, 2009.

[36] I. Navarro and F. Blanchette. Governing equations for simulations of soap bubbles. Master's thesis, University of California at Merced, 2010.

[37] H.A. Stone. A simple derivation of the time dependent convective diffusion equation for surfactant transport along a deforming interface. *Phys. Fluids A*, 2, 1990.

[38] C.H. Chang and E.I. Franses. Modified langmuirhinselwood kinetics for dynamic adsorption of surfactants at the air/water interface. *Colloids and Surfaces*, 69(23):189 – 201, 1992.

[39] F. Blanchette and Y. Lei. Energy considerations for multiphase fluids with variable density and surface tension. *SIAM Rev.*, 51(2):423–431, 2009.

[40] J.C. Padrino, T. Funada, and D.D. Joseph. Purely irrotational theories for the viscous effects on the oscillations of drops and bubbles. *Int. J. Multiphas. Flow*, 34:61–75, 2008.

[41] A. Bhakta and E. Ruckenstein. Decay of standing foams: drainage, coalescence and collapse. *Adv. Colloid Interface Sci.*, 70:1–124, 1997.

[42] E.X. Berry and R.L. Reinhardt. Analysis of cloud drop growth by collection. 3. Accretion and self-collection. *J. Atmos. Sci.*, 31:2118–2126, 1974.

[43] H.T. Ochs III, K.V. Beard, R.R. Czys, N.F. Laird, D.E. Schaufelberger, and D.J. Holdridge. Collisions between small precipitation drops. part i: Laboratory measurements of bounce, coalescence, and temporary coalescence. *J. Atmos. Sci.*, 52(12):2258–2275, June 1994.

[44] F. Raes, R. Van Dingenen, E. Vignati, J. Wilson, J.P. Putaud, J.H. Seinfeld, and P. Adams. Formation and cycling of aerosols in the global troposphere. *Atmos. Env.*, 34(25):4215 – 4240, 2000.

[45] T. Sarpkaya. Vorticity, free surface, and surfactants. *Annu. Rev. Fluid Mech.*, 28:83–128, January 1996.

[46] J.J. Thompson and H.F. Newall. On the formation of vortex rings by drops falling into liquids and some allied phenomena. *Proc. R. Soc. Lond.*, 39:417–436, 1885.

[47] H.A. Stone, A.D. Stroock, and A. Ajdari. Engineering flows in small devices: Microfluidics toward a lab-on-a-chip. *Annu. Rev. Fluid Mech.*, 36:381–411, 2004.

[48] Y.K. Cai. Phenomena of a liquid drop falling to a liquid surface. *Exp. Fluids*, 7(6):388–394, 1989.

[49] G.P. Neitzel and P. Dell'Aversana. Noncoalescence and nonwetting behavior of liquids. *Annu. Rev. Fluid Mech.*, 34:267–289, 2002.

[50] M. Rein. The transitional regime between coalescing and splashing drops. *J. Fluid Mech.*, 306:145–165, 0 1996.

[51] O. Reynolds. On the floating of drops on the surface of water depending only on the purity of the surface. *Proc. Lit. Phil. Soc. Manchester*, 21:12, 1881.

[52] E.G. Cockbain and T.S. McRoberts. The stability of elementary emulsion drops and emulsions. *J. Colloid Sci.*, 8(4):440 – 451, 1953.

[53] M. Linton and K.L. Sutherland. The coalescence of liquid drops. *J. Colloid Sci.*, 11(4-5):391 – 397, 1956.

[54] G.E. Charles and S.G. Mason. The mechanism of partial coalescence of liquid drops at liquid/liquid interfaces. *J. Colloid Sci.*, 15:105–122, 1960.

[55] S.T. Thoroddsen and K. Takehara. The coalescence cascade of a drop. *Phys. Fluids*, 12:1265–1267, 2000.

[56] H. Aryafar and H.P. Kavehpour. Drop coalescence through planar surfaces. *Phys. Fluids*, 18:072105, 2006.

[57] E.M. Honey and H.P. Kavehpour. Astonishing life of a coalescing drop on a free surface. *Phys. Rev. E*, 73:027301, 2006.

[58] Y. Amarouchene, G. Cristobal, and H. Kellay. Noncoalescing drops. *Phys. Rev. Lett.*, 87:206104, Oct 2001.

[59] F. Blanchette and T.P. Bigioni. Partial coalescence of drops at liquid interfaces. *Nature Phys.*, 2(4):254–257, 2006.

[60] F. Blanchette and T.P. Bigioni. Dynamics of drop coalescence at fluid interfaces. *J. Fluid Mech.*, 620:333–352, 2009.

[61] T. Gilet, K. Mulleners, and J.P. Lecomte. Critical parameters for the partial coalescence of a droplet. *Phys. Rev. E*, 75(3):036303, 2007.

[62] S.T. Thoroddsen, B. Qian, T.G. Etoh, and K. Takehara. The initial coalescence of miscible drops. *Phys. Fluids*, 19:072110, 2007.

[63] B.J. Fischer and S.M. Troian. Thinning and disturbance growth in liquid films mobilized by continuous surfactant delivery. *Phys. Fluids*, 15(3837), 2003.

[64] E.A. Van Nierop, B. Scheid, and H.A. Stone. On the thickness of soap films: an alternative to frankel's law corrigendum. *J. Fluid Mech.*, 630:443–443, 6 2009.

[65] A. Frumkin and V. Levich. On surfactants and interfacial motion. *Zhur. Fiz. Khim.*, 21(1183), 1947.

[66] V.G. Levich. *Physicochemical Hydrodynamics*. Prentice Hall, New York, 1962.

[67] Brenner H. Edwards, D. A. and D. T. Wasan. *Interfacial Transport Processes and Rheology*. Butterworth-Heinemann, 1991.

[68] F.H. Garner and A.H.P. Skelland. Some factors affecting droplet behaviour in liquid-liquid systems. *Chemical Engineering Science*, 4(4):149 – 158, 1955.

[69] Banchero J. T. Elzinga, E. R. Some observations on the mechanics of drops in liquid-liquid systems. *American Institute of Chemical Engineers Journal*, 7(4):394 – 399, 1961.

[70] T. R. Fritsch T. J. Horton and R. C. Kintner. Experimental determination of circulation velocities inside drops. *The Canadian Journal of Chemical Engineering*, 43(3):143146, June 1965.

[71] R.M. Edge and C.D. Grant. The motion of drops in water contaminated with a surface-active agent. *Chemical Engineering Science*, 27(9):1709 – 1721, 1972.

[72] T. Yamamoto and T. Ishii. Effect of surface active materials on the drag coefficients and shapes of single large gas bubbles. *Chemical Engineering Science*, 42(6):1297 – 1303, 1987.

[73] Kathleen J. Stebe, ShiYow Lin, and Charles Maldarelli. Remobilizing surfactant retarded fluid particle interfaces. i. stressfree conditions at the interfaces of micellar solutions of surfactants with fast sorption kinetics. *Physics of Fluids A: Fluid Dynamics (1989-1993)*, 3(1):3–20, 1991.

[74] Yongqin Zhang and J. A. Finch. A note on single bubble motion in surfactant solutions. *Journal of Fluid Mechanics*, 429:63–66, 2 2001.

[75] P Savic. *Circulation and distortion of liquid drops falling through a viscous medium*. National Research Council Canada, 1953.

[76] R.E. Davis and Andreas Acrivos. The influence of surfactants on the creeping motion of bubbles. *Chemical Engineering Science*, 21(8):681 – 685, 1966.

[77] J. F. Harper. On bubbles with small immobile adsorbed films rising in liquids at low reynolds numbers. *Journal of Fluid Mechanics*, 58:539–545, 5 1973.

[78] Z He, C Maldarelli, and Z Dagan. The size of stagnant caps of bulk soluble surfactant on the interfaces of translating fluid droplets. *Journal of Colloid and Interface Science*, 146(2):442 – 451, 1991.

[79] BV Deryagin, SS Dukhin, and VA Lisichenko. The kinetics of the attachment of mineral particles to bubbles during flotation. i. the electric field of a moving bubble. *Russ. J. Phys. Chem*, 33:389–393, 1959.

[80] D.A. Saville. The effects of interfacial tension gradients on the motion of drops and bubbles. *The Chemical Engineering Journal*, 5(3):251 – 259, 1973.

[81] J. F. Harper. On spherical bubbles rising steadily in dilute surfactant solutions. *The Quarterly Journal of Mechanics and Applied Mathematics*, 27(1):87–100, 1974.

[82] Yanping Wang, Demetrios T. Papageorgiou, and Charles Maldarelli. Increased mobility of a surfactant-retarded bubble at high bulk concentrations. *Journal of Fluid Mechanics*, 390:251–270, 7 1999.

[83] Graham F. Andrews, Richard Fike, and Shulun Wong. Bubble hydrodynamics and mass transfer at high reynolds number and surfactant concentration. *Chemical Engineering Science*, 43(7):1467 – 1477, 1988.

[84] John B. Mclaughlin. Numerical simulation of bubble motion in water. *Journal of Colloid and Interface Science*, 184(2):614 – 625, 1996.

[85] Renksizbulut M. Leppinen, D. M. and R. J. Haywood. The effects of surfactants on droplet behavior at intermediate reynolds-numbers .1. the numerical-model and steady-state results. *Chem. Eng. Sci.*, 51(3), 1996.

[86] R. Bel Fdhila and P. C. Duineveld. The effect of surfactant on the rise of a spherical bubble at high reynolds and peclet numbers. *Physics of Fluids (1994-present)*, 8(2):310–321, 1996.

[87] Ravichandra Palaparthi, Demetrios T. Papageorgiou, and Charles Maldarelli. Theory and experiments on the stagnant cap regime in the motion of spherical surfactant-laden bubbles. *Journal of Fluid Mechanics*, 559:1–44, 7 2006.

[88] B. Cuenot, J. Magnaudet, and B. Spennato. The effects of slightly soluble surfactants on the flow around a spherical bubble. *Journal of Fluid Mechanics*, 339:25–53, 5 1997.

[89] Savas Tasoglu, Utkan Demirci, and Metin Muradoglu. The effect of soluble surfactant on the transient motion of a buoyancy-driven bubble. *Physics of Fluids (1994-present)*, 20(4):–, 2008.

[90] S. Hartland. The profile of the draining film between a rigid sphere and a deformable fluid-liquid interface. *Chemical Engineering Science*, 24(6):987 – 995, 1969.

[91] S.T. Shah, D.T. Wasan, and R.C. Kintner. Passage of a liquid drop through a liquidliquid interface. *Chemical Engineering Science*, 27(5):881 – 893, 1972.

[92] A. F. Jones and S. D. R. Wilson. The film drainage problem in droplet coalescence. *Journal of Fluid Mechanics*, 87:263–288, 7 1978.

[93] P.G. Smith and T.G.M. Van De Ven. The effect of gravity on the drainage of a thin liquid film between a solid sphere and a liquid/fluid interface. *Journal of Colloid and Interface Science*, 100(2):456 – 464, 1984.

[94] H.C. Maru, D.T. Wasan, and R.C. Kintner. Behavior of a rigid sphere at a liquidliquid interface. *Chemical Engineering Science*, 26(10):1615 – 1628, 1971.

[95] A. S. Geller, S. H. Lee, and L. G. Leal. The creeping motion of a spherical particle normal to a deformable interface. *Journal of Fluid Mechanics*, 169:27–69, 8 1986.

[96] A.N. Srdic-Mitrovic, N.A. Mohamed, and H.J.S. Fernando. Gravitational settling of particles through density interfaces. *Journal of Fluid Mechanics*, 381:175–198, 2 1999.

[97] Nicole Abaid, David Adalsteinsson, Akua Agyapong, and Richard M. McLaughlin. An internal splash: Levitation of falling spheres in stratified fluids. *Physics of Fluids (1994-present)*, 16(5):1567–1580, 2004.

[98] Roberto Camassa, Claudia Falcon, Joyce Lin, Richard M. McLaughlin, and Richard Parker. Prolonged residence times for particles settling through stratified miscible fluids in the stokes regime. *Physics of Fluids (1994-present)*, 21(3):–, 2009.

[99] Roberto Camassa, Claudia Falcon, Joyce Lin, Richard M. McLaughlin, and Nicholas Mykins. A first-principle predictive theory for a sphere falling through sharply stratified fluid at low reynolds number. *Journal of Fluid Mechanics*, 664:436–465, 12 2010.

[100] King Yeung Yick, Carlos R. Torres, Thomas Peacock, and Roman Stocker. Enhanced drag of a sphere settling in a stratified fluid at small reynolds numbers. *Journal of Fluid Mechanics*, 632:49–68, 8 2009.

[101] M. Bayareh, A. Doostmohammadi, S. Dabiri, and A. M. Ardekani. On the rising motion of a drop in stratified fluids. *Physics of Fluids*, 25(10):–, 2013.

[102] A. Doostmohammadi, S. Dabiri, and A. M. Ardekani. A numerical study of the dynamics of a particle settling at moderate reynolds numbers in a linearly stratified fluid. *Journal of Fluid Mechanics*, 750:5–32, 7 2014.

[103] H. Hanakazi, K. Kashimoto, and T. Okamura. Jets generated by a sphere moving vertically in a stratified fluid. *Journal of Fluid Mechanics*, 638:173–197, 11 2009.

[104] H. Hanazaki, K. Konishi, and T. Okamura. Schmidt-number effects on the flow past a sphere moving vertically in a stratified diffusive fluid. *Physics of Fluids (1994-present)*, 21(2):–, 2009.

[105] H. Hanazaki, S. Nakamura, and H. Yoshikawa. Numerical simulation of jets generated by a sphere moving vertically in a stratified fluid. *Journal of Fluid Mechanics*, 765:424–451, 2 2015.

[106] Lawrence H. Larsen. Oscillations of a neutrally buoyant sphere in a stratified fluid. *Deep Sea Research and Oceanographic Abstracts*, 16(6):587 – 603, 1969.

[107] Istvn Bir, K. Gbor Szab, Balzs Gyre, Imre M. Jnosi, and Tams Tl. Power-law decaying oscillations of neutrally buoyant spheres in continuously stratified fluid. *Physics of Fluids (1994-present)*, 20(5):–, 2008.

[108] A. Doostmohammadi and A. Ardekani. Interaction between a pair of particles settling in a stratified fluid. *Phys. Rev. E*, 88:023029, Aug 2013.

[109] S. Dabiri, A. Doostmohammadi, M. Bayareh, and A.M. Ardekani. Rising motion of a swarm of drops in a linearly stratified fluid. *International Journal of Multiphase Flow*, 69(0):8 – 17, 2015.

[110] A. Doostmohammadi and A. M. Ardekani. Suspension of solid particles in a density stratified fluid. *Physics of Fluids*, 27(2):–, 2015.

[111] Kolja Kindler, Arzhang Khalili, and Roman Stocker. Diffusion-limited retention of porous particles at density interfaces. *Proceedings of the National Academy of Sciences*, 107(51):22163–22168, 2010.

[112] R. Camassa, S. Khatri, R. M. McLaughlin, J. C. Prairie, B. L. White, and S. Yu. Retention and entrainment effects: Experiments and theory for porous spheres settling in sharply stratified fluids. *Physics of Fluids (1994-present)*, 25(8):–, 2013.

[113] F. Blanchette and A. M. Shapiro. Drops settling in sharp stratification with and without marangoni effects. *Physics of Fluids.*, 23(4), 2012.

[114] John S. Eow and Mojtaba Ghadiri. Electrostatic enhancement of coalescence of water droplets in oil: a review of the technology. *Chemical Engineering Journal*, 85(23):357 – 368, 2002.

[115] Max Chabert, Kevin D. Dorfman, and Jean-Louis Viovy. Droplet fusion by alternating current (ac) field electrocoalescence in microchannels. *ELECTROPHORESIS*, 26(19):3706–3715, 2005.

[116] G. F. Christopher, J. Bergstein, N. B. End, M. Poon, C. Nguyen, and S. L. Anna. Coalescence and splitting of confined droplets at microfluidic junctions. *Lab Chip*, 9:1102–1109, 2009.

[117] Yong-Mi Jung () and In Seok Kang (). A novel actuation method of transporting droplets by using electrical charging of droplet in a dielectric fluid. *Biomicrofluidics*, 3(2):–, 2009.

[118] Levine ZA Ho M-C Colvin ME Vernier PT Tokman M, Lee JH. Electric field-driven water dipoles: Nanoscale architecture of electroporation. *PLoS ONE*, 8(4), April 2013.

[119] Geoffrey Taylor. Disintegration of water drops in an electric field. *Proceedings of the Royal Society of London A: Mathematical, Physical and Engineering Sciences*, 280(1382):383–397, 1964.

[120] S. Torza and S. G. Mason. Coalescence of two immiscible liquid drops. *Science*, 163(3869):813–814, 1969.

[121] B. S. Hamlin, J. C. Creasey, and W. D. Ristenpart. Electrically tunable partial coalescence of oppositely charged drops. *Phys. Rev. Lett.*, 109:094501, Aug 2012.

[122] Hamarz Aryafar and H. Pirouz Kavehpour. Electrocoalescence: Effects of dc electric fields on coalescence of drops at planar interfaces. *Langmuir*, 25(21):12460–12465, 2009. PMID: 19817472.

[123] M. Mousavichoubeh, M. Ghadiri, and M. Shariaty-Niassar. Electro-coalescence of an aqueous droplet at an oilwater interface. *Chemical Engineering and Processing: Process Intensification*, 50(3):338 – 344, 2011.

[124] Mirhamed Mousavichoubeh, Mojtaba Shariaty-Niassar, and Mojtaba Ghadiri. The effect of interfacial tension on secondary drop formation in electro-coalescence of water droplets in oil. *Chemical Engineering Science*, 66(21):5330 – 5337, 2011.

[125] A. Belmonte-F. Dollar W. D. Ristenpart, J. C. Bird and H. A. Stone. Non-coalescence of oppositely charged drops. *Nature*, 461(7262):377–380, September 2009.

[126] D. A. Saville. Electrohydrodynamics:the taylor-melcher leaky dielectric model. *Annual Review of Fluid Mechanics*, 29(1):27–64, 1997.

[127] Ory Schnitzer and Ehud Yariv. The taylormelcher leaky dielectric model as a macroscale electrokinetic description. *Journal of Fluid Mechanics*, 773:1–33, 6 2015.

[128] G. Pucci, D. M. Harris, and J. W. M. Bush. Partial coalescence of soap bubbles. *Physics of Fluids*, 27(6):–, 2015.

[129] Dmitry Kolomenskiy and Kai Schneider. A fourier spectral method for the navierstokes equations with volume penalization for moving solid obstacles. *Journal of Computational Physics*, 228(16):5687 – 5709, 2009.

[130] C.S. Peskin. The immersed boundary method. *Acta Numer.*, 11:479–517, 0 2002.

[131] P. Thomas Vernier Mayya Tokman Michael E. Colvin Jane HyoJin Lee, Zachary A. Levine. Electric field effects on water and water-vacuum interfaces in molecular dynamics simulations. *Biophysical Journal*, 98(3), April 2015.